MAPPING THE FUNCTIONAL CONNECTIVITY OF THE MOUSE ANTEROVENTRAL COCHLEAR NUCLEUS

Luke Campagnola

A dissertation submitted to the faculty of the University of North Carolina at Chapel Hill in partial fulfillment of the requirements for the degree of Doctor of Philosophy in the Curriculum of Neurobiology.

Chapel Hill
2013

Approved by:

Ken McCarthy

Paul Manis

Richard Weinberg

Nell Cant

Mark Zylka

ABSTRACT

LUKE CAMPAGNOLA: Mapping the Functional Connectivity of the Mouse Anteroventral Cochlear Nucleus
(Under the direction of Paul Manis)

The cochlear nucleus is the first central processor of auditory information and provides afferent input to most of the major brainstem and midbrain auditory nuclei. Presently, the lack of detailed data describing connectivity within the circuitry of the cochlear nucleus poses a major barrier to understanding its role in auditory processing, and thus complicates attempts to understand the auditory system as a whole. We have applied a novel, quantitative approach to mapping local circuits in the anteroventral cochlear nucleus (AVCN) using laser-scanning photostimulation. This approach included the development of new software and techniques that will allow more efficient acquisition and analysis of functional connectivity. Evoked responses to glutamate uncaging were analyzed to measure the amplitude and kinetics of individual synaptic events, providing a detailed description of connectivity and synaptic properties. We found that the majority of cells, including all three AVCN principal cell types, receive input from both D-stellate and tuberculoventral cells. Additionally, a small fraction of cells receive inhibitory input from an unidentified cell population at the dorsal-medial boundary of the AVCN, or excitatory input from within the AVCN. In agreement with previous reports, AVCN cells integrate from tuberculoventral cells occupying a narrow corresponding isofrequency region of the dorsal cochlear nucleus. In contrast, D-stellate inputs to the same cells arise from a much larger area which spans a wider frequency range. Furthermore, T-stellate cells integrate these inputs from an area that spans twice the frequency range of that integrated by bushy cells. Our results suggest that inhibitory circuits, even from a single presynaptic class, have patterns of convergence for each cell type that can support different kinds of spectral and temporal processing.

ACKNOWLEDGEMENTS

I would like to express my deepest gratitude to my advisor, Dr. Paul Manis, without whose creativity, patience, and encyclopedic knowledge I could not have realized this project. I can only hope to follow your example as a creative scientist, shrewd skipper, and dedicated parent.

I thank my committee members Drs. Richard Weinberg, Ken McCarthy, Nell Cant, and Mark Zylka for their insightful and welcoming support, and especially to Richard for his numerous attempts to impart both encouragement and practical sense upon my naïve ambitions.

I am grateful for the many hours of discussion and bug squashing with Megan Kratz, who made significant contributions to this work.

Finally, I thank my amazing wife, Rose, for her endless love, dedication, and support; and our children Jonah and Eleanor for inspiration and much needed distraction.

TABLE OF CONTENTS

LIST OF TABLES

LIST OF FIGURES

LIST OF ABBREVIATIONS

ACSF	artificial cerebrospinal fluid
AMPA	2-amino-3-(3-hydroxy-5-methyl-isoxazol-4-yl)propanoic acid
AVCN	anteroventral cochlear nucleus
CCD	charge-coupled device
CMR	comodulation masking release
DAQ	data acquisition (hardware)
DCN	dorsal cochlear nucleus
EPSC	excitatory postsynaptic current
GABA	γ-aminobutyric acid
IC	inferior colliculus
IPSC	inhibitory postsynaptic current
LED	light emitting diode
MNI	4-Methoxy-7-nitroindolinyl
MRI	magnetic resonance imaging
NMDA	N-methyl-D-aspartic acid
PSC	postsynaptic current
PSTH	post-stimulus time histogram
PVCN	posteroventral cochlear nucleus
ROE	rotary encoder
SOC	superior olivary complex
TTL	transistor-transistor logic
VCN	ventral cochlear nucleus

Chapter 1

Introduction

I am never content until I have constructed a mechanical model of the subject I am studying.
If I succeed in making one, I understand; otherwise I do not.

—Lord Kelvin, 1904

1.1 Complexity

One of the greatest scientific challenges of our time is to determine the mechanisms that give rise to human thought. Why is it that, given the enormous resources devoted to neuroscience research, a basic understanding of the brain remains elusive? Perhaps the problem is just one of scale—the human brain has on the order of 100 billion neurons and 100 trillion synapses. On the other hand, the molecules in a pitcher of water have more degrees of freedom, yet generate little interest. Perhaps the problem is that the brain is both large and *heterogeneous*? Or perhaps it is that the brain is highly *detailed* at the microscopic level? We are getting closer, but note that the lung also shares those properties, and yet is much more readily understood. We know intuitively that *something* is fundamentally different about the problem of the brain.

In 1948, Warren Weaver identified the reason. His key insight was that a broad class of problems from fields such as economics, political science, biology, and psychology all shared a common property, which he termed *organized complexity* (Weaver, 1948). The essential feature of organized complexity, and that which separates the brain from so many other systems is that, in addition to having very many variables, these variables are widely and deeply dependent on one another. While a single alveolus scarcely affects those around it, a single single neuron directly impacts the state of many other neurons, and in some cases can significantly alter the behavior of the brain as a whole. This property of massive interdependence of variables endows the brain with its unique properties, and also makes understanding the brain a monumental scientific task.

In the 65 years since Weaver's insight, the field of complexity theory emerged and has made great strides toward understanding the behavior of complex systems. As of 2001, at least 42 different definitions of complexity had been proposed (Lloyd, 2001). One common theme amongst many of them is *irreducibility*, the idea that a complex object, by definition, cannot be reduced to simple terms. Neuroscience often involves reducing the brain to its simplest pieces—molecules, neurons, or nuclei—with the assumption that by assembling the smaller components, we may learn more about the larger system. While this is generally true, it frequently neglects the fundamental issue of complexity—that by examining these smaller pieces in isolation, we can only guess the ways in which the organization of the pieces and interactions between them change their behavior.

In the same article, Weaver made another highly prescient observation: given our own inability to reason about complex systems, the use of "electronic computing devices" might allow these systems to be understood numerically rather than analytically. Indeed, computers are so deeply integrated into the methods of modern neuroscience that we scarcely notice the ways in which dealing with complexity has become commonplace. As the field of neuroscience continues to shift its attention toward systems of greater complexity, our ability to reason analytically about these systems will diminish, while computational modeling will continue to grow in capacity and ability.

1.2 Overview

This dissertation is not about modeling, but rather the process of measuring the parameters needed to generate physiologically realistic models. The behavior of complex systems depend in unpredictable ways on their inputs, and thus it is crucial in neuronal modeling to have reliable measurements of the neuronal substrate. The experiments described here place particular emphasis on the simultaneous measurement of many variables in the hope that a model based on these results will recapitulate as much of the underlying neuronal organization as possible. This approach has led to the development of novel and challenging techniques, and their description forms a large portion of this dissertation.

The sensory systems are very attractive for this type of research because their afferent input is relatively unprocessed, and thus much easier to understand and model. This project focuses on the cochlear nucleus, which is the first and only brain region to receive input from the auditory nerve. The cochlear nucleus has been characterized in great detail over several decades of research, with a particular emphasis on describing the anatomy and physiology of its primary neuron types. We have a thorough understanding of their responses to a wide variety of auditory stimuli, their intrinsic membrane properties, and even strong hypotheses about their primary functions in the auditory system.

Computational models have already been developed for several components of the cochlear nucleus, including auditory nerve input (Zilany et al., 2009), cell membrane properties, and synaptic kinetics (Banks and Sachs, 1991; Raman and Trussell, 1992; Rothman et al., 1993; Xie and Manis, 2013).

It would seem that we are well prepared to assemble a complete model of the cochlear nucleus; however, some crucial pieces of the puzzle are still missing. Most importantly, we lack a clear circuit map describing the local connectivity of interneurons. The reason for this is simple; until recently, the tools needed to probe this connectivity did not exist. Traditionally, connectivity has been measured by electrically stimulating a field of neurons while intracellularly recording from post-synaptic neurons. Such studies have been done in the cochlear nucleus (Ferragamo et al., 1998b; Wang and Manis, 2005; Xie and Manis, 2013), but this technique is confounded by its inability to selectively stimulate a single population of cells, particularly because electrical stimulation is believed to strongly activate axons, which are often densely intermingled in the stimulation field (Histed et al., 2009). A far less ambiguous approach is to record intracellularly from synaptically connected neurons, but this method is often too difficult to yield sufficient data, especially for neuron pairs that are separated by long distance. So while the existence of inhibitory interneurons has been clearly demonstrated, the circuit diagram has not. A more selective approach is to record intracellularly from pairs of neurons; however, such experiments are generally only feasible for very short-range connections.

Recently, techniques have been developed that allow spatially focal activation of neurons using laser photostimulation . Transgenic mice expressing channelrhodopsin are used to selectively stimulate the cell bodies and axons of genetically identified cells (Boyden et al., 2005), while caged glutamate photostimulation can be used to selectively stimulate the cell bodies of all cells (Katz and Dalva, 1994). The experiments in this dissertation use glutamate uncaging to measure connectivity within the cochlear nucleus circuit. Although this method lacks the genetic specificity of channelrhodopsin, it is particularly useful in the cochlear nucleus because all known interneuronal cell types are either anatomically separated or have distinctly identifiable synaptic properties (inhibitory vs excitatory). Since glutamate uncaging is generally only effective when directed at the soma of a neuron, this technique produces more definitive results by leaving fibers of passage unaffected. Furthermore, glutamate uncaging is much simpler as it does not require the use of transgenic animals.

This work describes the map of local inputs to the principal neurons of the mouse anteroventral cochlear nucleus (AVCN). These consist of at least two excitatory neuron classes, bushy cells and T-stellate cells (although bushy cells are often considered to consist of two different cell types, the distinction is less clear in mouse). Both cell types were found to receive input from three distinct, local inhibitory sources: tuberculoventral cells in the dorsal cochlear nucleus (DCN), D-stellate cells in the ventral cochlear nucleus

(VCN), and a third, unknown source at the dorsomedial boundary of the AVCN. Additionally, several cells had excitatory input from T-stellate cells in the AVCN. The input maps were registered with a 3D cochleotopic atlas to provide estimates of the input frequency to both pre- and postsynaptic cells, and subsequently analyzed to determine any relationships between input properties and postsynaptic cell types. Although both principal cell types received input from the same four sources, T-stellate cells had much more input from the VCN, while bushy cells had stronger input from the DCN. The difference in VCN input between the two cell types was particularly striking in that T-stellate cells received input from a wider frequency range than bushy cells. The functional implications of this result and others are explored in Chapter 6.

1.3 The cochlear nucleus and the auditory nerve

The cochlear nucleus is the first processing center for auditory information as it leaves the cochlea. It is also the *only* nucleus which receives direct input from the auditory nerve, and is thus an obligatory first step in the complex of auditory processing nuclei (Irvine, 1986). The cochlear nucleus is the source of at least five distinct ascending pathways, each of which encodes different aspects of the auditory stream and projects to several highly-interconnected nuclei in the brainstem and midbrain (Cant and Benson, 2003), and some of which project back to the cochlear nucleus. Downstream, these pathways are further processed by several subcortical nuclei before finally converging on the inferior colliculus (IC) in the midbrain, and from there the medial geniculate nucleus of the thalamus and ultimately auditory cortex (Oertel et al., 2002). In addition to the IC, output from the cochlear nucleus projects to the lateral lemniscus and several sub-nuclei with the superior olivary complex in the brainstem (Adams and Warr, 1976). The function of the lateral lemniscus is not well understood, but it is a major source of inhibitory input to the inferior colliculus, and thus may facilitate signal comparison there (Adams and Mugnaini, 1984). The superior olivary complex (SOC) is a cluster of multi-purposed nuclei which are most well known for their ability to encode the azimuthal location of sound sources by comparing interaural differences in the intensity and arrival time of signals from the cochlear nucleus (Goldberg and Brown, 1969). The axons of all three brainstem nuclei—CN, SOC, and LL—converge on the inferior colliculus, which combines information about acoustic features with sound localization and somatosensory inputs (Webster and Fay, 1992).

The complex network of auditory nuclei is believed to pre-process sound information to extract various acoustic features before being processed by the cortex. Crucially, neurons in the early auditory nuclei are some of the fastest in the brain, and thus are capable of performing computation on a much

finer timescale than would be possible by cortical neurons (Oertel et al., 2002). Although this system is still not well understood it is important to consider its functional requirements in order to constrain hypotheses about the output and purpose of the cochlear nucleus.

The function of the cochlear nucleus is likewise constrained by the afferent information available to it. The details of sound encoding in the auditory nerve are complex, but for the purpose of this discussion we may consider three primary components of the coding strategy. First, sound frequency is represented as a *place code*. A sound wave, like all continuous signals, may be represented as a combination of many different frequencies. The basilar membrane of the cochlea mechanically separates sound into its constituent frequencies and transmits vibration to the inner hair cells. Thus, each hair cell responds most strongly to a narrow range of sound frequency. This tonotopic organization is preserved in the spiral ganglion cells, in the auditory nerve input to the cochlear nucleus, and to varying degrees throughout the central auditory system (Oertel et al., 2002). Second, auditory nerve fibers use a *rate code* to represent the intensity of sounds within their receptive field. Most auditory nerve fibers have a limited dynamic range; their spike rate increases from the spontaneous rate to the maximum saturating rate after sound intensity has increased by about 30dB (Sachs and Abbas, 1974; Winter et al., 1990). Since the total dynamic range perceivable by most mammals is over 100dB, it follows that multiple auditory nerve fibers must be required within one frequency band to cover the entire range. Indeed, a single inner hair cell is contacted by about 20 spiral ganglion cells, each of which may encode a different portion of the dynamic range (Liberman, 1982). Spiral ganglion cells with a high spontaneous rate of firing are the most sensitive to quiet sounds (low threshold), while those with a low spontaneous rate are the most sensitive to loud sound levels (high threshold) (Sachs and Abbas, 1974). Third, a *time code* indicates the time of changes in the sound signal. For sounds with rapidly oscillating intensity (often sinusoidally amplitude-modulated tones in the literature), auditory nerve fibers may track the timing of intensity changes up to about 800Hz (Moller, 1974a; Frisina et al., 1990a). For low-frequency sound, they may track the timing of individual cycles in the sound wave (phase locking) up to 2-5kHz (Rose et al., 1967). Additionally, latency of the first spike following a sound onset is related to the intensity of the sound; louder sounds produce shorter latency to spike (Moller, 1975). These three coding mechanisms—place, rate, and time coding—are the basic input to the cochlear nucleus.

The cochlear nucleus has two major anatomical divisions: the dorsal (DCN) and ventral (VCN) cochlear nuclei, and the VCN is further comprised of anterior (AVCN) and posterior (PVCN) divisions (Figure 1.1). Fibers of the auditory nerve enter the cochlear nucleus at its ventral edge where they form the auditory nerve root which marks the boundary between AVCN and PVCN. In the nerve root, each fiber bifurcates into an “ascending” branch which extends through the AVCN and a “descending” branch which

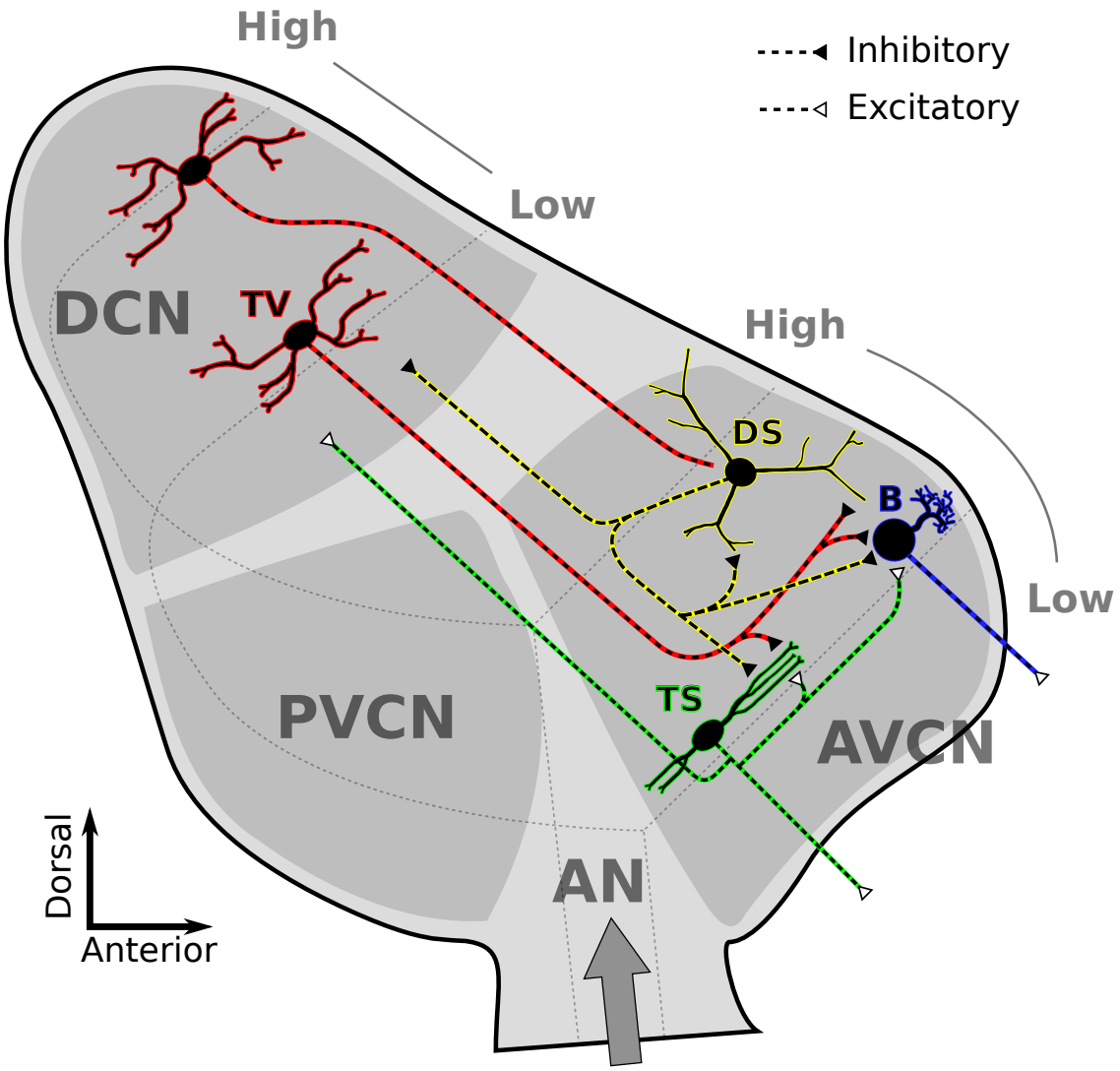

Figure 1.1: Schematic of putative AVCN circuitry. This is a sagittal view of the cochlear nucleus showing major subnuclei and a subset of cell types and circuitry relevant to the AVCN. Auditory nerve fibers **(AN)** enter the nucleus at the ventral edge then bifurcate into an "ascending" branch that innervates the AVCN and a "descending" branch that innervates the PVCN and DCN. AN fibers are organized tonotopically into sheets of similar frequency, with low frequencies near the ventral-lateral edge and high frequencies at the dorsal-medial edge. Bushy **(B)** and T-stellate **(TS)** cells are the primary excitatory output neurons of the AVCN and project ventrally to the trapezoid body. Both cell types integrate AN input from a narrow range of frequencies. D-stellate **(DS)** and tuberculoventral **(TV)** cells are inhibitory interneurons. TV cells project to bushy and T-stellate cells with a precise tonotopic registration. DS cells integrate from a wide range of AN fiber frequencies and have extensive axonal branching in the VCN and DCN. However, their postsynaptic targets are unknown, although they are believed to include both bushy and T-stellate cells. Some TS cells also have sparse local axon collaterals believed to synapse at least onto other T-stellate cells. Whether either of the inhibitory interneurons are the targets of any local projections is unknown.

passes through the PVCN, then turns dorsalward into the DCN (Cajal, 1909). In each cochlear nucleus subdivision, auditory nerve fibers are arranged in a precise tonotopic order with the lowest-frequency fibers occupying the ventrolateral edge and high-frequency fibers at the dorso-medial edge (Bourk et al., 1981; Muniak et al., 2013). The DCN integrates input from several sources including the VCN, the auditory nerve, and somatosensory afferents and is believed to compute azimuthal sound location by combining spectral cues and information about the head and pinna (Sutherland et al., 1998). The VCN has three major excitatory outputs. Octopus cells are found in an isolated pocket within the PVCN and are highly sensitive to the timing of broadband sounds (Rhode et al., 1983; Oertel et al., 2000). Bushy cells, which are most common in AVCN, are believed to preserve and enhance the fine temporal structure of their inputs. In contrast, T-stellate cells discard this fine temporal information and instead encode sound intensity on longer time scales (Shofner, 1999). Both bushy and stellate cells receive excitatory input from a very narrow frequency range of auditory nerve fibers (Bourk, 1976; Doucet and Ryugo, 2006).

The primary focus of this dissertation is the local interneuronal input to bushy and stellate cells in the AVCN. Information about this circuitry will help us to understand the function of the AVCN and the neuronal mechanisms that contribute to this function.

1.4 Principal cell types of the AVCN

While it is clear that distinct populations of cell types exist in the cochlear nucleus, the boundaries between them are not always clear, nor is it obvious which factors should be used to define those boundaries. Indeed, even the term “cell type” often lacks a clear definition, and numerous cochlear nucleus studies have discussed the difficulty of classifying cells (Pfeiffer, 1966; Godfrey et al., 1975; Rouiller and Ryugo, 1984; Rothman and Manis, 2003a; Typlt et al., 2012). Is a type defined by its input/output function, or by the set of inputs it receives, or the regions it projects to? The taxonomy of cell types in the cochlear nucleus, as with many other systems, has often been determined by the experimental technique in use. For example, the types “spherical”, “globular”, and “multipolar” appear in studies of Nissl preparations (Osen, 1969); “bushy” and “stellate” appear in Golgi preparations (Brawer et al., 1974); “primarylike”, “onset”, and “chopper” appear in single-unit studies (Kiang et al., 1965; Bourk, 1976; Rhode and Smith, 1986); and many numbered taxonomies have been adopted to describe a variety of physiological criteria (Evans and Nelson, 1973; Oertel, 1983; Shofner and Young, 1985). In many cases, cell types are organized into complex hierarchies when it is not clear which branch points in the hierarchy represent truly multi-modal distributions, and which simply represent the idealized cases at either end of a spectrum. There are also significant species differences; the variety and organization of cell types are

much less distinct in the mouse than in other species (Webster and Trune, 1982). Several studies have attempted to link these classification systems together by combining multiple measurements within cells, generally with good success (Cant and Morest, 1979a; Rhode et al., 1983; Rouiller and Ryugo, 1984; Oertel and Wu, 1984; Smith and Rhode, 1989).

The mouse AVCN has three *clearly* distinct cell types: bushy cells, T-stellate cells, and D-stellate cells. These three types differ on a wide range of physiological and anatomical properties, but in this case it is their axonal projections that unambiguously differentiate the types: T-stellate cells have excitatory projections to IC, SOC, and possibly DCN; bushy cells have excitatory projections only to the SOC; and D-stellate cells provide inhibitory projections to the DCN and contralateral cochlear nucleus (Cant and Benson, 2003). Many other differences exist between these three cell types, but in isolation none unambiguously determine cell type. How (and whether) these classes should be further subdivided is a matter of ongoing debate. This dissertation uses the nomenclature proposed by Oertel et al. (1990) because its intent is to indicate the projection patterns: D-stellate cells project to the **D**CN, whereas T-stellate cells project ventrally via the **t**rapezoid body.

1.4.1 Bushy cells

Bushy cells emphasize the fine timing structure of the auditory signal and send this to the SOC, where binaural comparisons of spike timing are used to compute the azimuthal sound location. They are further divided into two sub-categories. *Spherical* bushy cells project to the medial and lateral superior olives, which are both involved in azimuthal sound localization. *Globular* bushy cells project ipsilaterally to the lateral superior olive and contralaterally to the medial nucleus of the trapezoid body, which further projects to the lateral superior olive (Cant and Benson, 2003). However, the distinction between spherical and globular bushy cells is less clear in mice (Lauer et al., 2013). Both cell types cells *precisely* and *predictably* encode the timing of auditory events on a fast time scale (Joris et al., 1994; Shofner, 1999; Louage et al., 2005). Several cellular and synaptic specializations are combined to generate these behaviors.

Bushy cells have only one or two thick, short primary dendrites which end in compact, densely branched arborizations (Figure 1.2). The distal dentrites have only sparse synaptic input but are packed with large mitochondria, suggesting that these dendrites play a primarily metabolic role. The majority of the synaptic input is to the soma, proximal dendrite, and axon initial segment (Cant and Morest, 1979b). It is thought that the lack of distal dendritic input to bushy cells helps them to emphasize timing by avoiding dendritic filtering. Large, multi-site auditory nerve terminals provide strong and rapid input at synapses containing primarily AMPA receptors with a small fraction of NMDA receptors as well. These AMPA receptors are comprised mainly of GluR3 and 4 subunits, which endow these synapses with especially

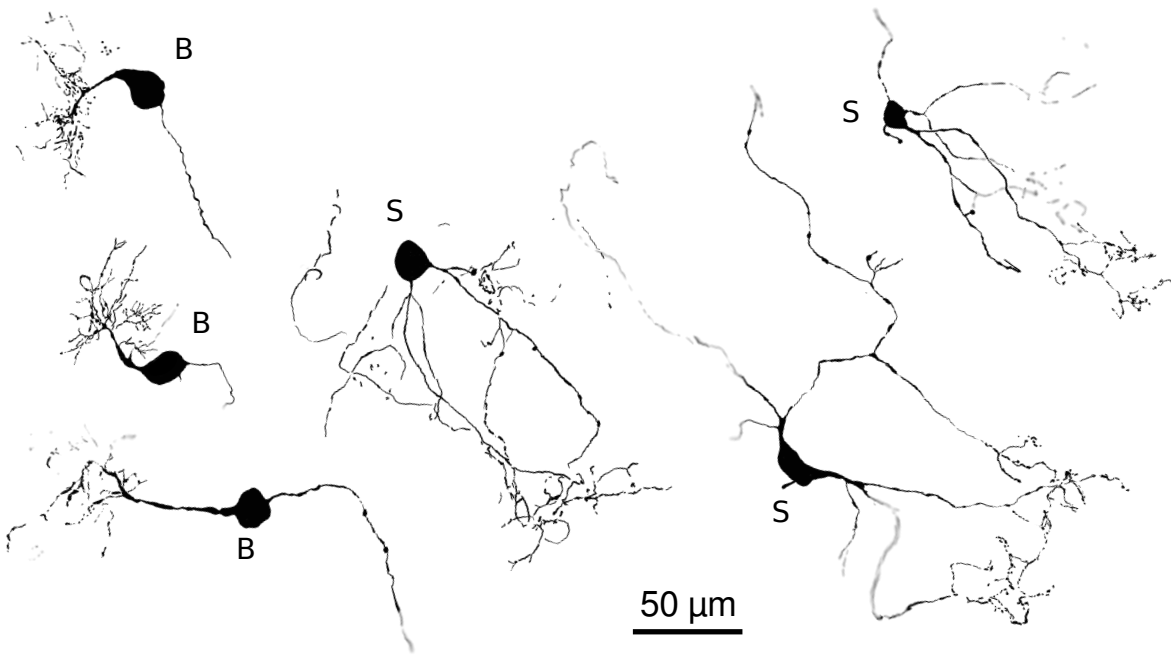

Figure 1.2: Reconstructions of cells with typical morphology. Bushy cells **(B)** have a single short primary dendrite which terminates in a compact and densely branched arbor. Stellate cells **(S)** have longer, more sparsely branching dentrites which often end in small tufts. The dendrites of T-stellate cells are restricted to a narrow plane parallel to the isofrequency sheets.

rapid kinetics (Hunter et al., 1992; Ryugo and Parks, 2003). Due to the precise tonotopic arrangement of auditory nerve fibers, bushy cells receive their primary input from fibers spanning a very narrow frequency band. Furthermore, anatomical evidence suggests that bushy cells tend to receive input from auditory nerve fibers of similar spontaneous rate (Fekete et al., 1984; Sento and Ryugo, 1989; Liberman, 1991). Thus the primary input to bushy cells appears to come from a homogeneous set of fibers.

Several criteria have been proposed for identifying cell types based on responses recorded from the extracellular potentials generated by single neurons. The most common in the cochlear nucleus is the post-stimulus time histogram (PSTH), which plots the probability of a neuron firing at any particular time after the onset of a stimulus (usually a short tone). Many neurons in the cochlear nucleus may be identified by simple visual inspection of their PSTH (Figure 1.3; Blackburn and Sachs, 1989). Bushy cells are known to have PSTHs which appear qualitatively similar to those of auditory nerve fibers, and are thus termed "primarylike" in single-unit studies (Rhode et al., 1983; Rouiller and Ryugo, 1984). At higher intensity, some units (most often globular bushy cells) develop a brief (0.5 ms) notch in the PSTH following an initial highly reliable spike, which is thought to be due to the refractory period of the cell (Bourk, 1976; Smith and Rhode, 1987). Given the relative strength, speed, and homogeneity of their inputs, it is perhaps unsurprising that bushy cells have such similar response properties to their primary input. However,

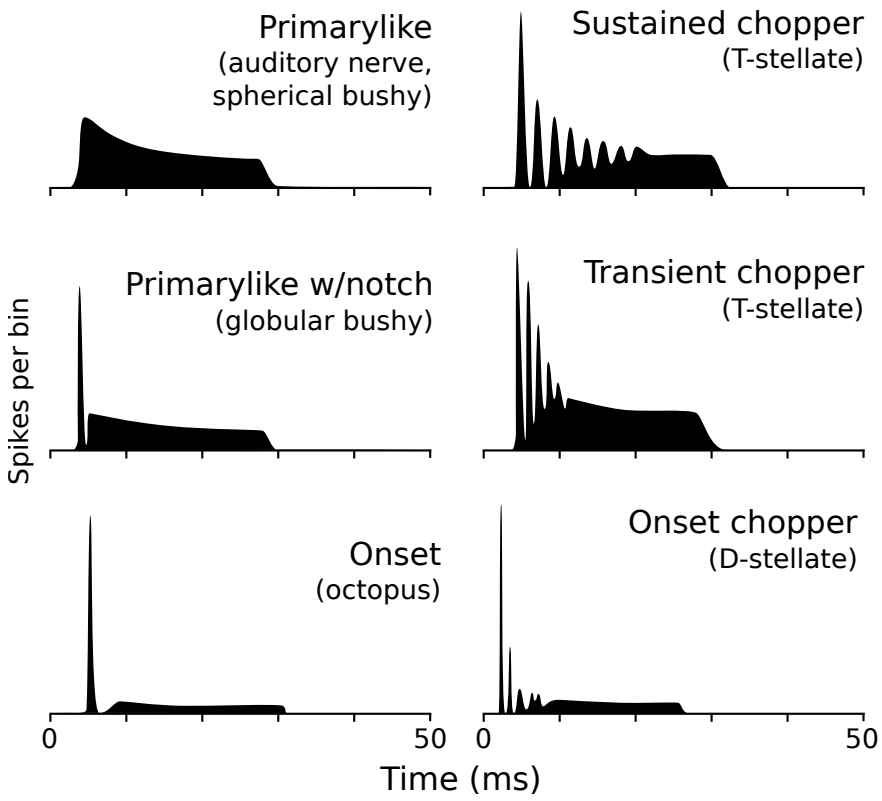

Figure 1.3: Common post-stimulus time histograms (PSTH) of VCN units. These plots show the probability of spiking over time during a brief tone. The variety of response types is due to a combination of differences in cell membrane properties and excitatory and inhibitory input properties. Bushy cells have both primarylike (at low intensity) and primarylike-with-notch (at high intensity) response types. T-stellate cells have sustained and transient chopper response types. D-stellate cells have onset chopper response types. Adapted from Rhode and Smith (1986); Blackburn and Sachs (1989).

bushy cells integrate input from multiple auditory nerve fibers (Spirou et al., 2005; Cao and Oertel, 2010), and therefore are not merely relay cells. Their responses differ from their primary input in important but subtle ways which have been revealed through several key studies over the last few decades.

To maintain rapid firing, it is not enough for a neuron to receive fast excitatory input, as bushy cells do. In a typical neuron, such strong excitatory inputs would cause large membrane depolarizations that would subsequently delay repolarization. The time constant for repolarization is determined largely by the capacitance and conductance of the cell membrane. Bushy cells (and many others in the auditory system) have an atypically high membrane conductance to allow rapid repolarization. This extra conductance is provided in part by a specialized potassium conductance (I_{LT}) which is partially open at resting potential, and which further opens at a low voltage threshold (Manis and Marx, 1991; Rothman and Manis, 2003a).

Perhaps more importantly, I_{LT} reduces the probability that a cell will fire multiple spikes in response to a tonic input (Rothman and Manis, 2003b). This is seen in current-clamp recordings of bushy cells where injection of a constant level of current elicits a single action potential, followed by a steady depolarization until the current is removed (Oertel and Wu, 1984). Effectively, bushy cells are more sensitive to the *derivative* of their input than the absolute level (McGinley and Oertel, 2006). The ability to fire selectively at the onset of a constant input is crucial for bushy cell function, since the timing of spikes in auditory nerve fibers becomes more unpredictable past the onset (Rhode and Smith, 1985).

Put another way, bushy cells respond most reliably when their individual auditory nerve inputs are synchronized, as this produces a sharp depolarization in the membrane, while unsynchronized inputs may be rejected as noise. This suggests an important reason for the homogeneity of bushy cell inputs: only auditory nerve fibers encoding similar aspects of the sound are expected to be consistently synchronized. Furthermore, by integrating the responses of multiple auditory nerve fibers, bushy cells are able to combine the timing of these inputs and output a signal that is far more precise (Joris et al., 1991, 1994).

The ability to fire with very precise timing is perhaps the most important aspect of bushy cell function, and is thought to play a key role in enabling binaural neurons in the medial superior olive to compute the azimuthal location of sound by comparing interaural differences in the arrival of sound (however, this mechanism is thought to be absent in mice due to their lack of low-frequency hearing and small interaural distance) (Smith et al., 1993). Precise and predictable timing is also important in the lateral superior olive, which computes sound location in part by comparing interaural differences in sound intensity. While bushy cells have very precise spike timing, the absolute latency from sound onset to spike is affected by the intensity of the sound—louder sounds produce faster responses. Thus, the lateral superior olive may compute interaural level differences by again comparing the timing of bushy cell

inputs bilaterally (Goldberg, 1975; Irvine et al., 2001; Bures and Marsalek, 2013). In both cases, timing precision is critical to accurately estimating sound location.

In addition to their primary excitatory input, bushy cells receive inhibition from several sources within the VCN, DCN, and SOC, for which many functions have been proposed. These are central to the topic of this dissertation and will be examined in detail in Sections 1.6 and 1.5.

1.4.2 T-stellate cells

Bushy cells appear to be most sensitive to rapid changes in the sound level. This high-pass characteristic makes them sensitive to fine temporal structure, but less sensitive to sustained sound levels. T-stellate cells provide an output stream that is complementary to bushy cells by suppressing the finest temporal information in favor of a highly regular firing rate that encodes amplitude on slower timescales (White et al., 1994; Shofner, 1999). In single-unit studies, these cells are termed "choppers" because of the characteristic chopping pattern seen in their PSTH, which is due to a highly stable inter-spike interval (Figure 1.3). This interval is strongly dependent on the sound level, but is insensitive to the fine temporal structure (Rhode and Smith, 1986; Smith and Rhode, 1989). Likewise, T-stellate cells lack the I_{LT} current found in bushy cells and thus respond to constant current injection with sustained, regular spiking (Oertel and Wu, 1984; Manis and Marx, 1991; McGinley and Oertel, 2006).

In anatomical studies, T-stellate cells are often referred to as "planar multipolar" cells because their long, sparsely-branching dendrites extend preferentially within a narrow isofrequency sheet (Figure 1.2; Oertel et al., 1990; Palmer et al., 2003; Doucet and Ryugo, 2006). Planar multipolar morphology has been linked to both chopper unit types (Rhode et al., 1983; Rouiller and Ryugo, 1984) and intracellular recordings of regularly-spiking cells (Oertel and Wu, 1984). Compared to bushy cells, this dendritic organization allows integration of more distal auditory nerve inputs while still maintaining sharp frequency selectivity. Ultrastructural studies (in which T-stellate cells are often called "Type I") have shown that, while the somas of T-stellate cells receive little synaptic contact, the dendrites are heavily innervated (Cant, 1981; Smith and Rhode, 1989; Josephson and Morest, 1998). This finding has led some to suggest that T-stellate cells rely on dendritic filtering to temporally smooth inputs from the auditory nerve, thus promoting more regular firing and more accurate representation of the input amplitude (Young et al., 1988; Banks and Sachs, 1991; White et al., 1994). Additionally, these inputs are mediated by AMPA receptors that contain GluR2, giving them significantly slower kinetics than in bushy cells (Cao and Oertel, 2010).

T-stellate cells are thought to comprise a heterogeneous group of cell types based on several criteria. Schofield and Cant (1996) showed that T-stellate cells project to either the ipsilateral or contralateral

inferior colliculus, but never both, suggesting two different classes. Single-unit studies have identified multiple classes of chopper PSTH: sustained choppers have the most regular interspike interval, whereas transient choppers and slowly-adapting choppers have more complex response patterns (Blackburn and Sachs, 1989), and onset choppers represent an entirely different class of neuron (discussed below). The functional significance of the wide variety of T-stellate subtypes is unclear. Furthermore, it remains to be determined whether these subtypes should be considered distinct populations or a single population with a diversity of response properties.

It should be emphasized that, although we separate bushy and stellate cells as encoding either timing or sound level, this description is not complete. We must also specify *on what timescale* stellate cells encode sound level. In some respects, bushy cells may be thought to encode sound level at the shortest possible timescale (in the frequency domain, a derivative is just a high-pass filter). T-stellate cells encode level on a longer time scale, albeit one that is still quite rapid; perhaps less than 10 ms (White et al., 1994), and the variety seen in response types may simply reflect processing at different points along this continuum. One common way to measure the timescale over which a cell processes its input is to modulate the amplitude input rapidly, then vary the frequency of this modulation to see where the cell responds most strongly. Numerous studies have examined the responses of cochlear nucleus units to amplitude modulated sound (Moller, 1974a; Frisina et al., 1990a; Rhode and Greenberg, 1994a; Wang and Sachs, 1994). These generally agree that most cell types in the VCN have an enhanced sensitivity to amplitude modulation compared to their primary input, and that this sensitivity differs in strength and tuning across cell types.

The enhanced representation to modulated sound is particularly apparent at high intensity, which is important because it poses a solution to the dynamic range problem introduced earlier: normal hearing spans an intensity range of over 100 dB, yet the firing rate of individual T-stellate and bushy cells saturates at about 30 dB past their lowest threshold (Smith and Rhode, 1989). However, if the sound is amplitude modulated, then the same cells are able to encode this modulation (either by modulating their own firing rate, or by synchronizing to the modulation envelope) over a much larger dynamic range, up to 90 dB in some studies (Frisina et al., 1990b). This reinforces that, for many cell types, there is a preference for encoding rapid changes in the sound level, rather than a constant level. Consistent with this interpretation, it has been found that primarylike-notch units have better synchronization than choppers (Wang and Sachs, 1994; Rhode and Greenberg, 1994a). Transient choppers were also found to have enhanced synchronization relative to sustained choppers, indicating that T-stellate subclasses may differ in their temporal selectivity.

1.4.3 D-stellate cells

The third major class of neurons in the cochlear nucleus are inhibitory interneurons called D-stellate cells. These cells have long, sparsely-branching dendrites that radiate in all directions, and are thus referred to as "radiate multipolar" in some anatomical studies (Oertel et al., 1990; Doucet and Ryugo, 1997; Palmer et al., 2003). The axons of D-stellate cells branch profusely within the ipsilateral and contralateral cochlear nuclei, and are believed to provide glycinergic input to both bushy cells and stellate cells of all types (Doucet et al., 1999). Unlike T-stellates, the synaptic inputs to D-stellate cells (often called "Type II" in ultrastructural studies) are more dense at the soma and proximal dendrites (Cant, 1981; Smith and Rhode, 1989).

In single-unit studies, D-stellate cells are described as having an "onset chopper" PSTH, which shows a strong and highly precise onset response followed by much weaker, irregular firing (Figure 1.3; Rhode and Smith, 1986; Smith and Rhode, 1989; Arnott et al., 2004). Consistent with the dendritic architecture of D-stellate cells, onset chopper units lack the sharp frequency tuning seen in auditory nerve fibers, and instead respond more strongly to broadband sounds (Figure 1.4; Rhode and Smith, 1986; Palmer et al., 1996). These two features–temporal precision and spectral breadth–can be understood in the context of a fundamental mathematical limit: much like the tradeoff between temporal precision and level precision discussed earlier, there exists an analogous tradeoff between temporal precision and spectral precision. In the case of D-stellate cells, Palmer et al. (1996) have suggested that the *cost* of having very high temporal precision is the requirement that these cells integrate a broader range of frequencies. It has also been found that onset chopper units have a much broader dynamic range (up to 90 dB) and stronger representation of amplitude-modulated sound than both sustained chopper (T-stellate) and primarylike (bushy) units (Smith and Rhode, 1989; Wang and Sachs, 1994).

It is clear that these cells have a peculiar array of physiological properties (Rhode and Smith, 1986); however, due in part to the relative scarcity of D-stellate cells in the cochlear nucleus, their physiology and function are not well understood. As one of the primary inhibitory interneurons in the cochlear nucleus, these cells are central to the topic of this dissertation.

1.4.4 Tuberculoventral cells

Another cell type which warrants introduction is the tuberculoventral cell of the DCN. Although these cells do not reside within the VCN, they provide a strong inhibitory projection into the VCN (Wickesberg et al., 1991) and thus figure prominently in this research. Tuberculoventral cells are glycinergic interneurons which reside in the deep layer of the DCN and are thought to receive excitatory

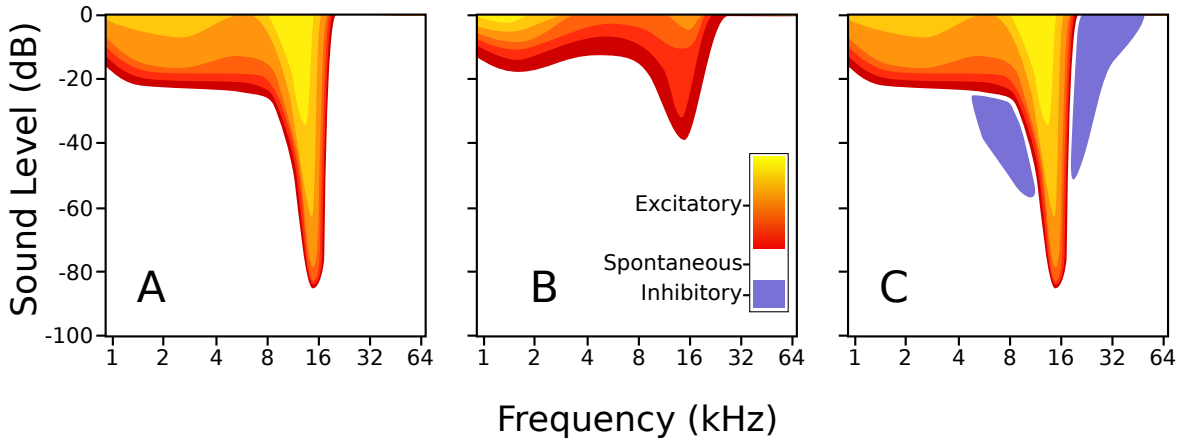

Figure 1.4: Typical frequency-response areas of VCN units. These maps are generated by playing a series of short tones of various frequency and intensity while recording extracellular potentials. **A)** Typical response of auditory nerve fibers, bushy cells, and T-stellate cells. These cells have sharp tuning at moderate intensities and broad tuning extending toward low frequency at higher intensity. **B)** Typical D-stellate response pattern, indicating broad tuning and high thresholds to pure tones. **C)** Example response pattern with inhibitory sidebands. Inhibitory areas are detected as a decrease in the spontaneous rate of firing. Adapted from Palmer et al. (2003).

input from both auditory nerve fibers and T-stellate cells in the VCN (Feng and Vater, 1985; Wu and Oertel, 1986; Zhang and Oertel, 1993; Muniak and Ryugo, 2013), as well as inhibitory input from other tuberculoventral cells (Kuo et al., 2012). The dendrites of tuberculoventral cells extend within isofrequency sheets in the DCN similarly to T-stellate cells, resulting in exposure to a narrow frequency range of auditory input (Oertel and Wu, 1989). Likewise, their axons project separately to narrow frequency bands in the three major cochlear nucleus divisions, and these projections are tonotopically matched to the dendritic field of the cell (Oertel and Wu, 1989; Wickesberg and Oertel, 1988). This connectivity has also been demonstrated functionally in a study by Wickesberg and Oertel (1990), in which focal application of glutamate to the DCN elicited inhibitory responses in both bushy and stellate cells in the AVCN.

In keeping with their dendritic architecture, tuberculoventral cells have a narrow frequency tuning similar to that of auditory nerve fibers. However, they also have comparatively high thresholds (Young and Brownell, 1976; Young and Voigt, 1982) and thus may selectively exclude low-threshold inputs. They fire regularly and reliably in response to constant current injection (Zhang and Oertel, 1993; Kuo et al., 2012). Together, the physiological features of tuberculoventral cells demonstrate a source of inhibition that is in many ways complementary to that provided by D-stellate cells: tuberculoventral cells are narrowly tuned and have sustained firing in response to tonic excitation, whereas D-stellate cells are broadly tuned and have a strongly phasic firing pattern. Although the function of these two inhibitory sources is a topic of active debate, much of the evidence suggests that D-stellate cells provide a source of temporally-precise

spectral contrast, whereas tuberculoventral cells provide a spectrally-precise *temporal contrast*. The functional significance and consequences of these inhibitory schemes are discussed in Section 1.6.

1.4.5 Other cell types

Collectively, bushy, T-stellate, and D-stellate cells dominate the AVCN literature. There are, however, more cell classes that make occasional appearances and have a minor role in this study. First, Ferragamo et al. (1998a) described Golgi cells that reside in the granule cell lamina which covers the lateral surface of the VCN. These cells are believed to be a source of GABAergic inhibition within the granule cell layer; however, there is scant evidence for any communication between the granule cell layer and the magnocellular core of the VCN, with the exception that the distal dendrites of some stellate cells are found near the granule cell layer (Ferragamo et al., 1998b).

Second, a small population of stellate cells with short dendrites has been identified around the margins of the VCN (Doucet and Ryugo, 1997, 2006). Recordings from these cells indicate that they have a peculiar array of properties including either wide dynamic ranges or lack of sensitivity to auditory input (Ghoshal and Kim, 1996a,b, 1997), although it is not clear what cell types were recorded from in these studies. Shore et al. (2000) found anatomical evidence for trigeminal input to the marginal shell of the VCN, raising the possibility that marginal cells may integrate multisensory inputs.

1.5 The AVCN circuit

The major cell classes described above—two excitatory output neurons, two inhibitory interneurons, and the spiral ganglion cells that give rise to the auditory nerve—form the basic components of the AVCN circuit. This section reviews the research describing the synaptic connectivity between these elements. The literature on this topic is comprised mainly of two types of study. Anatomical studies provide the best possible resolution for describing individual components of the circuit, but because these measurements are made on fixed tissue, they present only a static view and tell us little about the functional significance of synaptic connections. On the other hand, physiological studies typically measure the function of the intact system, but have little resolution for distinguishing the contributions of individual components. Those experiments which straddle the border between anatomical and physiological are traditionally difficult and rare, but provide a wealth of new information by bridging the gaps between these two disparate parts of the literature.

1.5.1 Anatomy of the AVCN circuit

Ultrastructural studies have determined the location and structural properties of synapses on each of the major AVCN cell types. Although these studies are not able to identify the sources of each type of synapse, predictions can be made based on synaptic and vesicular appearance. In electron microscopy studies, two broad classes of synapse have been identified. Excitatory synapses usually have an asymmetric synaptic density and spherical vesicles, while inhibitory synapses usually have symmetric density and flattened or pleomorphic vesicles (Colonnier, 1968; Peters et al., 1991).

Bushy cells have at least four types of synapse (Cant and Morest, 1979b; Tolbert et al., 1982; Smith and Rhode, 1987; Ostapoff and Morest, 1991). Auditory nerve terminals contain large, spherical vesicles and form multi-site synapses on the soma and axon initial segment. A study by Spirou et al. 2005 measured the prevalence of auditory nerve synapses onto globular bushy cells and concluded that most cells receive input from 15–23 independent fibers. Symmetric synapses containing flattened and pleiomorphic vesicles are also found primarily on the soma and axon initial segment. The fourth type of synapse is asymmetric with small spherical vesicles and is found sparsely on the distal dendrites. These studies demonstrate conclusive evidence for non-primary input to bushy cells and place a lower bound on the number of input types we expect to find. In addition, Gómez-Nieto and Rubio (2009, 2011) have described possible junctional coupling between the dendrites of bushy cells; however, such coupling has not been demonstrated electrophysiologically.

With the exception of auditory nerve terminals, the cells which form synapses onto bushy cells have not been identified. Smith and Rhode (1989) reported that the axons of onset-chopper units (D-stellate cells) contained pleomorphic vesicles, while those of sustained chopper units (T-stellate cells) contained small spherical vesicles. This suggests that D-stellate cells have sparse synaptic terminals on the soma of bushy cells, while T-stellate cells provide sparse input to the distal dendrites.

In ultrastructural studies of multipolar cells, two major categories have been described. Type I, believed to be T-stellate cells, has little somatic contact and dense dendritic contact, whereas type II, believed to be D-stellate cells, has dense somatic dendritic contact. The distal dendrites of both types are sparsely innervated (Smith and Rhode, 1989). Like bushy cells, both types have asymmetric synapses with large and small spherical vesicles, as well as symmetric synapses with flattened and pleiomorphic vesicles (Cant, 1981; Josephson and Morest, 1998; Smith and Rhode, 1989; Friedland et al., 2003). Thus, although the same synapse types are present on all three cell types, their distribution and prevalence are different. The location of synapses is of particular interest in the auditory system because it processes information so rapidly that even a small amount of dendritic filtering can have a significant effect on the function of fast

synaptic events.

Anatomical studies using light-microscopy of retrograde and anterograde tracers have provided a complementary picture by describing the patterns of axonal and dendritic projection. Tuberculoventral cells have dendritic and axonal fields in all three major cochlear nucleus divisions that are restricted to narrow frequency ranges (Feng and Vater, 1985; Wickesberg and Oertel, 1988; Oertel and Wu, 1989), although some studies have described sparse tuberculoventral terminals a short distance from the central frequency projection (Munirathinam et al., 2004). Furthermore, the projection regions of a single tuberculoventral cell appear to be tonotopically matched, since they follow the projections of labeled auditory nerve fibers. T-stellate cells follow a similar pattern, having both dendritic and axonal fields that are largely restricted to narrow-frequency sheets. The axons of T-stellate cells project ventrally to exit the cochlear nucleus, but also give rise to axon collaterals in both VCN and DCN (Oertel and Wu, 1984; Smith and Rhode, 1989; Oertel et al., 1990; Friedland et al., 2003). While D-stellate cells also have tonotopically-matched projections to VCN and DCN, both their dendritic and axonal fields extend over a much wider frequency range, within about 1 octave of the location of the soma (Smith and Rhode, 1989; Oertel et al., 1990; Arnott et al., 2004; Doucet and Ryugo, 2006). Additionally, D-stellate cells have inhibitory projections to the contralateral cochlear nucleus, which have been more extensively studied due to the relative ease with which they can be selectively labeled and activated (Cant and Gaston, 1982; Wenthold, 1987; Shore et al., 1991; Doucet and Ryugo, 2006). Bushy cell axons exit the cochlear nucleus ventrally and have no axonal collaterals.

In addition to local connectivity within the cochlear nucleus, a large body of literature has described evidence for descending input onto VCN cells, including projections from the superior olivary complex (Spangler et al., 1987; Brown et al., 1988; Shore et al., 1991; Mulders et al., 2008) and trigeminal nuclei (Shore et al., 2000; Dehmel et al., 2008). These inputs likely play a significant role in the behavior and output of the cochlear nucleus, but are beyond the scope of this report.

From the anatomical and ultrastructural studies discussed above, a coherent picture has emerged in which D-stellate cells provide wideband inhibition to VCN, tuberculoventral cells provide narrowband inhibition, and T-stellate cells provide narrowband excitation. These studies are consistent with the interpretation that all three VCN cell types are the recipients of all three interneuronal projections, but this has not been conclusively demonstrated.

1.5.2 Physiology of the AVCN circuit

Whereas anatomical descriptions of circuitry provide a time-frozen snapshot of the substrate on which neuronal circuits are built, electrophysiological methods provide a complementary approach that

preserves the dynamic interplay of components. Often, the cost of this high-level, functional view is that it becomes more difficult to determine the contributions of individual components. The next two sections present a selection of the cochlear nucleus physiology literature that focuses on the secondary inhibitory and excitatory inputs to AVCN neurons.

Early single-unit studies described the suppression of spontaneous spiking in response to short tones in VCN neurons. In these responses, suppression is apparent either during the tone, or for a short period following the offset. Although multiple excitatory and inhibitory responses may be combined to determine the final spike rate, these experiments suggest that the inhibitory inputs to VCN cells have different spectral and temporal properties than their excitatory inputs, and that the strength of inhibition varies widely from cell to cell (Starr and Britt, 1970; Evans and Nelson, 1973; Brownell, 1975). Units are often characterized by measuring their frequency response area, which is a 2-dimensional map describing the neuron's spike rate in response to short tone stimuli over a range of frequency and intensity (Figure 1.4). Bushy and T-stellate cells both approximate the auditory nerve in their excitatory response areas–a sharp peak of elevated sensitivity at the cell's characteristic frequency, and increasing sensitivity to broader frequency bands as intensity increases (Bourk, 1976).

T-stellate and globular bushy cells are often found to have suppression in sidebands flanking the central excitatory response area, while such suppression is rarely seen in D-stellate and spherical bushy cells (Brownell, 1975; Martin and Dickson, 1983; Smith and Rhode, 1989; Spirou et al., 1990; Rhode and Greenberg, 1994b). Sideband suppression is usually found within 1/2 to 3/4 octaves from the cell's central frequency, which has led many to hypothesize inhibition from D-stellate cells is the cause of this suppression (Martin and Dickson, 1983; Smith and Rhode, 1989). However, an anatomical study by Ostapoff et al. (1999) found tuberculoventral terminals in a fringe outside the expected central-frequency band, suggesting that these may also provide off-center frequency inhibition.

Experiments measuring the intracellular potential in response to external stimulation are somewhat more difficult, but provide useful information about the subthreshold signals being integrated by the cell. Importantly, this provides a measure of inhibitory influence even in the absence of spontaneous firing, whereas extracellular recordings require spontaneous activity in order to measure suppression. Electrical stimulation of the auditory nerve evokes both inhibitory and excitatory polysynaptic events in cochlear nucleus slices (Oertel, 1983; Ferragamo et al., 1998b) and in whole-brain preparations (Ryugo et al., 2003). In slices, evoked inhibitory events were seen even after removal of the DCN, which strongly suggests the activation of D-stellate inputs. Furthermore, injection of glutamate into the DCN was found to elicit rapid trains of inhibitory events in the VCN. As predicted anatomically, the location of DCN injection sites that successfully evoked inhibition was related tonotopically to the location of the postsynaptic cell

(Wickesberg and Oertel, 1990). In most cases, inhibitory events were found to outlast the primary excitatory input, either by continuing to fire well past the end of the stimulus, or by simply having slower decay kinetics. Xie and Manis (2013) found that the decay time constant of inhibitory events is longer in bushy cells than in stellate cells, raising the possibility that the same sources of inhibition may have different functional properties depending on the target cell type.

When taken together, the evidence generated by anatomical and physiological experiments present a coherent picture of connectivity within the VCN. It is clear that D-stellate cells are a source of broadband inhibition, and that these cells likely provide direct input to bushy and stellate cells. Tuberculoventral cells are a source of narrowband inhibition and have been more conclusively shown to provide inhibitory input to the same sets of cells. Due to the relative scarcity of D-stellate cells, it is not clear what types of inhibition they might receive, although they do appear to have the same types of synapses as other cell types at the ultrastructural level. Additionally, T-stellate cells are believed to provide a local source of excitation, although no direct evidence exists for this.

What remains is to determine more precisely the patterns of connectivity—what is the probability of connection between any two cell types, how is that probability distributed spatially (or over across other non-spatial properties), and what is the total convergence? Additionally, the synaptic strength and kinetics between each pair of cell types must be determined. In the past, these parameters have been difficult to measure experimentally due to the difficulty of selectively activating specific components of the circuit. This has been particularly difficult in the case of D-stellate cells, which are both sparse and wholly interspersed with other cell types in the VCN. Finally, generating and testing hypotheses about the functional significance of each type of connection, and about the coordinated activity of the complete circuit, will require careful modeling and new experimental approaches.

1.6 The function of interneurons in the AVCN

Although there is much we do not know about the local circuit connectivity in the cochlear nucleus, many hypotheses have been put forth to describe the functional relevance of the interneuronal connections in the AVCN. In the following section, these are organized broadly into three categories based on the type of information they operate on: frequency, intensity, and time. In general these effects are not mutually exclusive, and in many cases, may even be complementary interpretations of the same basic mechanism.

1.6.1 Spectral effects of inhibition

One of the most frequently proposed inhibitory functions is that lateral inhibition leads to spectral sharpening in the responses of bushy and T-stellate cells (Rhode and Greenberg, 1994b; Kopp-Scheinpflug et al., 2002). This follows from evidence for similar mechanisms such as in the retina, where lateral inhibition aids in defining the boundary between the receptive fields of adjacent cells. However, this issue remains controversial since a number of studies found no effect of inhibition on the spectral width of excitatory response areas (Brownell, 1975; Palombi and Caspary, 1992; Caspary et al., 1994). A closely related idea suggests that lateral inhibition results in selectivity for signals that are spectrally narrow (Palmer et al., 1996). That is, rather than decreasing sensitivity to adjacent tones, lateral inhibition decreases sensitivity to broadband sounds. Thus, cells become more sensitive to spectral *peaks* that are within the excitatory response area. This interpretation is somewhat more consistent with the broadband response properties of D-stellate cells.

To further refine the idea of spectral peak detection, we must consider that the background noise we seek to eliminate is also changing rapidly in time. Thus, to improve peak detection in a noisy background requires that the source of broadband inhibition be able to follow rapid fluctuations in the noise level. This is the basis the psychophysical phenomenon known as comodulation masking release (CMR; Hall et al., 1984), in which a narrow-band signal is hidden within a masker of similar frequency, but becomes detectable if the bandwidth of the masker is increased. In the VCN, chopper units are found to have the best CMR sensitivity (Pressnitzer et al., 2001), and a model by Xie and Manis (2013) suggests that this relies upon inhibition combining both broad-band excitability and rapid kinetics.

1.6.2 Inhibitory effects on dynamic range

Inhibition has also been proposed in numerous studies to optimize the dynamic range and gain control of the neuron (Frisina et al., 1990b; Caspary et al., 1994; Backoff et al., 1999; Kopp-Scheinpflug et al., 2002; Mulders et al., 2008). In sensory systems, dynamic range refers to the range over which a stimulus may vary before the spike output of a neuron no longer responds to further changes. This is most commonly measured in reference to the mean spike rate of a neuron, but may use any other metric (or combinations of metrics) such as the timing of spikes, the synchronization of ensembles, etc. For example, if we consider the output of a neuron simply as its mean spike rate, there is a fundamental limit on this output extending from zero (no spiking) up to the maximum firing rate determined by the refractory period of the cell. In the presence of background noise, the resting spike rate might increase, causing the output range available for encoding changes in the sound level to become compressed. In extreme cases,

the firing rate may become saturated and no new information can be encoded by adding spikes. A closely related concept is gain control, which determines the *scale* of the dynamic range in relation to the neuron's output.

Dynamic range optimization and gain control take several closely-related forms in the literature. Rhode and Greenberg (1994b) suggested that lateral inhibition helps to optimize the dynamic range in the presence of broadband background noise. Caspary et al. (1994) showed that blocking inhibition increases the spike rate in the center-frequency area of the cell, and suggested that inhibition provides gain control to improve signal detection in noise. Ebert and Ostwald (1995b) showed that moderate levels of inhibition suppresses spontaneous activity with little effect on evoked activity, and likewise suggested that inhibition improves the signal-to-noise ratio for acoustic transients in noise. Mulders et al. (2008) showed that background noise reduces the dynamic range of VCN cells, while stimulation of the olivocochlear bundle, which provides descending GABAergic input to the cochlear nucleus, restores much of that dynamic range by shifting the cell's rate-level function. Finally, Xie and Manis (2013) have suggested that slow inhibitory input to bushy cells provides gain control by maintaining the membrane potential at the optimal level for I_{LV} activation. Although the details of these experiments vary widely, their conclusions follow a common theme wherein inhibition helps to reduce the effect of various unwanted signals, while increasing the dynamic range available for representing signals of interest.

Cochlear nucleus neurons are also found to have greater dynamic range for representing amplitude-modulated sounds than constant-amplitude sounds. Whereas most units have saturated firing rate at 20–40 dB above their threshold, the same units may be sensitive to amplitude modulation up to 90 dB above threshold (Moller, 1974b; Frisina et al., 1990b). Additionally, cochlear nucleus neurons are more sensitive than auditory nerve fibers to amplitude-modulated sound, particularly at high intensity. This indicates that mechanisms intrinsic to the cochlear nucleus are responsible for optimizing sensitivity to amplitude modulation. Backoff et al. (1999) showed that blocking inhibition reduces the ability of PVCN neurons to synchronize to the envelope of amplitude modulated sound, and suggested that inhibition improves sensitivity to modulation by ensuring that the spike rate does not saturate.

1.6.3 Temporal effects of inhibition

Both bushy and stellate cells employ a variety of mechanisms to ensure that spike timing is carefully controlled. Bushy cells preserve the very precise timing of auditory events while modulating that timing to encode signal intensity. Stellate cells, on the other hand, generate a variety of precisely controlled spiking patterns that are invariant to rapid changes in their excitatory input. In both cases, inhibition is thought to contribute to timing control.

At least three types of chopper have been identified in single unit recordings based on PSTH shape. Sustained choppers have a highly regular interspike interval, while adapting choppers have an initial decrease in spike rate lasting either less than 10 ms (transiently-adapting chopper) or greater than 20 ms (slowly-adapting chopper). Several studies have investigated the mechanisms underlying these response types. In chopper units, inhibition increases first spike latency and decreases both regularity and spike rate, particularly during the sustained portion of the response (Palombi and Caspary, 1992; Ebert and Ostwald, 1995a; Paolini et al., 2004, 2005; Gai and Carney, 2008b). However, the effects of inhibition do not appear to be strong enough to entirely explain the differences between sustained and transient chopper response types (Paolini et al., 2005; Gai and Carney, 2008a).

In response to short tone bursts, the spike rate of auditory nerve fibers is initially high and decreases rapidly over the course of several milliseconds. Oertel et al. (2011) have hypothesized that, given the phasic nature of auditory nerve input, a matched, phasic inhibition is needed in order to produce regular firing seen in sustained chopper responses. In agreement with this, Xie and Manis (2013) have shown that fast inhibition in stellate cells may selectively eliminate spikes immediately following the onset of a sound. D-stellate cells, given their fast and phasic response properties, might be an ideal inhibitory source to fulfill this function. Although this proposed function appears to be at odds with the finding that inhibition mainly affects the sustained portion of the response, the experiments which led to that conclusion were not able to distinguish between the effects of different inhibitory cell populations.

In both bushy and stellate cells, inhibition increases first spike latency (Paolini et al., 2004; Gai and Carney, 2008a). For stellate cells, the importance of first spike latency is not at all clear. For bushy cells, however, first spike latency contains information about sound intensity. The dynamic range optimization mechanisms discussed previously focused on controlling the cell's spike rate, but given the apparent importance of *absolute* timing in the output of bushy cells, it follows that managing dynamic range may involve adjustment of spike timing as well.

Forward masking is a psychophysical phenomenon in which sensitivity to a brief sound (probe) is reduced by the presence of an immediately preceding sound (masker). As the time difference between the masker and probe increases, the effect of forward masking is decreased. This effect is found in the responses of auditory nerve fibers as well as cochlear nucleus neurons. Typically, sensitivity to the probe is recovered within about 20 ms of the end of the masker (Boettcher et al., 1990; Backoff et al., 1997). Studies have shown that cochlear nucleus neurons have different amounts of masking and different recovery times between unit types, and that they are often different from auditory nerve responses as well (Boettcher et al., 1990; Shore, 1995). When inhibition is blocked either pharmacologically or by severing the descending connections from the SOC, recovery times often decrease significantly (Backoff et al., 1997;

Shore, 1998). This indicates that inhibition evoked by the masker continues to affect neuronal output even after the excitatory effects have diminished.

Forward masking caused by tuberculoventral inhibition has been proposed to serve as a mechanism for monaural echo suppression (Wickesberg and Oertel, 1990), although inhibitory input from both the SOC and from commisural D-stellate projections might facilitate binaural echo suppression as well. This is particularly important in the context of sound localization, where the presence of echoes would likely lead to reduced accuracy. Bushy cells, which form a crucial component in localization pathways, were found to have particularly long forward masking recovery (Shore, 1995).

1.7 Summary

It is clear that D-stellate and tuberculoventral cells provide major sources of inhibitory input to cells in the VCN. In some cases, connectivity between specific cell types has been clearly established. Both bushy and T-stellate cells are likely to receive tonotopically-precise input from tuberculoventral cells, as demonstrated by Wickesberg and Oertel (1990). In other cases, connectivity is strongly suggested through indirect means. Ferragamo et al. (1998b) demonstrated polysynaptic excitation and inhibition in T-stellate cells in slices of the VCN, suggesting input from both D-stellate and T-stellate cells. The remainder of VCN connectivity has only been inferred based on anatomical evidence and single-unit response properties. Thus, a major goal of the present research is to establish more direct evidence for the existence of connectivity between specific cell types.

Perhaps more importantly, there have been no *quantitative* measurements of connectivity on which to base computational models of the cochlear nucleus. A wide array of functions have been proposed for the local connectivity of the cochlear nucleus. Synthesizing a coherent theory that unites these functions will require both careful modeling and new types of experiments. Thus far, few of these proposed functions have been tested conclusively due to an inability to selectively manipulate individual circuit components. Photostimulation using caged compounds and optogenetic tools were developed to address this problem and have been used elsewhere with much success. These tools are relatively new and have not been applied to the cochlear nucleus before this research. The primary goal of the present research is to generate a quantitative description of connectivity and synaptic properties within the cochlear nucleus, with particular attention toward those factors most crucial for the development of computational models. In addition to spatial patterns of connectivity, we are interested in the strength and kinetics of synapses, and the relationship of these properties to both pre- and postsynaptic cell types.

Chapter 2

Experimental Methods

For many decades, researchers have used electrical stimulation or injection of neuroactive substances as a means to selectively activate specific components of neuronal systems. By recording post-synaptic currents in whole cell recordings, it is possible to measure the strength and kinetics of any activated synapses. Pre-synaptic cell populations are selected primarily through spatial segregation, so these techniques are most effective in studies examining long distance projections between nuclei. It has been more difficult to tease apart densely interconnected local networks. Electrical stimulation is thought to activate axons more strongly than cell bodies (Ranck, 1975; Histed et al., 2009), making it difficult to determine the identity of activated cells except when a homogeneous population of fibers can be isolated. For example, the wealth of information available about the dynamics of auditory nerve synapses exists largely because the nerve root can be electrically stimulated in brain slice preparations. Microinjection of glutamate provides a solution since this generally only stimulates cell bodies and dendrites. However, it lacks the temporal control provided by electrical stimulation and requires physical contact which can damage tissue, disrupt physiological recordings, and is generally tedious when stimulating many different locations.

Over the last twenty years, a variety of new tools have been developed with the intent of allowing more focal and selective manipulation of elements within neuronal networks. Laser photostimulation has received the most attention as it combines temporal precision with unparalleled spatial selectivity. By combining laser activation with computer-controlled beam steering, high resolution maps of connectivity may be acquired rapidly. Photostimulation of caged glutamate with continuous-wave lasers activates a narrow column of tissue in the path of the beam with a temporal resolution of a few milliseconds (Katz and Dalva, 1994). For greater spatial selectivity, caged compounds have been developed which are sensitive to 2-photon stimulation with ultrafast lasers (Fino et al., 2009). These techniques are analogous to traditional microinjection but provide superior temporal control and rapid throughput. Another popular technique uses genetically-encoded, photoactivatable ion channels such as channelrhodopsin and

halorhodopsin (Boyden et al., 2005; Han and Boyden, 2007). Since these channels are often expressed throughout the cell, including in the axon, optogenetic techniques are more analogous to electrical stimulation, but with the immense advantage of genetic selectivity combined with the strengths of laser photostimulation.

Few transgenic mice with differential expression across cochlear nucleus cell types have been demonstrated to date, making it difficult to definitively isolate input types based on genetic markers. However, the organization of interneurons in the cochlear nucleus is such that each of the three types is distinguishable by glutamate uncaging—D-stellate and tuberculoventral cells occupy different divisions of the nucleus, whereas T-stellate and D-stellate cells overlap but can be distinguished by their excitatory or inhibitory influence. Furthermore, the relative scarcity of excitatory interneurons within the AVCN mitigates the possibility of polysynaptic activation. Combined, these aspects make glutamate uncaging an attractive technique to use in the AVCN.

The strategy used in this study is, briefly, to make whole-cell recordings from individual AVCN neurons in cochlear nucleus slices, then photostimulate neurons systematically in a grid over the entire slice to determine the location and synaptic properties of neurons that connect project to the patched cell. Because the cochlear nucleus is a complex 3-dimensional structure, it would be difficult to determine the complete pattern of connectivity from a single slice plane. Therefore, three complementary slice orientations were chosen which preserve different aspects of the cochlear nucleus circuitry. By recording the exact location of each slice relative to the nucleus, maps have been registered to a 3-dimensional atlas. This was subsequently aligned to a tonotopic atlas of the mouse cochlear nucleus that was used to estimate the frequency sensitivity of both patched and presynaptic cells.

2.1 Dissection and Slicing

CBA/Caj mice (Jackson Lab) from in-house colonies, 13–33 days old (mean age 23±5 days, n=50), were used for all electrophysiological recordings. All experimental procedures were approved by the Institutional Animal Care and Use Committee at the University of North Carolina at Chapel Hill. Mice were anesthetized with ketamine (100 mg/kg) and xylazine (10 mg/kg) i.p., and then decapitated. The brain was removed and immersed in pre-warmed (34 °C) dissection buffer gassed with 95% O_2 and 5% CO_2 to a pH of 7.4. The dissection buffer was based on an N-methyl-D-glucamine (NMDG) solution proposed by Tanaka et al. (2008) to improve slice viability (Table 2.1). The solution we used differs in that it includes a set of metabolites commonly used in our lab, and lacks choline chloride because the high concentration of HCl used to balance the pH provided more than sufficient Cl^- concentration. A block of

Reagent concentration (mM)		
Reagent	Dissection	Recording
NaCl		122
KCl	1.75	1.75
NMDG	135	
KH2PO4	1.25	1.25
NaHCO3	25	25
Glucose	10	10
Myo-Inositol	3	3
Sodium Pyruvate	2	2
Ascorbic Acid	0.4	0.4
MgSO4 (7H2O)	1.5	1
CaCl2 (2H2O)	2	3
HCl	135	

Ion concentration (mM)		
Ion	Dissection	Recording
Na^+	25	147
K^+	3	3
Cl^-	140.75	129.75
Ca^{2+}	2	3
Mg^{2+}	1.5	1
PO_4	1.25	1.25
SO_4	1.5	1

Table 2.1: Artificial cerebrospinal fluid composition.

brainstem including the cochlear nucleus was dissected and attached with cyanoacrylate glue against agar on a platform mounted on a small gimbal. The cochlear nucleus was then cut on an oscillating tissue slicer (Leica VT 1200) to yield a single section, typically 350–600 µm thick.

Each cochlear nucleus was cut in one of three planes of section chosen to preserve or emphasize specific aspects of the nucleus circuitry (Figure 2.1; dissection solution). "Parasagittal" slices were cut in a nearly sagittal plane, with the dorsal end tilted about 20° medial to the sagittal plane. When cutting parasagittal slices, thin slices were shaved from the lateral surfaces of the DCN and VCN to remove the molecular and granule cell layers before cutting the final slice. Slices in this orientation were typically cut thicker (500–600 µm) to help preserve connections between the deep DCN and AVCN. "Ascending" slices were cut roughly parallel to the ascending branches of auditory nerve fibers (which run posteroventral at the nerve root to anterodorsal at the opposite end of the AVCN) and orthogonal to the lateral surface of the AVCN. In this slice plane, the anterior end was tilted about 40° dorsal to the horizontal plane. "Tuberculoventral" slices were cut orthogonal to the lateral surface of the AVCN and approximately parallel to the intranuclear fibers connecting the DCN and AVCN.

During slicing, the tissue block was viewed from the side through a low-magnification stereo microscope using a front-surface mirror turned 45°, and located beside the tissue block. The orientation of the mounting gimbal was adjusted before and during slicing to optimize the plane of section. The brain was photographed through the microscope before and after each cut to record the anatomical location of the extracted section relative to the brainstem block. These images were later used to reconstruct the slice in the context of a 3D atlas.

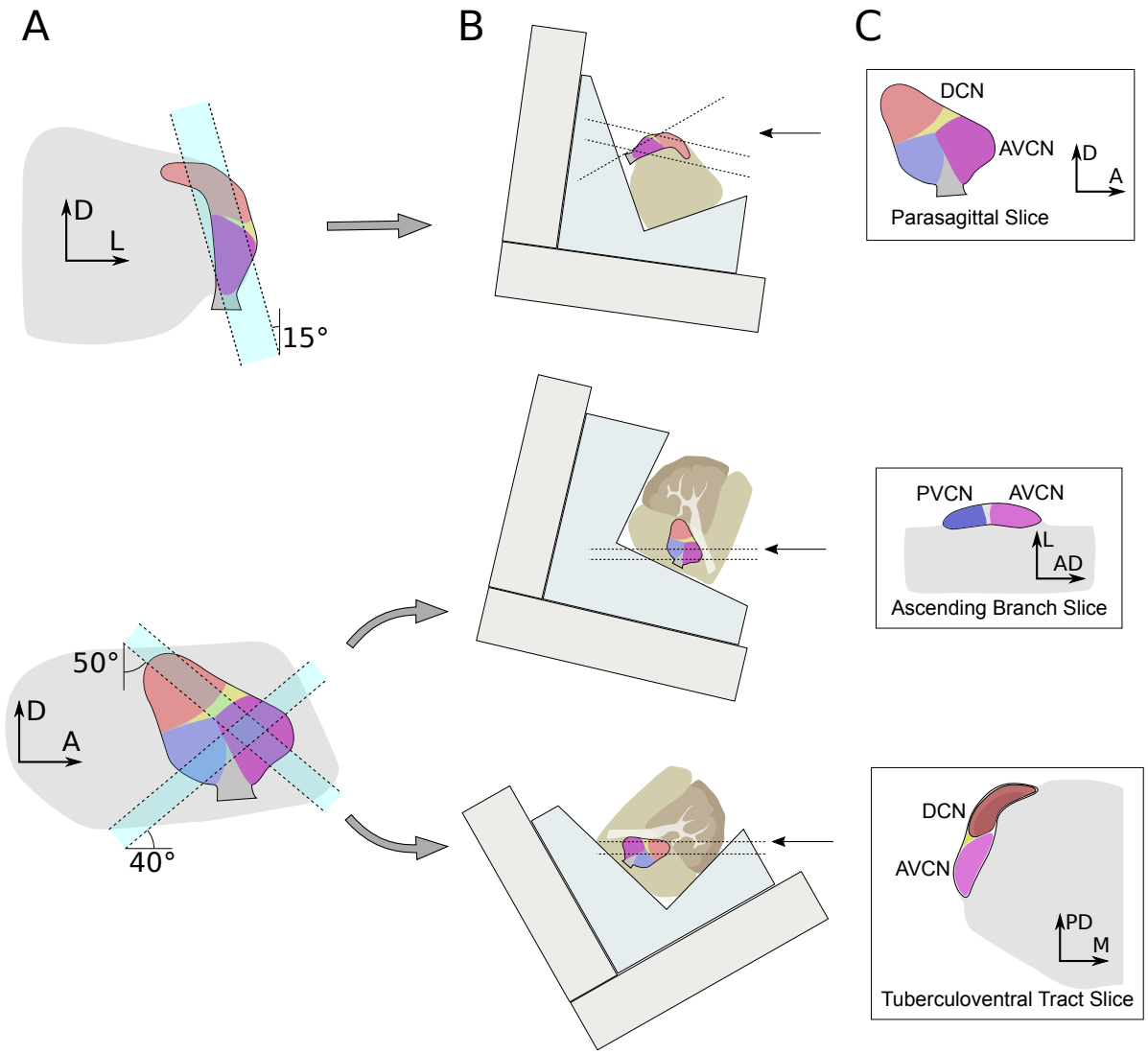

Figure 2.1: **A)** Schematics showing the orientation of cuts that produce the slice planes used in this study. Each slice plane was selected to retain specific sets of connections within the nucleus. **B)** Schematics showing positioning of gimbal, agar, and tissue block for each orientation. Note that parasagittal slices require the lateral surface to be shaved at two different orientations. Black arrows indicate the blade cittong direction. **C)** Schematics showing final shape of slices in each orientation.

2.2 Electrophysiology

Following dissection, slices were incubated for at least 30 minutes at room temperature in a NaCl-based artificial cerebrospinal fluid (ACSF) (Table 2.1; recording solution), and was bubbled with 95% O_2 and 5% CO_2 to a pH of 7.4. Slices were then secured in a recording chamber with a 7 ml recirculating supply of oxygenated ACSF containing 180 µM MNI-caged-L-glutamate and 360 µM S-MCPG, a nonselective metabotropic glutamate receptor antagonist (Tocris Bioscience). The solution was pumped through the recording chamber at approximately 2 ml/min using a peristaltic pump driven by a geared stepper motor to maintain a precisely-controlled flow rate. The flow was further smoothed using a 10 ml drip chamber to remove fluid pulsing generated by the pump. This was essential to achieving consistent photostimulation because changes in the fluid level and meniscus curvature can dramatically alter the focus of the laser beam. The stepper motor was separated from the peristaltic pump by a long drive shaft and powered by quadrature sine-wave outputs from an audio amplifier. This ensures that electrical noise is not transmitted from the motor into the fluid lines and is more acoustically quiet as well.

The ACSF was heated to 25 °C immediately before entering the recording chamber using an inline heater (Warner Instruments). This temperature was chosen because we found that increasing the temperature resulted in decreased synaptic release probability. Cells were visualized with an upright Zeiss Axioskop FS 2 equipped with a water-immersion objective lens (40x or 63x) and CCD camera (Photometrics Quantix 57 or QuantEM 512SC).

Patch electrode pipettes were pulled from 1.2 mm diameter borosilicate glass (Sutter) with a Sutter P2000 puller (Sutter Instruments), and had a resistance of ~3–10 MΩ in the bath. For most recordings, a cesium-based electrode solution containing QX314 (Tocris Cookson) was used to minimize potassium and sodium conductances and to improve voltage clamp of dendrites. This solution also allowed the cell to be depolarized by voltage clamp for prolonged periods. The electrode solution is described in Table 2.2 (cesium solution), and was adjusted to pH 7.3 with CsOH. This solution is based on a cesium solution used previously (Wang and Manis, 2005), but uses a lower Cl^- concentration to set the chloride reversal potential closer to physiological levels. Electrode solutions also contained Alexa Fluor 488 or 568 (Invitrogen) to allow morphological identification. Whole-cell recordings were made with a Multiclamp 700A amplifier (Molecular Devices). Recordings with whole-cell series resistance greater than 30MΩ were excluded from quantitative analysis of postsynaptic currents.

AVCN neurons are commonly characterized by their response to brief current injections; however, the use of Cs^+-based electrode solution makes this analysis problematic. In a subset of experiments, electrodes were first filled with a small quantity of a standard K-gluconate-based internal solution, followed by a

Reagent concentration (mM)		
Reagent	K-gluconate	Cesium
NaCl	2	
KCl	6	
K-gluconate	126	
CsMeSO3		128
CsCl		5
Sucrose	10	10
HEPES	10	10
EGTA	0.2	5
PhosphoCreatine bg	10	10
MgATP	4	4
GTP Tris	0.3	0.3
QX314 Cl		3
KOH	6	
CsOH		2

Ion concentration (mV)		
Ion	K-gluconate	Cesium
Na^+	2	
K^+	138	
Cl^-	8	8
Mg^{2+}	4	4
Cs^+		135

Table 2.2: Electrode solution composition.

larger volume of Cs^+ solution. This allowed cells to be physiologically characterized immediately after rupturing the cell membrane, as it typically took ~15 minutes for sufficient Cs^+ to diffuse to the tip of the pipette. The K-gluconate solution contained (in mM): 126 K-gluconate, 2 NaCl, 6 KCl, 10 sucrose, 10 HEPES, 0.2 EGTA, 4 Mg-ATP, 10 creatine phosphate, and 0.3 GTP Tris. The pH was adjusted to 7.2 with KOH and the final osmolarity was ~295 mOsm.

For voltage-clamp, cells were held at -50 mV (the estimated Cs^+-electrode solution junction potential of −11.4 mV was not corrected) when measuring excitatory synaptic responses or 0 mV when measuring inhibitory synaptic responses. Cells were monitored for the duration of each experiment to ensure that series resistance and input resistance were within acceptable limits. Typically the current required to hold cells at the target voltage were less than 50 pA at -50 mV or 200pA at 0 mV.

2.3 Photostimulation

To measure connectivity and characterize synaptic responses, we used caged MNI-glutamate photostimulation to evoke action potentials in cells presynaptic to the patched cell while recording post-synaptic responses. Photostimulation was done with a 100 mW, 355 nm UV laser (DPSS Lasers Inc. Series 3500) steered through the microscope's epi-flourescence port. The beam position was controlled with a pair of galvanometer-based scanning mirrors (6510H, Cambridge Technologies) combined with 100mm scan and tube lenses (Thorlabs) embedded within the microscope (see Appendix A). Laser power was monitored with a photodiode in later experiments. UV light pulses were controlled via the laser's Q-switch combined with a fast shutter (Uniblitz, Vincent Associates). The laser spot was approximately 90

μm in diameter with an intensity of ~20 mW at the sample, calibrated with a Newport 1917-R laser power meter and 818P-015-17W thermopile sensor (Newport).

Photostimulation pulses, physiological recordings, and galvanometer mirror commands were synchronized using a multifunction data acquisition device (National Instruments PCI-6259) controlled by custom software (www.acq4.org) written in Python. The galvanometer mirror voltage commands were determined by calibrating the resulting laser spot position against the CCD camera frames. Scanning maps were designed by visually specifying the desired spot locations relative to the image of the slice on the computer monitor.

2.4 Cell Characterization and Mapping Procedure

One of the primary goals of this study was to examine the relationship between cellular physiology and morphology, and patterns of synaptic connectivity. Thus cells were tested with a variety of experimental protocols to allow thorough characterization.

Patched cells were directly photostimulated in cell-attached mode before rupturing the cell membrane. The latency and number of action potentials elicited was used both to characterize the cell as well as determine optimal stimulation parameters to ensure that the majority of cells would respond with at least one action potential. Five cells underwent more extensive profiling to determine the relationship between pulse energy, spot location relative to the soma, and the response of the cell. After rupturing the cell membrane, the cell's current-voltage relationship was measured with standard current injection and voltage step protocols.

We mapped the locations of synaptic inputs to the cell by photostimulating sites in a hexagonal grid, typically consisting of 100–300 points, over the visible surface of the cochlear nucleus. Each site was stimulated while holding the patched cell at either -50 mV to record excitatory postsynaptic currents (EPSCs), or between -10 and +10 mV to record inhibitory postsynaptic currents (IPSCs). Photostimulation flashes of 10 to 40 µJ were generated by pulsing the laser Q-switch for 0.5–2ms. In experiments where the laser power was monitored, the flash duration was automatically adjusted to control the total energy delivered. For each stimulation, we recorded the membrane current for at least 300 ms before and after the laser flash. Stimuli were typically separated by about 1.5 s. Sites were stimulated in an optimized order to maximize the distance between subsequent stimulations, and adjacent sites were never stimulated within 10 seconds of one another. To reduce false positives, each site was usually stimulated 3 times per holding potential (for a total of 6 stimulations), however this number was occasionally varied depending on the cell's rate of spontaneous postsynaptic events. The response to each stimulation was recorded, along with the location of the stimulation site and an image of the laser spot to allow later verification of the laser calibration.

Chapter 3

Analytic Methods

3.1 Event detection

To compare mapping data across animals, all cell and stimulation locations were registered to a standard 3D atlas based on MRI images of the mouse brain with a resolution of 21.5 µm (Johnson et al., 2010). In this atlas, the cochlear nucleus and sub-nuclei were identified and labeled manually. Photographs taken during the slicing procedure were scaled and aligned with an image of the atlas to define the location of the slice. Next, a schematic image of the slice anatomy was generated by digitally slicing the atlas data to match the orientation of the physical slice, and the photos of the slice taken in the recording chamber were aligned with the atlas image. Finally, the location of the cell was marked manually and the location of laser stimulation sites were automatically registered with the slice photographs. The atlas was later aligned with a cochleotopic atlas (Muniak et al., 2013) to determine the arrangement of isofrequency sheets and tonotopic axis within the slice, and to estimate the likely frequency location of each patched cell or stimulation site. The width of the laser spot (90 µm) spans roughly 0.3 octaves within the tonotopic atlas.

The currents recorded during photostimulation represent 3 classes of events: spontaneous synaptic currents, evoked synaptic responses, and direct currents evoked by glutamate release onto the postsynaptic cell. One of the major challenges of photostimulation mapping is to separate these components and analyze them independently. Our approach is summarized in Figure 3.1. Whole-cell recordings are first filtered to remove 60 Hz line noise and high-frequency noise sources. Next, we search for large inward currents beginning less than 4 ms following the stimulus onset. Such currents are often the result of direct glutamate stimulation of the postsynaptic cell. If present, this current was fit against a shape comprised of the product of an exponential rise and the sum of two exponential decays:

$$y(x) = (1 - e^{-t/\tau_r})^p (Ae^{-t/\tau_{d1}} + Be^{-t/\tau_{d2}}) \tag{3.1}$$

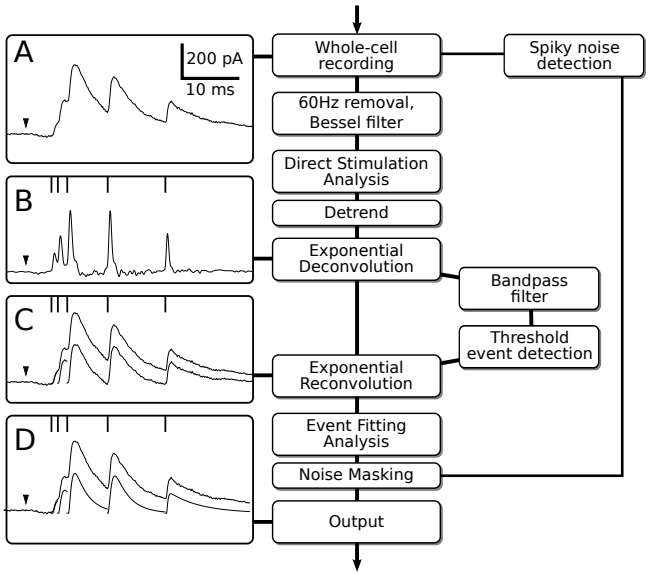

Figure 3.1: Event detection algorithm. The algorithm is described more thoroughly in the text. **A)** Whole-cell recording data is filtered to remove noise and detrended. In some cases, currents due to direct stimulation are subtracted from the traces. **B)** Next, the trace is exponentially deconvolved to emphasize the rising phase of each synaptic event. The deconvolved trace is used to determine the starting time of each event. **C)** Segments of the deconvolved signal are reconvolved to yield an estimated shape for each event as if it were isolated from prior events. **D)** The reconvolved event traces are fit to a function (Equation 3.2) to measure the onset time, amplitude, and time constants.

Traces were fit using the Levenberg-Marquardt algorithm in scipy (www.scipy.org; see scipy.optimize.leastsq), combined with a simple parameter-space search to reduce the probability of improper fitting. The results of this fitting procedure were saved for further analysis. In some cases, the fit depolarization shape was subtracted from the recording to improve our ability to measure synaptic events occurring during the falling phase of the direct response.

Recordings were next detrended and exponentially deconvolved (Richardson and Silberberg, 2008) to improve separation of overlapping events and emphasize the fast rising phase of synaptic events. The deconvolved signal was used to determine the onset time of each synaptic event and then partitioned into a single trace segment per event. The segmented events were then exponentially reconvolved to give an estimate of the shape of the event in the absence of any preceding events. Finally, the reconvolved events were fit to a synaptic conductance-like function that is the product of rising and falling exponentials:

$$y(x) = A(1 - e^{-x/\tau_r})^2 e^{-x/\tau_d} \tag{3.2}$$

For events that occurred in rapid succession, this method provides a good estimate of the onset time and amplitude of each event, but distorts their rise/decay kinetics. For well-isolated events, the exponential deconvolution and reconvolution have little effect and thus the rise/decay kinetics of the

event can be accurately measured.

3.2 Input detection

In photostimulation mapping experiments, both the presence of spontaneous events and the probabilistic nature of synaptic transmission introduce uncertainty about the presence of synaptic connections. Spontaneous events occurring shortly after the photostimulation may lead to false positive identification of inputs, whereas failures in synaptic transmission may lead to false negatives. Typical rates of spontaneous IPSCs were 0.1–2 Hz for bushy cells and 0.5–6 Hz for stellate cells, whereas spontaneous EPSCs occurred at 10–20Hz for both cell types. To reduce both types of error, we typically stimulated each site 3 times, depending on the spontaneous activity in the postsynaptic cell and the reliability of evoked responses. We also used high-Ca^{2+} ACSF to increase synaptic release probability, which should reduce the presence of false negatives.

Most photostimulation mapping studies identify evoked events by comparing the total charge transfer during equal periods before and after stimulation (e.g. Shepherd et al. (2003); Jin et al. (2006); Barbour and Callaway (2008)). We have found this method to be sensitive to noise and insensitive to photostimulation responses which evoke little charge transfer relative to spontaneous activity. In addition, charge transfer from synaptic events is obscured by direct stimulation currents for inputs close to the postsynaptic cell. To address these problems, we developed a statistical metric based on the onset times of detected events to distinguish spontaneous from evoked events. The method assumes that the times of occurrence of spontaneous postsynaptic currents (PSCs) follow the statistics of a Poisson process, and computes the probability that this process generates a particular series of events. This method is similar to one proposed by Chase and Young (2007) for measuring first spike latencies of neurons in response to sensory stimuli and in the presence of spontaneous activity.

The statistic is computed in 3 steps. First, we determined the mean rate of spontaneous events by counting the number of events in the pre-stimulus region of each recording (this region does, on rare occasions, contain events evoked by the preceding stimulation as well). For cells with a low spontaneous event rate (< 0.3 Hz), the rate was determined by averaging over all recordings for the cell. For cells with higher or erratic spontaneous rates, we measured the rate for each stimulus and applied a Gaussian smoothing filter ($\sigma \approx 30$ s) over time to generate a per-recording estimate of spontaneous rate.

Second, for each stimulation site we combined the times of post-stimulus events across all stimulus repetitions into a single pool. The spontaneous rates measured during the pre-stimulus period were also summed. We then computed a metric that indicates whether the pooled event times were likely to have

been generated by a Poisson process with the summed spontaneous rate. To compute the metric, let the function *N(t)* be the number of events occurring at time $\leq t$, relative to the stimulation onset. Then, for any time t post-stimulus, we can compute the probability that a Poisson process would generate *N(t)* events in a time window of width t using the survival function for a Poisson distribution with spontaneous rate s:

$$PoisSF(t) = 1 - e^{-st} \sum_{i=0}^{N(t)-1} \frac{(st)^i}{i!} \tag{3.3}$$

Third, the probability that the response in the evoked window is not due to spontaneous activity is computed by taking the minimum of the survival function between $t = t_{min}$ (2 ms) to $t = t_{max}$ (200 ms). Since taking the minimum involves multiple comparisons, a correction is needed to compute a probability from this metric. The correction is determined by measuring the scores for many repeated trials of a simulated Poisson process over a range of values for st_{max} and computing from this a table of p values.

This metric has an important advantage over simply computing the survival function at a specific time point in that it is sensitive to the *timing* of events as well as their rate. Events that cluster immediately after the stimulation time will yield a higher score. Thus the metric is sensitive even in situations with high spontaneous rates of activity as long as the presynaptic cell responds quickly and with reliable latency after the stimulation. At the same time, the metric can detect synaptic inputs that have longer latency or poor precision, but nevertheless increase the mean event rate over a longer time period.

For each map, the set of sites with evoked responses was determined by selecting those sites whose metric was less than some threshold (usually 0.001–0.01). The threshold was determined for each map based on the rate of spontaneous events and strength of evoked events. In a small number of cases, unstable membrane currents or sudden changes in the spontaneous event rate that were clearly not associated with the stimulus resulted in the incorrect detection of events; these were manually removed from the results.

3.3 Classification of cell types

Classification of cell type was difficult in these experiments because we primarily used cesium-based electrodes and thus could not rely on current clamp data. Cell identification was further complicated by incomplete dye labeling and in some cases by ambiguous morphology. To classify as many cells as possible, we used several complementary criteria. Cells were classified as bushy (55 cells), stellate (24 cells), or ambiguous/unusual (10 cells) on the basis of morphology, spontaneous PSC kinetics, and when available, I/V curves. Morphological classification was made by ranking the cells on a scale from 1 to 5 (1=bushy, 3=ambiguous, 5=stellate) and averaging results from three independent experienced observers.

Average values less than or equal to 2 were considered bushy; values greater than or equal to 4 were considered stellate. Additionally, spontaneous PSC kinetics could be used in most cells to distinguish between categories by measuring the ratio between the decay time constant of excitatory and inhibitory PSCs (Xie and Manis, 2013). Cells with a ratio greater than 0.5 were considered stellate whereas cells with a ratio less than 0.2 were considered bushy. In a subset of cells, I/V curves were measured with potassium gluconate electrode solution. These cells could be classified by their responses to short current injection pulses (Oertel and Wu, 1984). For cells patched with cesium electrode solution, a similar (but less reliable) classification could be made based on the response of the cell to direct stimulation while recording in cell-attached mode. Cells for which direct stimulation elicited a train of action potentials were almost always stellate cells, whereas cells that responded with a single action potential could be either type.

Cells expressing entirely bushy-like or stellate-like characteristics were classified accordingly. Although it is clear that bushy and stellate cells represent two distinct populations of cells, many of the differences between these populations are expressed on a continuum (Webster and Trune, 1982; Rothman and Manis, 2003a; Typlt et al., 2012); some cells express properties that appear to be intermediate between the two populations, whereas other cells have characteristics of both populations. Despite this difficulty, it is still beneficial to classify cells based on the canonical bushy and stellate categories. In addition, cells having unclear characteristics were classified as "ambiguous" and those expressing characteristics of both cell types were classified as "unusual".

Stellate cells were further classified as either T-stellate or D-stellate based on morphology and membrane properties. T-stellate cells typically have dendrites constrained to a narrow isofrequency region, whereas D-stellate cells have dendrites that cross frequency planes (Doucet and Ryugo, 2006). Cell reconstructions were overlaid onto the maps of isofrequency contours generated using the cochleotopic atlas from Muniak et al. (2013), and cells whose dendrites clearly were oriented to cross the isofrequency contours were flagged as candidate D-stellates. We often had poor confidence in this morphological characterization because of incomplete fills, and thus combined it with measurements of I_h current kinetics (Fujino and Oertel, 2001), which could be measured in voltage clamp with Cs^+-containing electrodes. We measured the activation time constant of the I_h current in response to a voltage step from -50 mV to -130 mV. Cells with decay constants less than 20 ms *and* D-stellate morphology were considered likely D-stellate cells (2 cells). The remainder were simply labeled "stellate" and likely are primarily T-stellate cells (22 cells).

3.4 Statistical Analysis

Many of the samples we compared for differences were not normally distributed, so significant differences were detected using a custom permutation resampling function. First, the difference between the means of two samples was computed. Next, values were randomly shuffled between the samples while keeping the sample sizes constant, and the differences in the means of each permuted sample pair was computed. Finally, the p-value was determined as the fraction of times the absolute value of the permuted mean differences exceeded the originally measured difference. For each comparison we performed 10,000 permutations. Where this function determined a p-value of 0, we have reported that $p<10^{-4}$. The scipy.stats library for Python was used to compute single-sample t-tests (stats.ttest_1samp) and Pearson correlation coefficient (stats.pearsonr). Multiple groups were compared by ANOVA using R and are described in the Results. Data are presented as mean$\pm$standard deviation throughout Chapter 5.

Chapter 4

Description of Software

Both the experimental and analytical methods used in this work are highly technical and would be impossible without the use of specialized software. This chapter describes the design and function of the various software components that were developed to support this project.

4.1 Objective and rationale

We have developed a modular software platform for experimental neurophysiology called ACQ4. The system integrates acquisition, management, and analysis of all experimental data collected for this project. With a few exceptions, it was designed as a general-purpose tool and thus we expect it to be of value to the neuroscience community and potentially other fields of research. It is available for download at

http://www.acq4.org.

Within the context of this research, the purpose of developing ACQ4 was to provide a system that could carry out photostimulation mapping, imaging, and general electrophysiology protocols as described in Chapter 2 as well as the analyses described in Chapter 3. At the time we began developing ACQ4, few software options were available with photostimulation mapping capabilities. We evaluated some of these and found additional development would be required to meet the needs of this project. For reasons discussed below, our preferred development platform is Python, but no acquisition systems were available on this platform. Furthermore, no software existed with the data analysis capabilities we needed. These reasons led us to create an entirely novel acquisition and analysis system based on Python. Knowing this would be a significant undertaking, we also designed ACQ4 to satisfy general-purpose experimental requirements in the hope it would prove useful outside the context of this research project (and indeed, has already been used in a variety of other projects).

The broad scope of ACQ4 is to provide a generic system for accessing data acquisition and control hardware including cameras, motorized position control, and generic DAQ devices. ACQ4 is a modular, extensible system, making it possible to add support for new types of devices and experimental protocols.

The tools currently included with ACQ4 provide support for a wide range of neurophysiology techniques including patch-clamp electrophysiology, photostimulation mapping, calcium imaging, intrinsic imaging, and two-photon imaging.

4.2 Platform

ACQ4 is written in Python, a modern, open-source programming language that has grown rapidly to become one of the most popular general-purpose programming languages in use. While the commercial system MATLAB is currently the dominant programming environment for scientific use, Python use is growing quickly and offers many benefits over MATLAB. Whereas MATLAB was designed specifically for numerical computation, Python is a modern, general-purpose programming language and thus we have found it to be a more capable language overall, particularly in the ease with which it interacts with device drivers, user interfaces, and the operating system. Python is also free, open-source, and unencumbered by commercial licensing, which greatly reduces barriers for other researchers to access ACQ4. Python also benefits from the *scipy* and *numpy* projects, which bring excellent numerical and scientific computing to Python. Finally, Python has bindings to several mature, feature-rich user interface libraries. We have chosen the Qt library for its excellent, high-performance graphics capabilities.

Another popular language for scientific computing is C++ because, although it is considerably more difficult to use, it provides better computational performance than interpreted languages such as Python and MATLAB. We have found, however, that by leveraging the numpy library to perform most computationally demanding functions as well as Qt to perform most graphically demanding functions, we are able to achieve comparable performance in most cases.

The combination of these components—Python, numpy, and Qt—allows ACQ4 to operate efficiently on most platforms using entirely free software. ACQ4 currently operates on Windows, Linux, and OSX. In practice, the availability of hardware drivers may restrict the platforms available for data acquisition. For example, the cameras currently supported only ship with Windows drivers and MultiClamp amplifiers do not support Linux. Displaying and analyzing data, however, works on any platform supporting Python, Qt, and numpy. Optional Python libraries are required for access to various features: h5py is required for reading most data files stored by ACQ4, the Python Imaging Library (PIL) is required for access to TIFF files, and pyparsing and pyserial are required for data acquisition. ACQ4 has been tested on Windows XP, Windows 8, Mac OSX, and Ubuntu Linux. National Instruments DAQmx 9.x is required for access to NI DAQ functionality.

4.3 Program details

4.3.1 Overview

ACQ4 is developed as a general-purpose research platform with a strong focus on neurophysiology. In our lab it is currently used for patch-clamp electrophysiology, photostimulation mapping, multiphoton microscopy, calcium imaging, and cortical intrinsic imaging. The software handles most aspects of acquiring, managing, and analyzing experimental data. Its acquisition capabilities include scanning laser imaging, camera imaging, and I/O via NI DAQ hardware including support for a variety of patch-clamp amplifiers.

ACQ4 is both a platform for application development and a suite of modules built on that platform. At the core of ACQ4 is a central manager which controls access to devices, executes protocols synchronizing multiple devices, manages storage and retrieval of data, and loads user interface modules (Figure 4.1). Each user interface module provides a specific functionality such as camera access, synchronized recording and device control, data browsing, and various analysis modules. These modules make use of the services provided by the manager, allowing them to communicate and synchronize with one another.

Data acquisition may be achieved either by submitting task requests to the Manager or by directly accessing the hardware. In most cases, modules will submit task requests to the Manager that describe the intended actions for each device included in the task. The manager handles all aspects of device configuration and synchronization, while ensuring that tasks submitted by different modules do not attempt to access the same hardware simultaneously. This is one of the most important services provided by the Manager because it simplifies the creation of new modules and at the same time encourages scalability. For situations that require lower-level access to the hardware, modules may request direct access from the Manager.

Most data in ACQ4 is stored using the HDF5 file format. These files contain both the raw data arrays from camera and DAQ recordings as well as meta-information related to the recordings. ACQ4 provides libraries for reading these files in both Python and MATLAB. Experimental data is organized into directory hierarchies while annotations and log files are stored within data directories in a human-readable format. The organization of this hierarchy is in part specified by the experimenter and allows flexibility when designing and executing experiments. When this data is analyzed, the results are typically stored in an SQLite relational database file. The use of industry-standard HDF5 and SQLite formats helps to ensure that data will be readable by a variety of different applications.

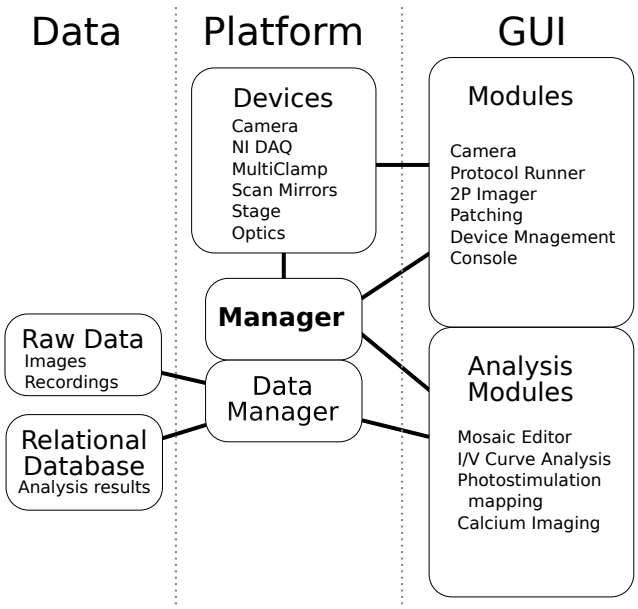

Figure 4.1: Schematic representation of the architecture of ACQ4.

4.3.2 Supported hardware

ACQ4 supports a large family of data acquisition devices via the National Instruments DAQmx library. These boards are used to communicate with most of the hardware used in ACQ4 including patch clamp amplifiers, scan mirrors, CCD cameras (for triggering and timing readout), shutters, and Pockel cells. Currently we have tested E and M-series boards. ACQ4 currently supports Photometrics and QImaging cameras for both realtime video display and capture as well as in synchronized data acquisition. ACQ4 has full support for controlling both MultiClamp 700A/B and AxoPatch200 amplifiers, although nearly any amplifier should be usable if it only requires DAQ communication. We use ACQ4 with galvometric scan mirrors from Cambridge Tech and Thorlabs for both multiphoton imaging and photostimulation. Input to the mirrors is automatically calibrated using a CCD camera, allowing photostimulation and imaging coordinates to be specified graphically over a camera image. Lasers are controlled via DAQ TTL and analog outputs, providing automated access to shutter, Pockel cell, and Q-switch controls. Optionally, laser power output may be monitored and calibrated to provide known power levels or light pulses of a specific energy. We also support basic control functionality for Coherent Chameleon lasers. ACQ4 uses position information from Sutter MP-285 stage controllers and other rotary encoders to allow later reconstruction of large image mosaics as well as photostimulation mapping data. Position-awareness is deeply integrated into ACQ4's user interface such that all imaging and photostimulation is represented in physical coordinates.

Most devices in ACQ4 will provide a control panel for immediate access to the device as well as an

interface for designing experimental protocols (see ProtocolRunner). ACQ4's modular architecture allows adding support for new devices through several plug-in interfaces. Most devices, however, need little more than access to DAQ lines to operate sufficiently.

Generic optomechanical devices

The experiments that ACQ4 is designed to handle often involve data with complex spatial relationships. For example, one may wish to collect photos from a broad range of locations across a sample, perform physiology at some of these locations, or direct a scanning laser to a specific place relative to the sample. Throughout ACQ4, a global coordinate system is used to represent the natural coordinates of the sample, and all recording or stimulation that takes place with a defined spatial relationship to the sample is automatically registered with the global coordinate system. Thus, images and photostimulation data are automatically stored alongside their global position and scale, allowing automatic mosaic reconstruction. A broad subclass of devices, referred to as *optomechanical* devices, represent hierarchically-linked devices with a defined physical or optical relationship to one another. For example, a motorized stage, microscope, and camera may all be linked optomechanical devices. As the stage and sample move, the global coordinate location of the microscope and camera will shift to reflect this new arrangement. Likewise, changing the objective lens currently in use will change the optical scaling and offset associated with the microscope, which in turn defines the boundaries of the camera sensor relative to the sample. The end result is that all devices and the data they produce are spatially aware, and this requires no effort from the user during the experiment.

Cameras

Support for scientific cameras currently includes all devices which use either PVCam (Photometrics) or QCam (Q-Imaging) drivers. Cameras support both live-imaging modes as well as more controlled data acquisition modes that specify the timing and behavior of the device. In live-imaging mode, the camera usually collects frames freely and sends them to a camera module (see Section 4.3.3) for display. Cameras also manage their own connections to DAQ channels. During managed protocols, the camera may be triggered by the DAQ or serve as the starting trigger for an device. Additionally, many cameras export a TTL signal that indicates the timing of frame exposures. In protocols that record this signal, it is analyzed to determine exposure time of each camera frame. Image data is then stored to disk alongside the time values of each frame relative to the start of the protocol, as well as the raw exposure and trigger signals. The result is that physiological recordings made synchronously with imaging can be automatically registered temporally during analysis.

Cameras are optomechanical devices (see Generic optomechanical devices above), and thus may be calibrated such that their size, position, and orientation have a fixed spatial relationship to any other optomechanical devices. This is most commonly used with both a motorized stage for position feedback and a microscope device which defines per-objective scaling and offset. With a properly configured system, image mosaics can be collected and automatically reconstructed.

Data acquisition boards

ACQ4 supports a large family of data acquisition devices via the National Instruments DAQmx library. These are commonly the central hub of data acquisition and device control. They are responsible for recording analog signals from physiology equipment, synchronizing cameras, driving galvometric scan mirrors, and communicating with a variety of other hardware such as LEDs, shutters, pockel cells, photodiodes, Q-switched lasers, etc.

In ACQ4, the user rarely interacts directly with the DAQ system. Instead, each device that is connected to channels on the DAQ will handle this automatically. The user specifies actions, waveforms, and recording criteria by interacting directly with each device. The benefit to this approach is that each device is free to define the user interface that is most naturally suited to that particular device. For example, scanning mirrors make use of one analog output per mirror. The user will only rarely need to specify the exact voltage signal needed at the analog output ports; instead, the user specifies the spatial pattern desired for the laser spot, and the scanner device takes care of communication with the DAQ.

Electrophysiology amplifiers

Three amplifiers are currently supported for electrophysiology experiments: the MultiClamp 700, the AxoPatch 200, and the AxoProbe 1A. ACQ4 records all remotely accessible parameters from the MultiClamp Commander software (Molecular Devices) or from the telegraph outputs on the AxoPatch 200. Scaling constants for input and output to the DAQ channels are automatically applied, and for MultiClamp, several parameters may be controlled from the user interface such as the VC/CC mode, gain, and signal selection. Switching between voltage and current clamp is handled automatically by the device, first switching to I=0 mode before changing the holding commands sent to the DAQ. This allows ACQ4 to rapidly and safely switch between recording modes without user interaction.

Scan mirrors

Galvometric scan mirrors are commonly used as laser positioning devices for both multiphoton imaging and photostimulation. ACQ4 supports these devices by exporting two calibrated analog output

signals via a DAQ board. For experiments combining laser scanning and physiological recording, it is recommended to have at least three analog output channels available. Mirror positions are determined by the user by specifying the desired location of the laser beam relative to the global coordinate system. Since scanners are optomechanical devices (see Generic optomechanical devices above), they are aware of both their position relative to the sample and the details of any optics in between. Thus, ACQ4 scanners perform a basic coordinate mapping: given an x,y location in the global coordinate system, determine the voltages V_x,V_y that will cause a specific laser (multiple lasers may share the same set of mirrors) to be centered on the global location specified. This mapping is determined by an automated calibration system that uses a camera to record the laser spot location while scanning over a range of mirror voltages. From this data, the coefficients of a generic mapping equation are solved:

$$\begin{aligned} V_x &= Ax^2 + By^2 + Cx + Dy + E \\ V_y &= Fx^2 + Gy^2 + Hx + Iy + J \end{aligned} \tag{4.1}$$

The mapping coefficients are determined once for each combination of source laser and microscope objective. Scanner devices support three modes of operation during protocols. For simple photostimulation experiments, the output voltage is set immediately before each protocol run. This mode does not require buffered access to the analog output channels. Fore more complex scanning patterns such as with mutltiple sequential photostimulation sites or arbitrary scanning imaging patterns, a simple command language can be used to specify raster, line scan, circular, and spiral scan shapes. This mode is sufficient for even the most complex photostimulation and imaging experiments. For any use not supported by the simple command language, arrays of x,y locations may be specified instead.

Lasers

ACQ4 supports calibrated laser output using Pockel cells, shutters, and Q-switched lasers. Laser devices report their current output power either using a beamsplitter and calibrated photodiode, or by power reporting built in to Coherent laser systems. The laser device then determines, based on the objective lens currently in use, the expected power at the sample. The user may specify either the desired continuous laser power for long scanning protocols or the desired laser pulse energy for fast photostimulation protocols. These values for power or energy are then used to determine the correct pockel cell output voltage or the duration of a Q-switched pulse, respectively. This allows more predictable laser delivery over long-term experiments where it is expected that the output power of the laser may drift over time, or optical components may change. Furthermore, it allows the user to specify experimental protocols using physically meaningful units.

Stages

Due to the spatial awareness that is built in to many aspects of ACQ4, it is recommended to use a stage or movable microscope objective with some sort of position feedback. ACQ4 has support for the Sutter MP285 controller (with the use of custom interfacing hardware; see Appendix B) which is frequently used in motorized stage systems. Stages are represented in ACQ4 as optomechanical devices whose offset is determined by the position reported by the stage feedback. In the hierarchy of optomechanical devices, stages are typically the highest-level parent device. Thus, stage motion is immediately propagated to all devices which are optomechanically linked to the stage. This allows imaging data to be recorded alongside the location of the image, which facilitates the automated reconstruction of image mosaics. The Camera user interface module (Section 4.3.3) has several features which make use of this optomechanical transformation information.

4.3.3 User interface modules

ACQ4's user interface is divided into modules, each providing support for a specific type of activity. Modules are one of the primary ways that ACQ4 may be extended to perform new functionality.

Camera

The Camera module (Figure 4.2) provides a live video feed from one or more imaging devices and also serves as a visual representation of the global coordinate system for photostimulation and laser imaging controls. On systems with access to stage position information, the Camera module will track the current position and update the virtual coordinate space accordingly. This allows, for example, tracking the location of specific cells or sites in the preparation, acquiring large, multi-part photostimulation maps, and building large image mosaics which are displayed behind the camera feed. For systems with multiple microscope objectives, this feature provides a persistent view of the sample under low power, allowing the experimenter to navigate around the sample without switching objectives.

The Camera module also provides image processing features helpful for enhancing image contrast for cell patching and calcium imaging, as well as region of interest plotting from the live video feed. Multiple imaging devices may be used simultaneously and displayed with the correct relative scaling and alignment. The Camera module handles recording individual frames and video to disk.

The display area of the Camera module serves as a visual representation of the global coordinate space. It displays not only images generated by the camera, but also data and user interface controls generated by other modules. A module for laser scanning imaging, for example, displays a rectangle

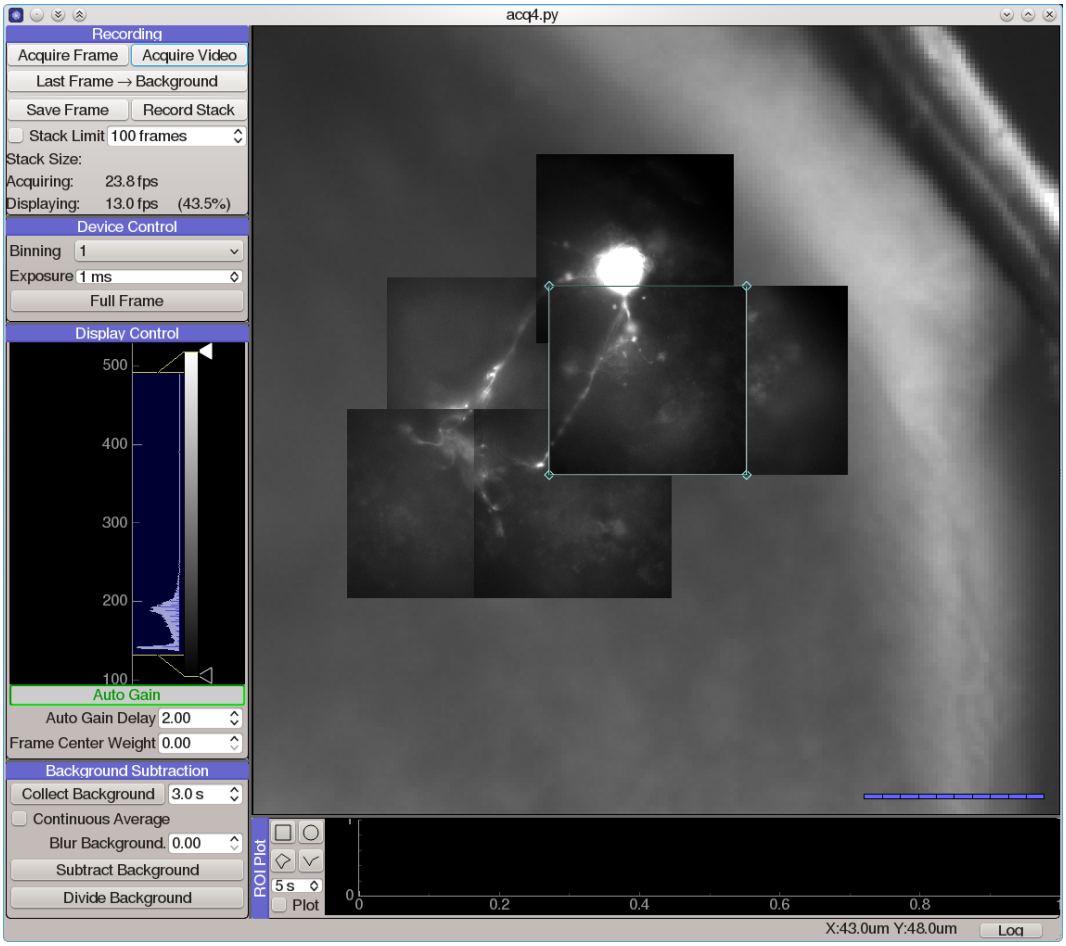

Figure 4.2: Screen capture of Camera module. The central panel shows a live video feed (frame outlined in white) of epifluorescence imaging of a filled cell. Other images were recorded previously and displayed in the background of the camera module. Since ACQ4 keeps track of both the position of the microscope stage and the currently used objective lens, these background images are automatically positioned and scaled relative to the video feed. The panels at the left side provide user control over the operation of the camera and video display modes.

which can be positioned by the user to determine the area imaged with a multiphoton laser system. Likewise, photostimulation sites, grids, and scanning paths are all displayed in the Camera module allowing photostimulation patterns to be defined in relation to either camera or multiphoton imagery. Online analysis modules may also use this space to display photostimulation mapping results or images generated in scanning imaging protocols.

Protocol Runner

The Protocol Runner is a customizable interface to ACQ4's protocol execution capabilities (Section 4.3.4). It allows the user to design and execute protocols combining any number of devices. The vast majority of data is collected with this module, which is used for everything from recording spontaneous activity to photostimulation mapping, LTP induction protocols, and complex stimulation paradigms. When designing a protocol, the user selects the subset of devices which should participate in the protocol. Each device provides its own graphical interface for specifying the behavior of the device during the protocol (e.g. recording modes, output waveforms, etc.) as well as for displaying data recorded by the device. Synchronization between devices is achieved by specifying the control and triggering waveforms used by each device, while the DAQ hardware ensures that protocols are executed correctly. Waveforms are specified either by combining predefined elements such as square pulses or by evaluating an arbitrary Python expression that generates the array.

In this context, the word "protocol" is used to describe a single, coordinated action to be taken by one or more devices. Typically a single protocol involves a short period of recording (usually less than 1 second) from patch clamp amplifiers, cameras, or other DAQ-connected devices such as photomultiplier tubes. Arbitrary waveforms may be defined to control stimulation devices, scanning mirrors, and triggering behavior. The Protocol Runner module also allows the execution of sequences of protocols which iterate over multi-dimensional parameter spaces. Typically, variable parameters affect some aspect of a stimulus waveform such as the starting time or amplitude of a pulse. However, each type of device defines the ways in which it can define variable parameters. Scanning mirror devices, for example, may define an arbitrary set of photostimulation locations, allowing the same protocol to be executed once for each location. If multiple sequencing variables are specified, the module executes the protocol once for each point in the multi-dimensional parameter space.

Data Manager

The Data Manager module allows the user to browse, view, and export recorded data; view experiment logs; and manage notes and other metadata. Additionally, this module is used to determine

the default storage location for data during the experiment. To streamline experiment execution, all modules record data into this default directory rather than prompting the user for a location.

For large studies, keeping data properly annotated and organized consistently is both essential and difficult. The Data Manager encourages hierarchical organization of data by allowing the user to construct trees of pre-defined directory types, each having its own set of metadata fields. For example, the experiments in this study followed a predictable pattern: on any given day, multiple slices were dissected from a single animal, and multiple cells were recorded from each slice. Thus, each experiment begins with one directory indicating the date, and annotated with information about the animal and other experimental conditions for that day. Next, a sub-directory is created for each slice used during the experiment, and each of these is annotated with information about the location and orientation of the slice. Images of the slice are stored in this directory. Finally, a sub-directory for each cell is created inside the appropriate slice directory, and these are annotated with information relevant to the cell such as its location, type, and depth within the slice. All data collected from this cell is stored within this directory. Importantly, the meta data fields for each type of directory are pre-defined (but user configurable), which encourages the user to collect and store data with a consistent organization. Since each type of experiment will have a different organizational design, the set of directories and their associated meta data fields is configurable by the user.

Other modules

Several other modules provide more focused features such as scanning laser imaging, assisted cell patching (Figure 4.3), cell health monitoring, direct device control, and an interactive Python prompt.

The Patch module sends a simple test pulse to the patch amplifier in order to test the current status of the electrode or cell. It is configured to rapidly update during patching and displays the input and access resistances measured by the electrode. After patching is complete, this module may be run more infrequently in the background to monitor cell health. Resistances, holding current, resting potential, and capacitance are all collected and stored as a record of the patching procedure and cell health throughout the duration of the experiment. These values may also be plotted to assist the experimenter in tracking changes over time.

The Imaging module provides laser scanning imaging functionality for multiphoton and confocal microscopes. This module combines control of scanning mirrors, laser power control, and signal detection devices (e.g. photomultiplier tubes or photodiodes). Like other modules, the Imaging module operates in the global coordinate system and displays its output in the display area of a Camera module. It also displays a user-positionable rectangle which defines the extents of the laser scanning area. The Imaging

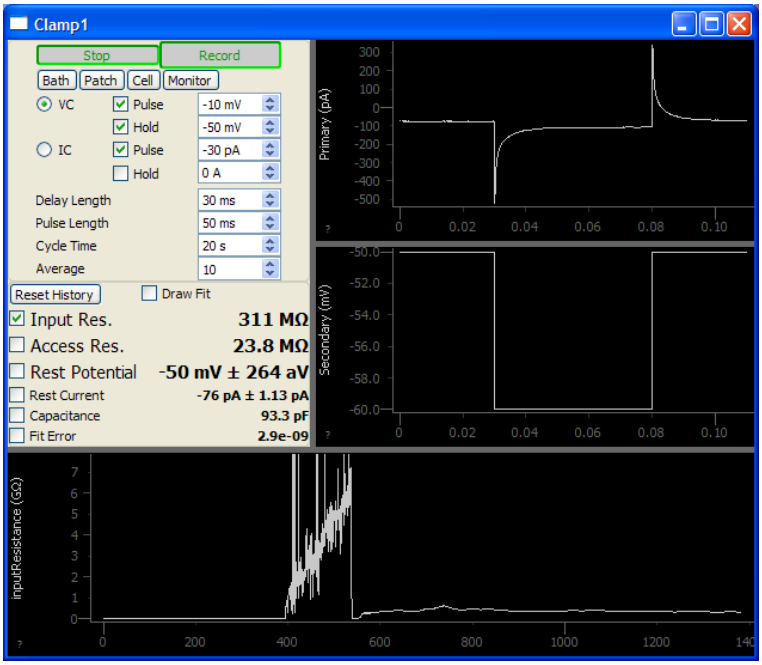

Figure 4.3: Screen capture of Patch module. At top-right is the current recording from a patched cell. The left panel is used to control the clamp mode and test pulse parameters, and displays a basic analysis of the recording. At bottom is a record of the input resistance over the entire time it was patched.

module supports overscanning to remove retrace artifacts as well as bidirectional scanning with automated field shifting to reduce comb artifacts.

4.3.4 Device management and protocol execution

The Manager keeps track of all devices in the system, and in most cases, handles all details of configuring and synchronizing devices to perform acquisition. User interface modules acquire data by submitting tasks to the manager, which runs each queued task in order as hardware becomes available. Each task consists of a list of the devices that should be used as well as a set of commands describing the desired behavior of each device. This may include stimulus waveforms, the names of channels to record from, triggering settings, and other options. Each device defines the exact set of options it will accept.

When the Manager receives a new task, it executes a series of steps to ensure that all devices are configured properly and started in the correct order. First, the Manager waits until all requested hardware has become available. Next, it iterates over all of the devices in the task, asking each whether it has a preference for being configured before any others. Devices are then configured in the requested order using the task options specified for each device. This stage typically involves sending stimulus and triggering waveforms to the DAQ hardware, preparing devices to receive triggers, and setting the proper recording mode on patch clamp hardware. During this stage, each device indicates whether it should be

started before or after any other device, based on the specified triggering options. This allows, for example, a camera to be triggered by a DAQ digital output in one task, or for the DAQ to be triggered by the same camera in another task. Finally, each device is started in the correct order.

At this point, control returns to the module that requested the task. When the task has completed, the module is sent a signal informing it that the results of the task are ready to be used. Most modules simply display the results or perform online analysis. If requested, the Manager will handle storing all task results to disk for later retrieval and analysis. The Manager handles tasks in a thread-safe manner, allowing modules to request and wait on tasks in a background thread while the main thread displays results and processes user input.

4.3.5 Analysis

Analysis is carried out through a series of modular components, each of which perform a specific analysis and record these results. Analysis modules can be combined to accomplish more complex tasks. Some can be reprogrammed graphically to alter their behavior. ACQ4 provides several analysis modules designed to handle the most common analysis tasks. For more localized problems, external Python modules may be loaded to perform custom analysis. ACQ4 also provides a data abstraction system which allows a variety of data formats to be read and interpreted by the same analysis hardware.

The Mosaic Editor provides a virtual canvas for displaying and aligning images and other data in physical coordinates. This module facilitates the creation of image mosaics which can be aligned with position-dependent data (such as photostimulation maps) and anatomical reference atlases. All data is annotated with this alignment configuration to allow further analysis to operate on normalized, corrected coordinates. An extensible atlas system provides a mechanism for creating positionable drawings and other user interface elements that allow the data to be registered with a standard coordinate system.

The Event Detector module detects and measures repeated events within a signal. This is used primarily for detecting action potentials, synaptic currents, and calcium imaging signals. The module can be configured to make a variety of measurements on each detected event such as the amplitude and decay time constant and outputs a table of this data to be written to database or passed on to another module. The core analysis performed by this module is entirely customizable—a visual programming environment (similar to LabView) allows a variety of filters and detectors to be configured which determine the module's output function. This environment allows analysis routines to be rapidly prototyped and tested. It may also embed Python scripts, allowing more flexible analysis.

The Photostim module embeds an Event Detector and analyzes a sequence of photostimulation recordings. The results of this analysis are used to construct colored maps and exported to database or

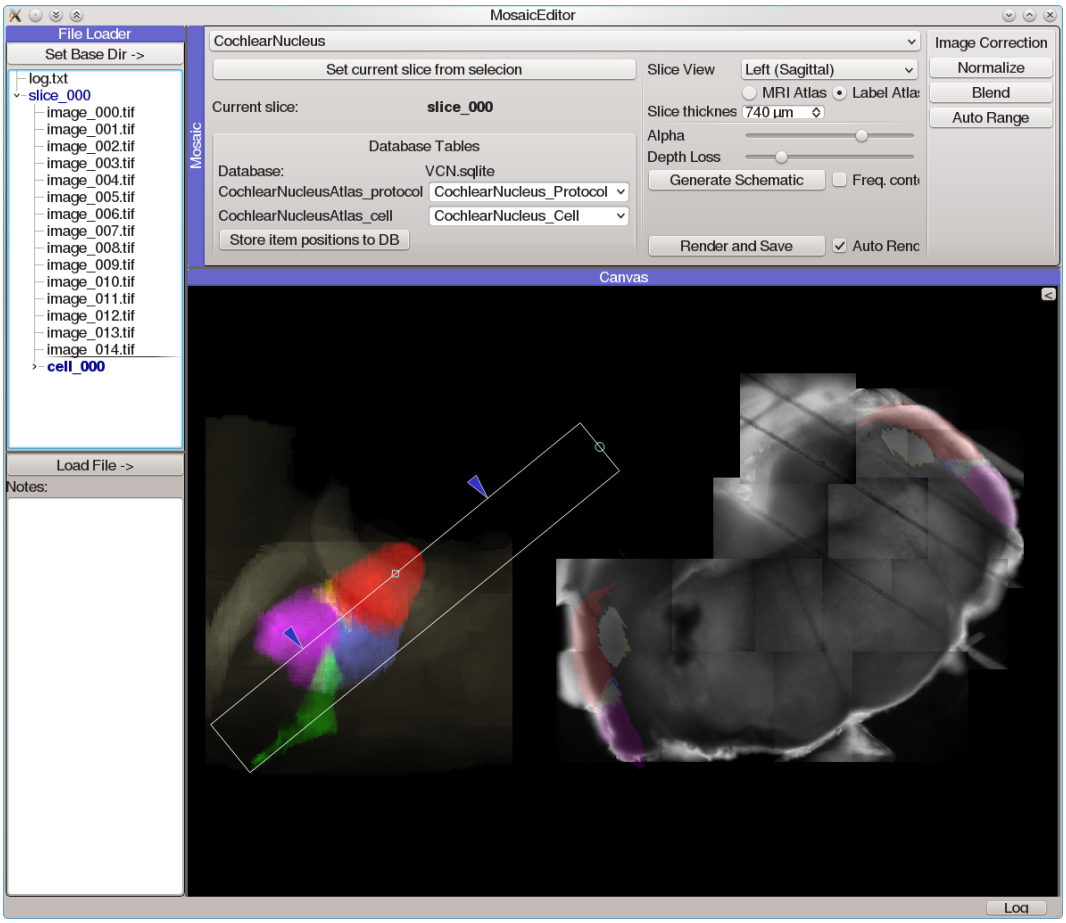

Figure 4.4: Screen capture of MosaicEditor analysis module. On the right, a mosaic of the brain slice has been automatically reconstructed from several individual images. Overlaid above the mosaic is a virtual slice of a labeled 3D atlas, as determined by the position and orientation of the slice plane indicated at the left.

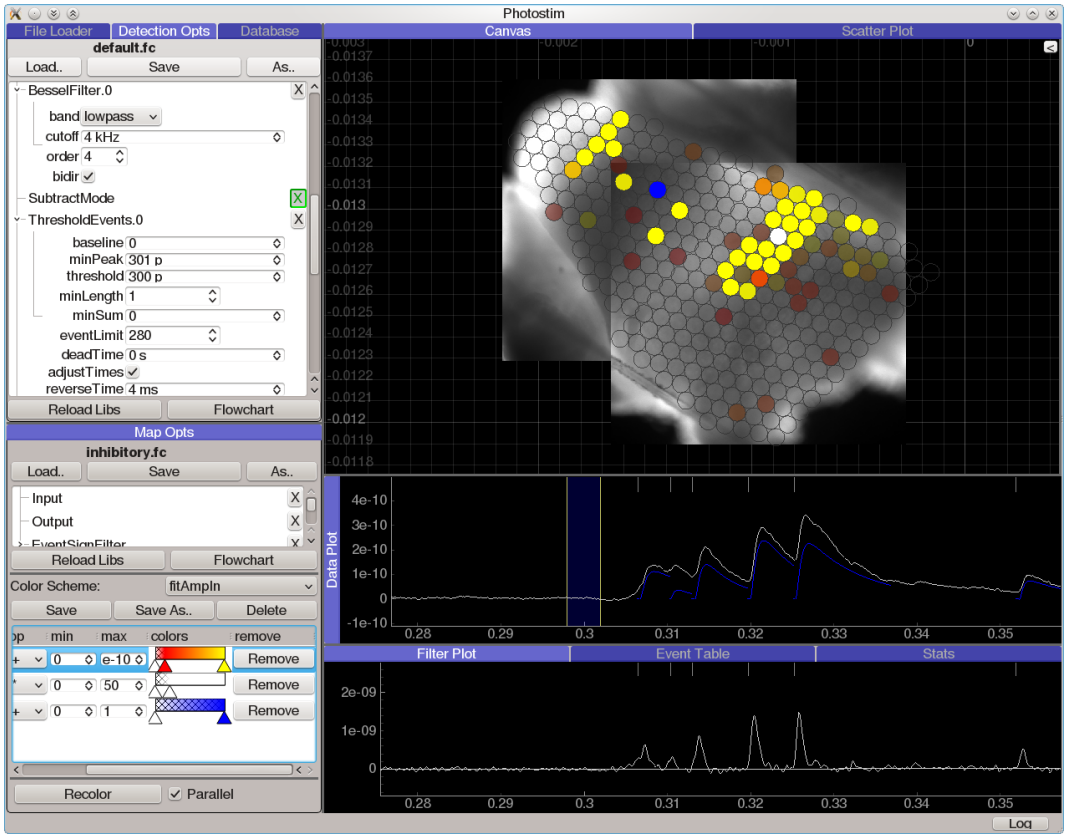

Figure 4.5: Screen capture of Photostim analysis module. The leftmost panel contains controls for determining event detection and map coloring criteria. At top-right is an automatically generated mosaic showing photos of the brain slice with two separate photostimulation maps overlaid. Beneath that, the panel labeled "Data Plot" shows raw recordings of evoked IPSCs (white) as well as the shapes of events as they were detected and fit (blue). Note that these event shapes are estimates of the *isolated* shape of each event, as it might look in the absence of any preceding events. At bottom-right is a panel showing the exponential deconvolution that is used to detect the onset time of each event (see Section 3.1).

other modules. The output of this module is further analyzed by a number of other modules which apply Poisson statistics as described in Chapter 3, spatial correlation algorithms (Bendels et al., 2010), or simply combine maps based on their atlas alignment.

Several other analysis modules have been developed such as the ImageAnalysis module, which provides basic tools for analyzing imaged fluorescent indicator data combined with physiological recordings. The IVCurve module performs basic analyses of current pulse protocols which are standard for characterizing patched cells. Each of these modules is designed to operate both as a standalone analysis application or as an embeddable module for participating in more complex analyses. This architecture encourages re-use, consistency, and scalability of analytic methods among the various modules

Chapter 5

Experimental Results

5.1 Cell classification and localization

The cells in this study fall almost entirely within the AVCN with only a few cells in the posteroventral cochlear nucleus (PVCN) or possibly past the dorsal margin of the AVCN (Figure 5.1A,B). Most cells fall within the central AVCN, with the ventral and rostral borders largely excluded. Stellate cells were confined to the lateral portion of the nucleus, with only bushy cells found in the medial extent. Cochlear nucleus slices were taken in three different orientations, indicated in Figures 5.1C, D, and E. No granule cells were included in this study.

Cells were classified as either bushy or stellate based on both morphology and PSC kinetics. Fifty-five of 89 cells were classified as bushy and 24/89 were classified as stellate. Bushy cells were defined as having IPSCs with decay time constant more than twice as long as their EPSC decay time constant (typically > 5 ms and < 1 ms, respectively), whereas stellate cells had nearly equal EPSC and IPSC decay time constants (typically about 3ms; Figure 5.2A,B), in agreement with Xie and Manis (2013), although the time constants in the present study are longer because recordings were done at a lower temperature (25 °C vs 34 °C). Five cells were classified as "ambiguous" because they lacked unambiguous morphological or PSC data. Another 5/89 cells were classified as "unusual" because they appeared to have morphological and physiological characteristics from both categories. Cells classified as ambiguous or unusual are excluded from this report, except where indicated.

The differences in decay time constants between bushy and stellate cells were statistically significant for both spontaneous EPSCs (bushy=0.50±0.11 ms; stellate=2.6±0.92 ms; permutation $p<10^{-4}$) and IPSCs (bushy=14±6.8 ms; stellate=3.6±0.86 ms; permutation $p<10^{-4}$). In addition to the decay time constant, we measured the amplitude and rate of spontaneous events. The rate of spontaneous IPSCs was significantly lower in bushy cells than stellate (bushy=0.46±0.59 Hz; stellate=3.1±2.9 Hz; permutation $p<10^{-4}$), whereas the rate of spontaneous EPSCs was not different (bushy=13±8.2 Hz; stellate=12±7.1 Hz; permutation

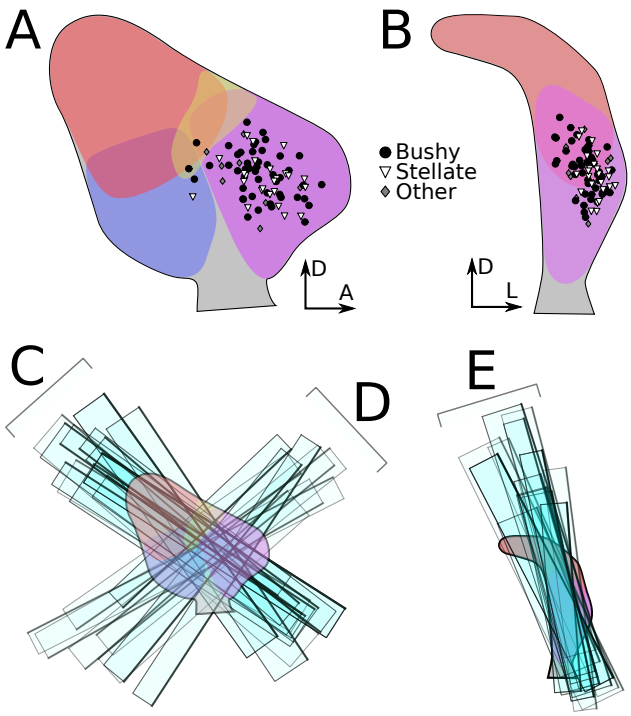

Figure 5.1: Locations of data sampled in this study. **A)** Sagittal view of the cochlear nucleus atlas with locations of patched cells indicated. **B)** Coronal view of the atlas with the same cell locations marked. **C)** Rectangles indicate the locations of a selection (approximately 1/3) of tuberculoventral slices aligned against the the atlas in sagittal view. Dark edges indicate the side of the slice that was visible during the experiment. **D)** Locations of ascending slices aligned against the atlas in sagittal view. **E)** Locations of parasagittal slices aligned against the atlas in coronal view.

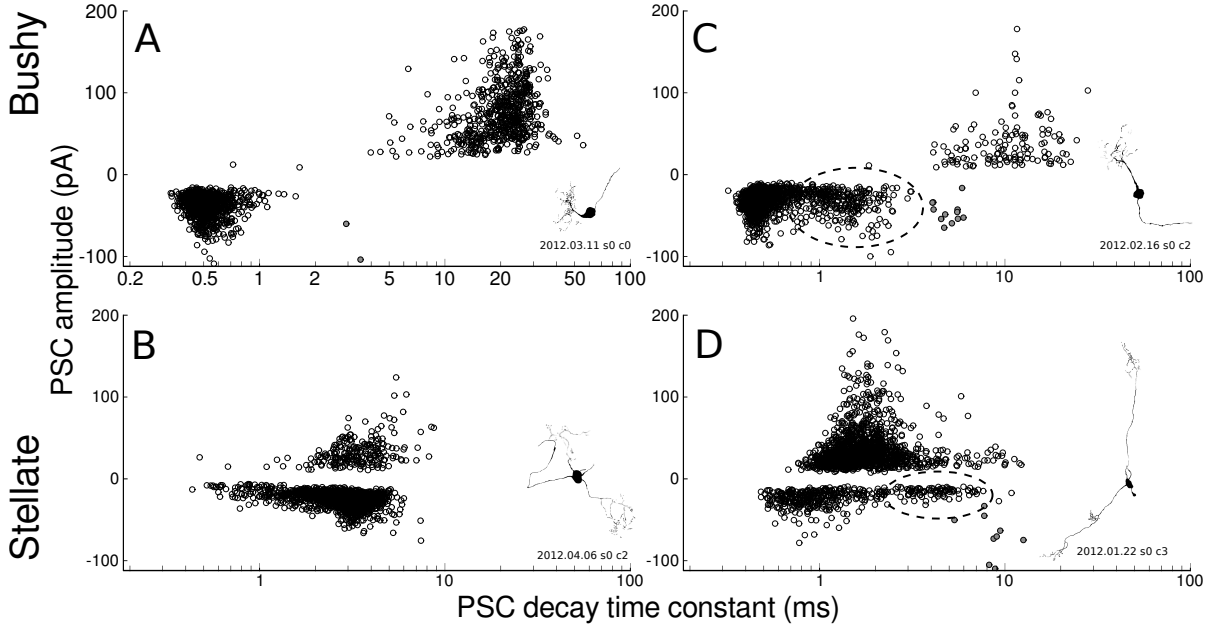

Figure 5.2: Spontaneous PSC kinetics depends on the postsynaptic cell type. Shown are scatter plots of PSC amplitude vs decay time-constant for both spontaneous and evoked events in four cells. In all cases, both spontaneous and evoked events form overlapping populations. **A)** Typical bushy cell with slow IPSCs (presumed to arise from tuberculoventral and D-stellate synapses) and fast EPSCs (presumed spontaneous release at auditory nerve synapses). **B)** Typical stellate cell with matched EPSC and IPSC decay kinetics. **C)** Bushy cell with bimodal EPSC distribution. The slower population of EPSCs (dashed ellipse) is presumed to be of non-cochlear origin. A third population (filled grey) consists of direct-stimulation depolarizations. **D)** Stellate cell with bimodal EPSC distribution.

p=0.73). Conversely, the amplitude of spontaneous IPSCs was not significantly different between cell types (bushy=20$\pm$12 pA; stellate=24$\pm$11 pA; permutation p=0.37) whereas the amplitude of spontaneous EPSCs was larger in bushy cells than stellate (bushy=-35$\pm$9.8 pA; stellate=-19$\pm$6.3 pA; permutation $p<10^{-4}$).

In addition to the fast EPSCs that result from spontaneous release at auditory nerve terminals, 10 cells also had a population of slower EPSCs. Slow EPSCs were detected in 7 bushy cells, with decay time constants between 1.5 and 3ms (Figure 5.2C). If such events are present in stellate cells, they would be difficult to distinguish due to overlap with the decay times of auditory nerve EPSCs. However, 3 stellate cells had a subset of EPSCs with decay time constant clearly different from those of their auditory nerve EPSCs (2.5, 11, and 25 ms) (Figure 5.2D). Bimodal EPSC distributions have not been reported previously in VCN neurons and were only apparent in this study due to the long recording times required to carry out photostimulation mapping.

5.2 Responses to Direct Stimulation

Glutamate uncaging does not excite all cells in the same way. Therefore, it is necessary to measure the responses of potential presynaptic cells to photostimulation. Specifically, it is important to know the firing patterns of photostimulated cells and how these this patterns change as the laser spot is positioned over different regions of the cell. To accomplish this, 59 cells in this study were photostimulated at least once with the patch electrode attached to the exterior of the cell. This provides a sample of the responses that are likely to be generated with photostimulation, although the sample is biased in that it excludes cells that are deeper or in different regions of the slice. The laser pulse duration was adjusted such that most cells fired at least one spike in response to photostimulation. This duration was typically about 1 ms, providing a total pulse energy of 20 µJ at the sample. The direct responses of the principal cells of the VCN depended on the cell type. Stellate cells most frequently (12/18) responded with a train of spikes, which could last for tens or hundreds of milliseconds (Figure 5.3A). In contrast, most bushy cells (31/33) responded with a single spike when photostimulated, regardless of the laser pulse duration (Figure 5.3B). These responses are consistent with the known responses to current injection for bushy and stellate cells (Oertel, 1983). Five cells were photostimulated repeatedly at densely-spaced (~30 µm) locations to determine the relationship between the number of evoked spikes and distance from the laser spot to the soma (Figure 5.3C). These results show that the spatial resolution of presynaptic targets in the photostimulation maps is likely not consistent. However, the maximal distance from the center of the laser spot to a target cell body is 150 µm, and for 4 out of 5 cells was less than 100 µm.

After photostimulation maps were measured in the cell-attached mode, the amplitude and kinetics of direct photostimulation responses were evaluated in whole-cell recordings. In most cases, direct stimulation resulted in currents of several hundred pA lasting for tens of ms (eg, Figure 5.3D, trace c). In 31 of the 85 cells tested, a portion of the response current persisted for hundreds of ms, suggesting the presence of slower glutamate receptors in the cell membrane. The amplitude of this slow component varied widely depending on the exact location of the laser flash over the cell (Figure 5.3D), indicating that glutamate receptors are not uniformly distributed on bushy and stellate cells.

For each cell, we counted the number of sites on a 90 µm grid with direct responses greater than 20 pA. The plot in Figure 5.3E shows these counts separated by cell type. Consistent with the differences in dendritic morphology between bushy and stellate cells, we found that stellate cells typically had direct stimulation currents in about twice as many sites as bushy cells.

In addition to the relationship between the position of the laser illumination and the evoked cellular response, it is also useful to know how the depth of the cell within the slice affects the probability of

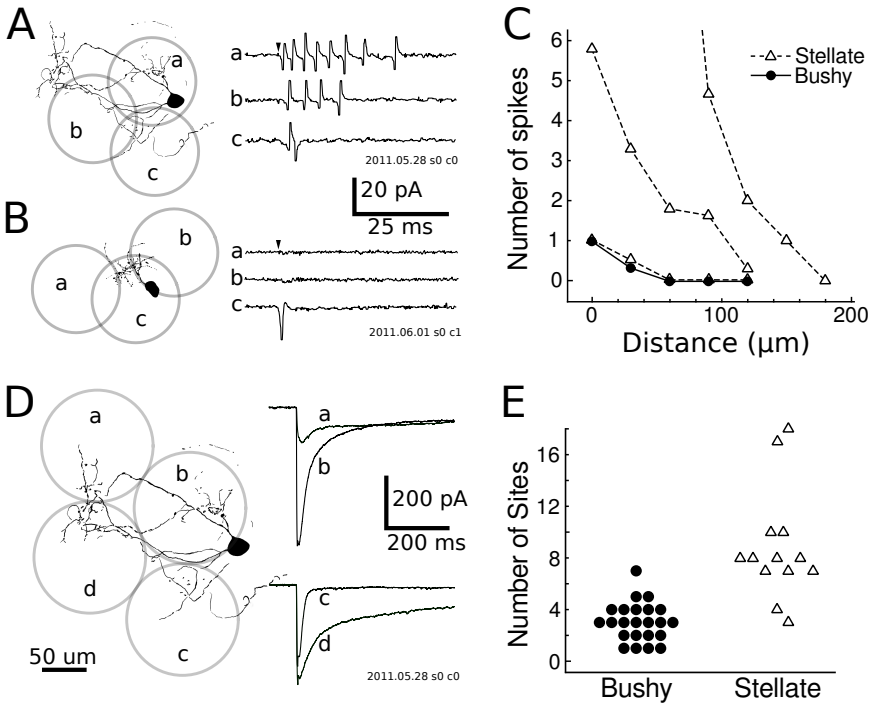

Figure 5.3: Typical responses to direct photostimulation. **A)** Example cell-attached, voltage-clamp recordings taken with photostimulation at three locations over a stellate cell. **B)** Similar cell-attached recording on a bushy cell. **C)** Profiles of one bushy and three stellate cells showing the the number of spikes fired versus the distance from the cell soma to the center of the laser spot. **D)** Example intracellular voltage-clamp recordings taken at four sites over the same stellate cell. **E)** Stellate cells have significantly larger direct response areas than bushy cells. Each point represents, for a single cell, the number of stimulation sites in a grid that produced a direct response peak larger than -20 pA.

evoking a response. In principle this relationship is difficult to measure, so we addressed this indirectly by estimating the scattering and divergence of the beam as it travels through the tissue. The details of this experiment and its analysis are described in Appendix C. From these estimates, it appears that the intensity of the laser is decreased by 80% at a depth of 200 µm, thus we expect that the majority of cells stimulated are at shallower depths. Although this estimate is quite coarse, it does help us to constrain the problem somewhat—neurons are unlikely to be strongly activated through the entire depth of the slice, and beam scattering within the tissue should not adversely affect the mapping resolution.

5.3 Spatial organization of input sites

Photostimulation maps of inputs to individual cells for both excitatory and inhibitory synaptic currents were analyzed to determine the locations of presynaptic cells in the map. We found that both bushy and stellate cell receive inhibitory input from regions in both VCN and DCN, and occasionally from the dorsal border of the AVCN. Excitatory inputs were much rarer, and tended to arise from locations close to the recorded cell. In the following sections, we discuss each source region separately.

For each cell, photostimulation responses were recorded, analyzed to detect synaptic events, and ultimately mapped to a 3-dimensional location inside an atlas of the cochlear nucleus. The example in Figure 5.4 describes the format we use to represent this data. Photostimulation responses typically consisted of a combination of three features: spontaneous PSCs, evoked PSCs, and direct photostimulation currents. Direct currents can be distinguished from evoked currents by their short latency of less than 1 ms from the laser flash (Figure 5.4G), whereas evoked synaptic events typically had a latency greater than 3 ms (Figure 5.4E,F). Photostimulation sites with evoked events are distinguished from those with purely spontaneous events on the basis of the Poisson statistic described in Section 3.2.

Inhibitory input from VCN

Eighty-nine percent (59/66) of cells had detectable inhibitory inputs that arose from within the VCN, usually appearing as a contiguous cluster of sites surrounding the postsynaptic soma (Figure 5.5). The vast majority of these inputs were in the AVCN with only a few from PVCN, which is unsurprising because the postsynaptic cells were almost exclusively in the AVCN. The area over which detectable inputs were evoked was highly variable, ranging from zero to over half of the AVCN. Some cells appeared to receive inputs that were aligned within frequency bands (e.g. Figure 5.5A,E) whereas others appear to receive inputs that were arranged across the isofrequency planes (e.g. Figure 5.5D). The two D-stellate cells in our dataset both had inhibitory input from nearby in the AVCN, indicating the presence of local

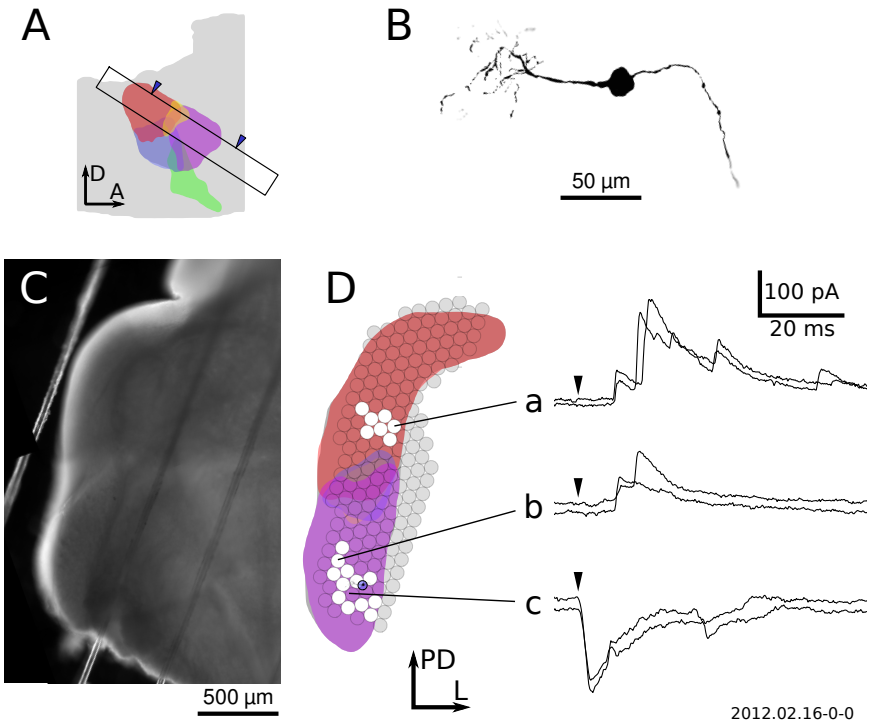

Figure 5.4: Example mapping data for a single bushy cell. **A)** Schematic indicating the location of the slice from which this cell was patched. This slice was taken from the right hemisphere of the brain. Arrowheads indicate the surface of the slice that was visible during the experiment. Colors are red=DCN, blue=PVCN, purple=AVCN, green=auditory nerve, yellow=granule cell area. Note that the divisions between anatomical regions may not be orthogonal to the plane of section, thus the regions have some overlap in the schematic. **B)** When available, maps are accompanied by a morphological reconstruction of the cell based on two-photon microscopy or fluorescence images. **C)** Image of the slice (reconstructed mosaic) as seen under the 4x microscope objective. **D)** Map of input locations overlaid on schematic of the slice, which was automatically generated from a 3D atlas. Each circle indicates the location of multiple (typically 3) laser stimulations; white filled circles indicate a presynaptic input was detected in the patch recording. The size of each circle indicates the illumination area of the laser spot. The location of the postsynaptic cell is shown by a blue circle over the AVCN. **D-a,b)** Voltage clamp recordings of IPSCs evoked in DCN and AVCN, respectively. Black arrowheads indicate the time of photostimulation. **D-c)** Direct photostimulation of the patched cell.

inhibition, likely from other D-stellate cells.

Stellate and bushy cells process and emphasize different aspects of their auditory input. Hence, we hypothesized that they would differ in the spatial organization of their inhibitory inputs. Indeed, stellate cells in this sample typically had twice as many VCN stimulation sites with detectable inhibitory input as bushy cells (Figure 5.6A; bushy=7.7$\pm$5.4; stellate=21$\pm$13; permutation $p<10^{-4}$). Since the difference is quite large, we next investigated which aspects of the input maps differed between cell types. T-stellate cells have dendritic arbors that extend in a planar configuration within isofrequency planes. In contrast, bushy cells have small, dense dendritic arbors with few synapses. We hypothesized that T-stellate cells would receive input from D-stellate cells within the same frequency range as bushy cells, but that the input would arise from a wider area parallel to the corresponding isofrequency sheet. To our surprise, we found exactly the opposite.

For each cell, we measured the standard deviation of the location of its inputs along the axis roughly parallel to both the isofrequency sheets and the lateral surface of the nucleus (Figure 5.6B). In this measure, we found no difference between bushy and stellate cells (bushy=149$\pm$54 µm; stellate=176$\pm$69 µm; permutation p=0.22). This result was unexpected and suggests that T-stellate cells may preferentially receive VCN inhibitory input to their proximal dendrites. This is consistent with anatomical evidence that synapses are comparatively sparse at the distal dendrites of T-stellate cells (Smith and Rhode, 1989). Similarly, we found no difference between cell types along the isofrequency axis orthogonal to the lateral surface of the nucleus (not shown; bushy=69$\pm$35 µm; stellate=97$\pm$16 µm; permutation p=0.08)). Measuring input convergence orthogonal to the isofrequency surfaces is more difficult due to the curvature of these surfaces. To determine whether bushy and stellate cells have differing input convergence across isofrequency lamina, we estimated the center frequency of each stimulus site (CF_{site}) using the cochleotopic atlas constructed by Muniak et al. (2013). For each cell, we measured the standard deviation of input site frequencies, scaled logarithmically, such that the range is expressed in octaves: $range = stdev[log_2(CF_{site})]$. A comparison of the input frequency range per cell is shown in Figure 5.6C. On average bushy cells received inputs over a frequency range corresponding to ±0.3 octaves around the cell's estimated frequency, whereas stellate cells received inputs that spanned ±0.5 octaves (but note that this is not a measurement of the *maximum* extent of the input area). This difference was statistically significant (bushy=0.31$\pm$0.15 octaves; stellate=0.49$\pm$0.18 octaves; permutation p=0.0035). Figure 5.6D summarizes the average input site distributions for bushy and stellate cells, after referencing the input site frequency to the target cell's frequency. This further supports the observation that stellate cells receive local inhibition from within the AVCN that spans a wider frequency range than do bushy cells. Note that the input widths reported only reflect the tonotopic span associated with the locations of presynaptic

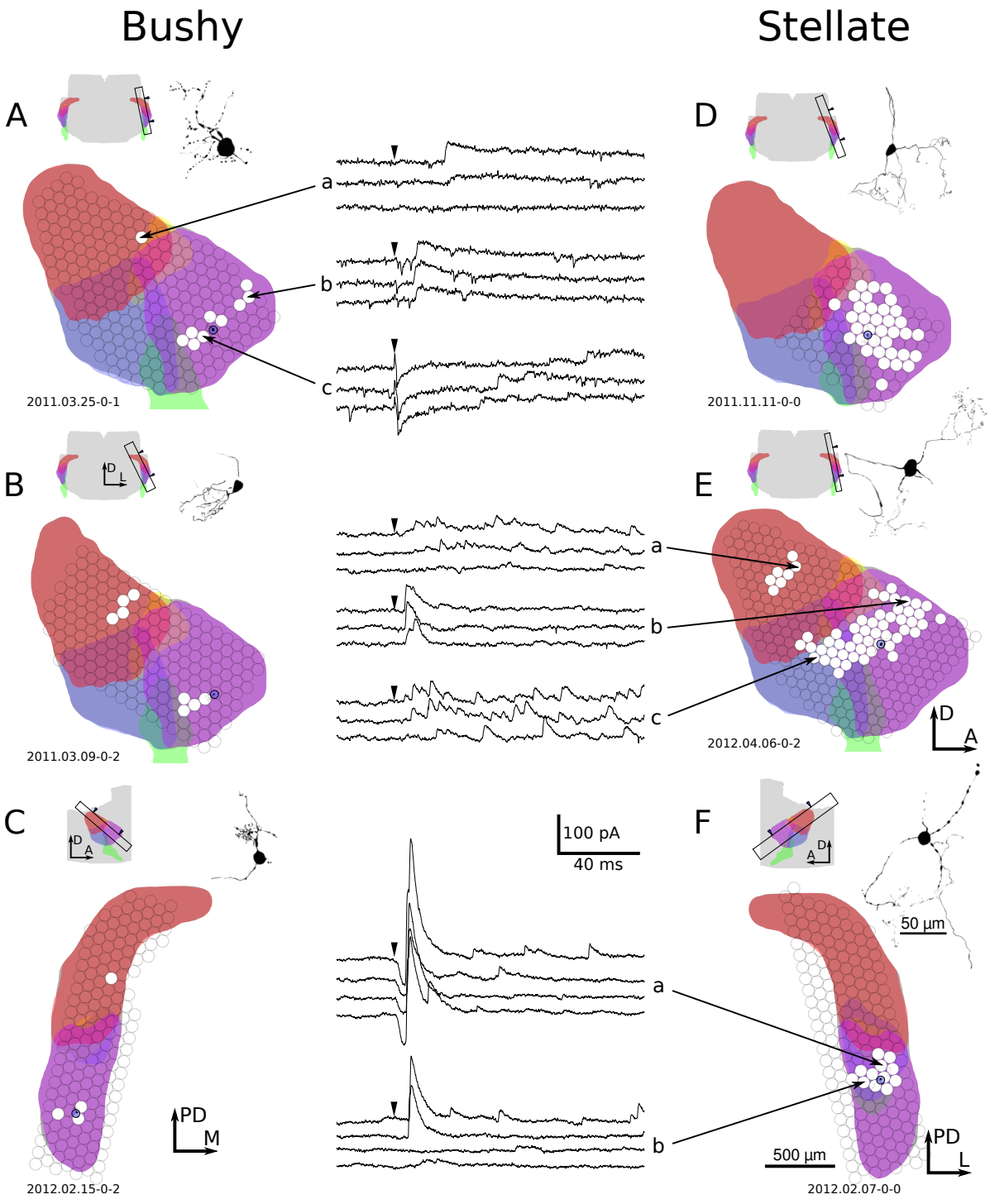

Figure 5.5: Example inhibitory connectivity maps for six AVCN cells. The format is described in Figure 5.4. Each cell has input from the AVCN; four also have input from the DCN. **A,B)** Bushy cells in parasagittal slice plane. **C)** Bushy cell in tuberculoventral slice plane. **D,E)** Stellate cells in parasagittal slice plane. **F)** Stellate cell in tuberculoventral slice plane. The example voltage-clamp recordings in this figure show a wide variety of response types, including weak (A, E), strong (F), rapid firing (E-a, E-c), single event (A-b, F-a, F-b), late (A-c), unreliable (A-a, F-b), and direct (A-c, F-a).

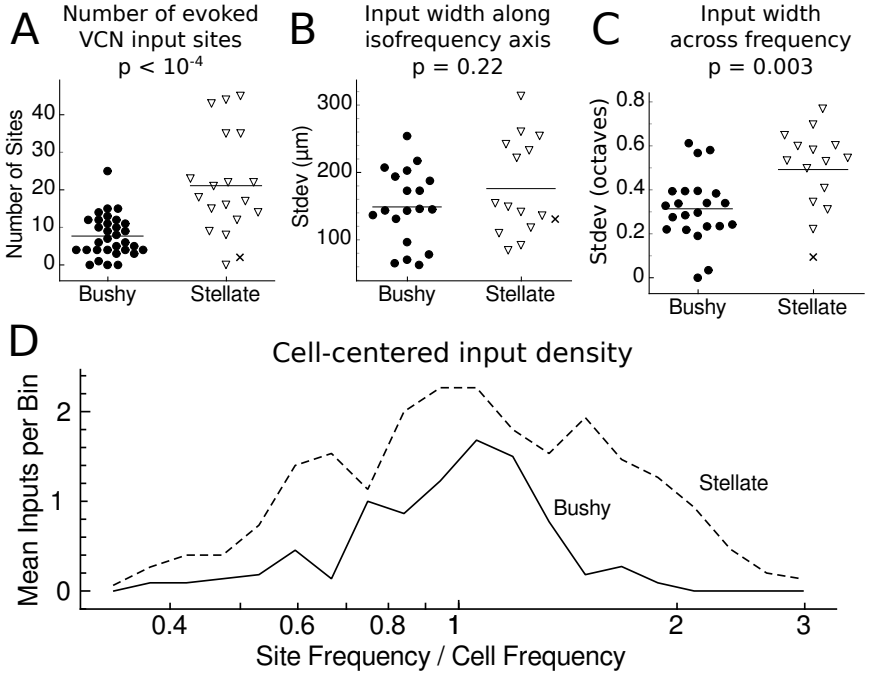

Figure 5.6: Bushy and stellate cells differ in their integration of AVCN inhibitory inputs. **A)** Stellate cells receive input from a larger number of stimulation sites than bushy cells. Each point in the scatter plot indicates the number of input sites detected for a single cell. **B)** The difference in input area between bushy and stellate cells is not due to differences along the isofrequency axis (parallel to auditory nerve fibers). The plot shows the standard deviation of the positions of input sites for each cell. **C)** Stellate cells integrate from a wider frequency range than bushy cells. The value of each point is computed as $stdev[log_2(CF_{site})]$ for the estimated frequencies of input sites to a cell. **D)** Histograms showing the average density of input sites across frequency for bushy and stellate cells. All input sites were pooled and binned into equal frequency intervals. The plotted values indicate the average number of input sites per cell and bin. Stellate cells appear to receive more inhibition than bushy cells from both on-center and off-center frequencies.

input sites. Since D-stellate cells themselves integrate excitatory inputs over a broad frequency range, the actual frequency range of inhibitory input to the targets of D-stellate cells will be wider than the numbers reported above.

Inhibitory input from DCN

In contrast to the variable organization of inhibitory inputs from within the VCN, inhibitory inputs from the DCN were more consistently organized (Figure 5.7). Previous studies have found that tuberculoventral cells in the DCN are the source of a tonotopically-matched inhibitory input to AVCN cells (Wickesberg and Oertel, 1988, 1990; Saint Marie et al., 1991; Wickesberg et al., 1991; Ostapoff et al., 1999). Our results are consistent with these studies. DCN inputs always arose from a narrow band that was parallel to the isofrequency sheets in the DCN (e.g. Figure 5.5B,E; Figure 5.7A,B). Inputs detected in tuberculoventral slices always originated in the deeper layers of the DCN, and always fell within a single, narrow isofrequency region. Furthermore, the location of this band orthogonal to the isofrequency plane is correlated with the location of the postsynaptic cell (Figure 5.7C,D; Pearson correlation coefficient=0.87, $p=2.5\times10^{-6}$, slope=0.93).

We recorded 42 maps for which DCN inputs were expected to be detected. These maps exclude parasagittal slices for which the lateral surface of the DCN was not removed, tuberculoventral slices that lacked the proper alignment, and all ascending slices. Of these maps, only 57% were found to have DCN input. It is unclear whether this reflects the normal distribution of DCN projections, or results from interruption of the tuberculoventral tract during slicing. Only one putative D-stellate cell had mapping over the DCN, and it had no input from this region.

Next, we quantified the shape of the DCN inputs (Figure 5.8) for comparison to the AVCN results in Figure 5.6. For the following analyses, only maps that were expected to have DCN input were included. Unlike in AVCN, we found no differences between bushy and stellate cells in the number of DCN input sites (Figure 5.8A; bushy=2.0$\pm$2.1; stellate=2.5$\pm$3.0; permutation p=0.62). The spatial range of DCN input sites within isofrequency sheets was also not different between bushy and stellate cells (Figure 5.8B; bushy=75$\pm$48 µm; stellate=99$\pm$49µm; permutation p=0.45).

We used ANOVA to compare the spectral range across cell type and input region (Figure 5.8C). We found significant effects of both cell type ($F_{1,35}$=22.6, $p=3.3\times10^{-5}$) and input region ($F_{1,35}$=33.5, $p=1.5\times10^{-6}$) as well as a significant interaction between the two ($F_{1,35}$=5.67, p=0.023). Posthoc comparisons using Tukey's HSD method determined that the spectral width of DCN inputs was significantly different from the width of VCN inputs onto both bushy (DCN to bushy=0.10$\pm$0.08 octaves; p=0.04) and stellate (DCN to stellate=0.16$\pm$0.09; $p=1.5\times10^{-5}$) cells. Furthermore, the spectral width of VCN inputs was significantly

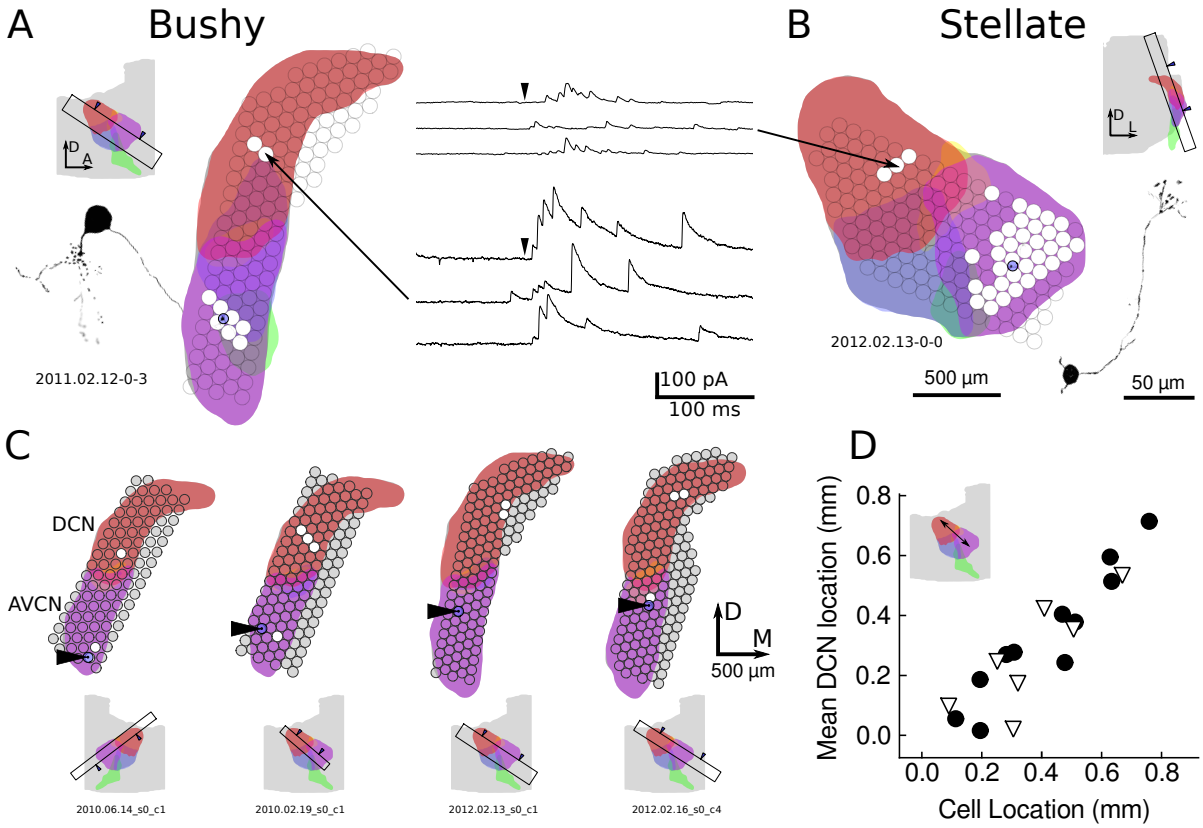

Figure 5.7: Inhibitory connectivity from DCN to AVCN. The format is described in Figure 5.4. **A)** Example map of bushy cell with DCN input. **B)** Example map of stellate cell with DCN input. **C)** DCN projections to VCN are focal and tonotopically organized. Maps from four representative cells in tuberculoventral slices show that the locations of DCN inputs are confined to a narrow region in the deep layer. Arrowheads indicate the location of the postsynaptic cell. **D)** The position of inputs along the tuberculoventral tract axis (indicated in inset) correlates with the position of the postsynaptic cell along the same axis in the AVCN. Position values are relative to an arbitrary origin within the 3D atlas.

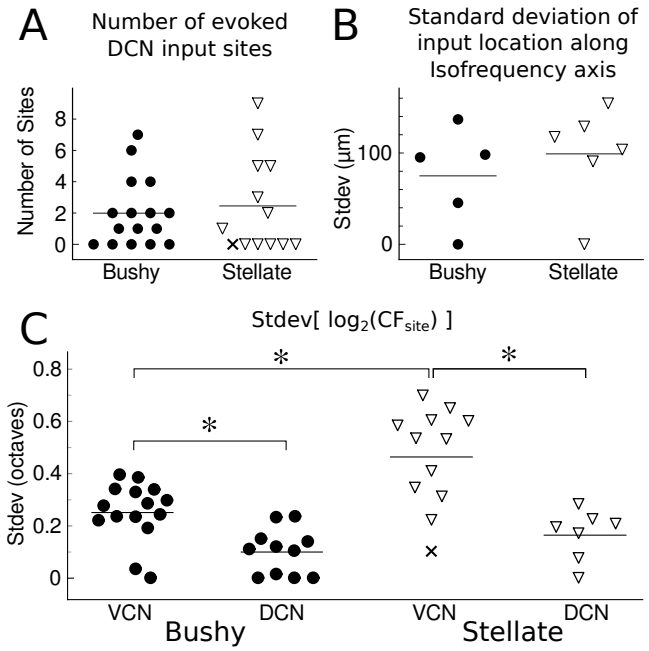

Figure 5.8: Bushy and stellate cells have similar integration of DCN inhibitory inputs. **A)** Number of DCN stimulation sites with detectable input per cell. The bushy and stellate cell distributions are not significantly different. **B)** Measurement of the width of DCN input area per cell. Each point in the plot indicates the standard deviation of input locations along an axis roughly parallel to the DCN isofrequency sheets. Again, the bushy and stellate distributions are not significantly different. **C)** Comparison of the standard deviation of input sites, in octaves, across cells. DCN inputs arise from a significantly narrower frequency span than AVCN inputs, for both bushy and stellate cells.

different between bushy and stellate cells, as seen previously ($p=4.5\times10^{-5}$), whereas the width of DCN inputs was not significantly different between bushy and stellate cells (p=0.79). These results confirm that DCN cells provide tonotopically restricted inputs to VCN cells.

Inhibitory input from the dorsal border of AVCN

Fifty-five maps were collected that included included photostimulation sites over the granule cell area at the dorsal border of the AVCN (25 bushy, 16 stellate, 14 other). In 10 of these maps (6 stellate, 2 bushy, 2 other), a third distinct source of inhibitory input was found. In parasagittal slices, these inputs were found to lie along the dorsal edge of the AVCN, often appearing as small clusters of 2–4 stimulation sites that were usually spatially separate from the larger AVCN input region (Figure 5.9A,D,E). In tuberculoventral slices, these inputs appeared along the dorso-medial border of the AVCN (Figure 5.9B,C). The strength and firing pattern of these dorsal-border inputs varied widely from cell to cell. Some cells showed long trains of fast IPSCs, whereas others showed only a single slow IPSC (e.g. Figure 5.9B and A, respectively), similarly to both AVCN and DCN inputs. The difference between the fraction of bushy vs stellate cells with this type of input was statistically significant (Fisher's Exact test; p=0.039).

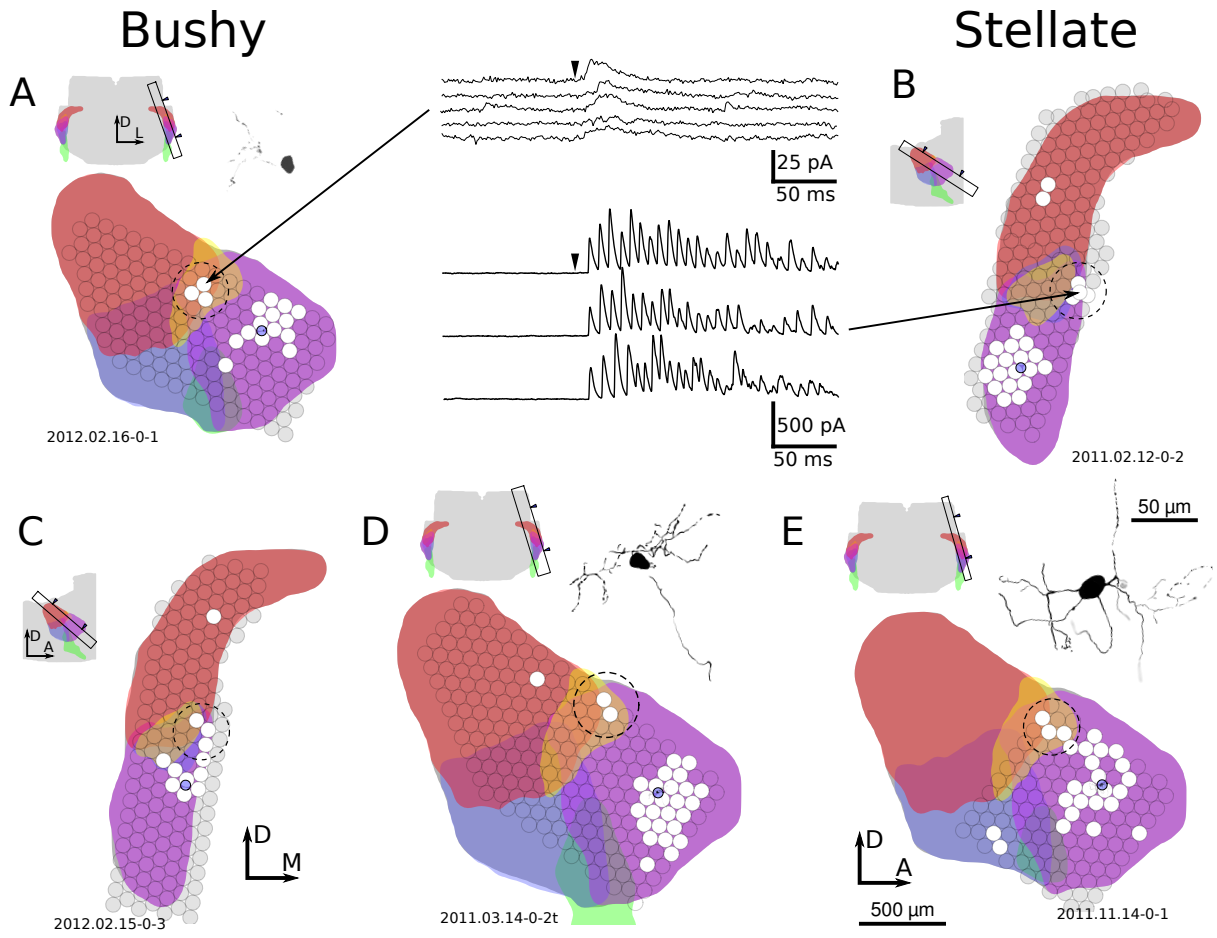

Figure 5.9: AVCN cells receive inhibitory input from the dorsal and medial borders of the AVCN. The format is described in Figure 5.4. Inputs at the dorsal and medial edge of the AVCN are indicated with a dashed circle. Maps **A** and **C** are bushy cells, **B** and **E** are stellate cells, and the cell type in **D** is ambiguous. Morphology was not available for the cells in B and C; their cell types were determined by physiological criteria.

Summary of inhibitory input

Figure 5.10A shows the combined, cell-centered, inhibitory maps across cell types and slice planes. Some of the features previously discussed are immediately apparent: both cell types have similar patterns of spatial convergence, integrating inputs mainly from DCN and nearby VCN with occasional input from the dorsal border of the AVCN. Inputs from VCN converge from a much broader range than those from DCN, particularly along the axis orthogonal to the isofrequency lamina. Stellate cells integrate from a much larger area of AVCN than bushy cells, although their DCN input areas are similar. Previously, Wickesberg and Oertel (1988) measured this connectivity by injecting horseradish peroxidase into the AVCN. They identified inputs from a narrow-frequency strip of DCN and also from a region of VCN dorsal to the injection site. Although our results regarding DCN inputs to AVCN agree with theirs, we did not find any preference for local inputs within the AVCN to be located dorsally. In our sample, the input arises from regions that are largely centered on the target cell.

From the parasagittal-plane maps in 5.10A, it appeared that the VCN input regions for both bushy and stellate cells were wider along the x-axis (isofrequency axis from posteroventral to anterodorsal) than along the y-axis (tuberculoventral tract axis). To test this we measured the per-cell standard deviation of site locations across both axes for each cell type, then compared the x and y axes. For bushy cells, spread is significantly larger along the x-axis than the y axis (x=151$\pm$50 µm; y=94$\pm$38µm; permutation p=0.006; n=12). This result suggests that the terminal fields of D-stellate cells may preferrentially extend within frequency bands, and supports a similar anatomical report by Arnott et al. (2004). For stellate cells, the same trend was apparent but not statistically significant (x=176$\pm$70 µm; y=146$\pm$48 µm; permutation p=0.25; n=12).

Excitatory input from AVCN

The axons of T-stellate cells have local collaterals that terminate within the VCN, and are believed to be a source of local excitatory input. To explore excitatory connectivity within the VCN, we mapped evoked EPSCs in 75 cells by holding each at -50 mV during photostimulation. Ferragamo et al. (1998b) reported that 44 of 54 T-stellate cells in the PVCN had long latency (polysynaptic) excitatory input following auditory nerve shock, and suggested that local excitatory connections arose from within the T-stellate population. In contrast, we detected excitatory inputs in only 5 of 75 cells (4 bushy cells and 1 stellate; Figure 5.11). Uncaging consistently produced trains of action potentials in cell-attached recordings from T-stellate cells, so it is unlikely that this difference is the result of a failure to stimulate the cells. Ferragamo et al. (1998b) recorded largely, although not exclusively, from T-stellate cells in the PVCN,

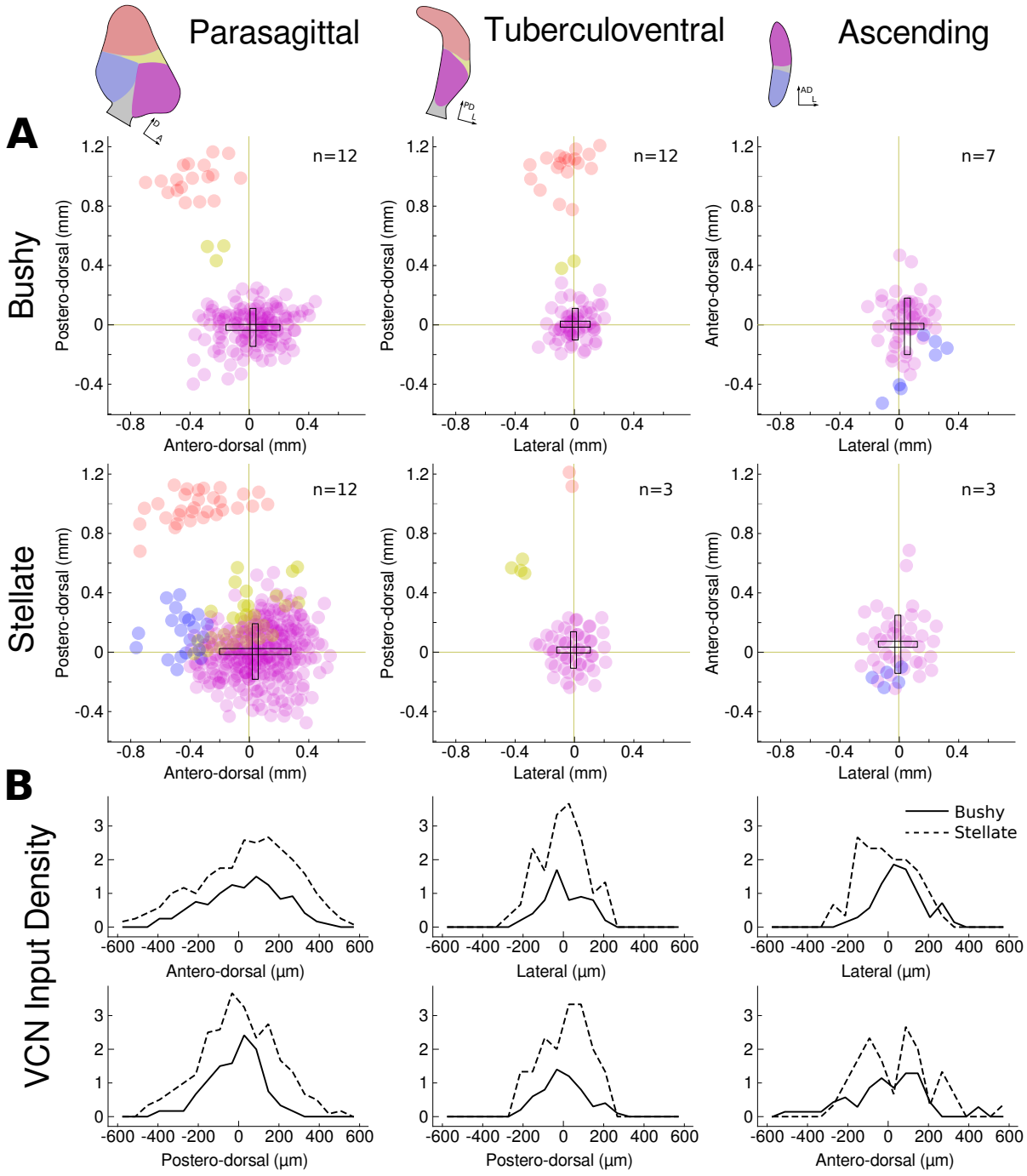

Figure 5.10: Combined maps and input density analysis of inhibitory connectivity. **A)** Cells were divided into groups based on cell type and slice plane, then maps were combined within groups and translated such that the postsynaptic cells all lie at the origin. Slice planes are described in Section 2.1 and Figure 2.1. Each spot indicates one detected input site from a single cell; colors indicate the anatomical region of the photostimulation site (green=AVCN, red=DCN, blue=PVCN, yellow=AVCN dorsal border). Black rectangles within the maps indicate the center and standard deviation of the entire population of input sites for either VCN or DCN. The parasagittal slice plane is rotated such that the ascending branch of auditory nerve fibers is roughly parallel to the x axis. **B)** Each plot shows histograms of the average density of VCN input locations across the x (top row) and y (bottom row) axes from the maps above. The histograms are normalized by the number of cells in the group.

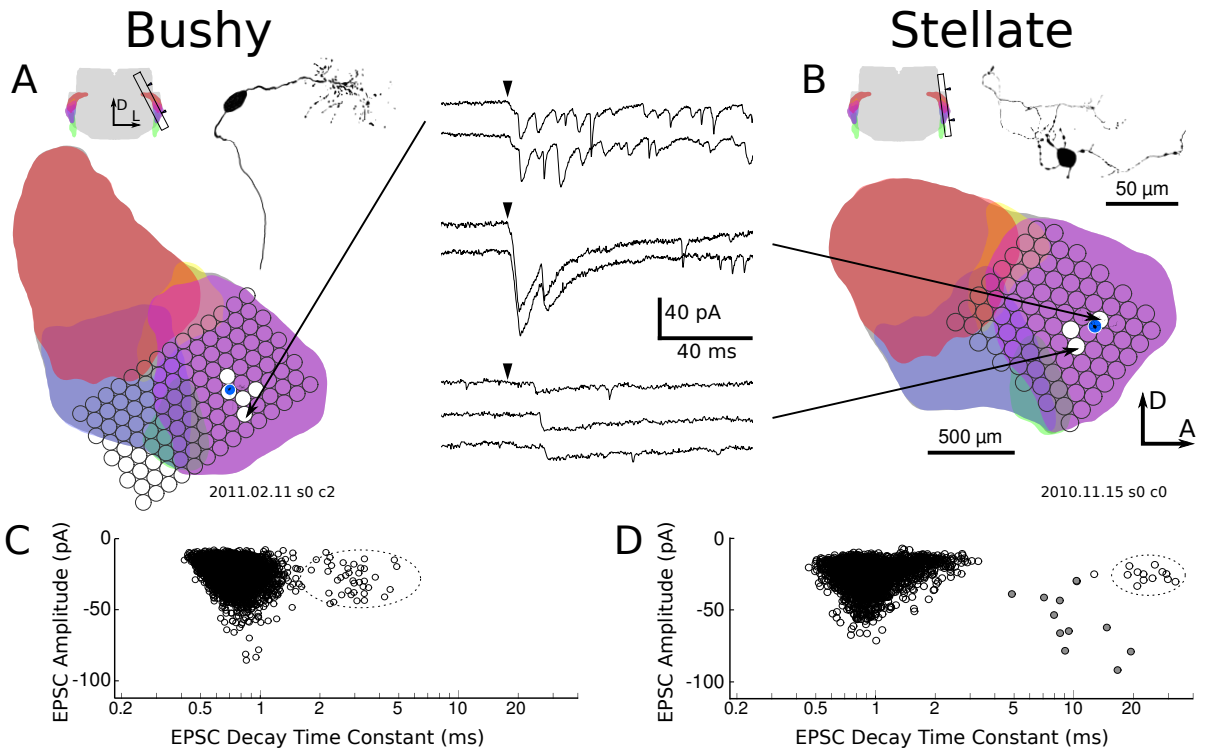

Figure 5.11: AVCN cells receive excitatory input from a local source. **A,B)** Maps of excitatory inputs to a bushy cell and stellate cell, respectively. The format is described in Figure 5.4. **C,D)** Scatter plots of events detected during all recordings for these cells. The circled regions include both spontaneous and evoked events that form a population with a slow decay time constant relative to the spontaneous release from auditory nerve fibers. The filled grey circles in (D) are direct stimulation responses.

whereas we recorded largely from cells located in the AVCN. Thus it is possible that the local networks have regional differences, and that the posterior T-stellate cell population is more highly interconnected. Furthermore, the local T-stellate terminals may have low release probability or few terminals on any given target cell, which would reduce their detectability in the presence of the high rates of spontaneous excitatory events. Despite the differences between these studies, it seems likely that T-stellate cells provide the local excitatory inputs observed in both.

The properties of local excitatory inputs have some surprising differences compared to auditory nerve inputs. Excitatory inputs were always found within 200 µm of the postsynaptic cell body and did not appear to be restricted to a narrow isofrequency plane. Thus the postsynaptic cell may receive excitatory inputs from cells of different frequency (e.g. Figure 5.11A), in contrast to their narrowly-tuned auditory nerve input. In 3 of the bushy cells with excitatory input, evoked EPSCs had a decay time-constant of 2–3 ms, which is distinctly slower than the ~1 ms decay of spontaneous auditory nerve PSCs. In each of these cells, a population of spontaneous EPSCs was also found with slower kinetics than auditory nerve EPSCs (Figure 5.11C, 5.2C). Four additional bushy cells exhibited similar populations of slow spontaneous

EPSCs, but had no detected evoked EPSCs. The stellate cell had evoked EPSCs that were much slower than the spontaneous auditory nerve EPSC population (Figure 5.11D), and two more stellate cells had bimodal EPSC distributions, but lacked local excitatory input. Together, these findings indicate that local excitatory input within the VCN may provide a different function than auditory nerve input.

A second source of local excitatory input was proposed by Gómez-Nieto and Rubio (2009), who suggested that gap-junctional coupling could provide local excitation amongst groups of bushy cells. We found no evidence for gap-junctional coupling in this study. However, a connection between adjacent bushy cells might be difficult to detect due to overlap of gap-junction and direct photostimulation currents.

5.4 Differences in inhibitory synaptic inputs to VCN neurons

The mapping results in Figures 5.6 and 5.10 show that that stellate cells, on average, receive inhibitory inputs from a wider region of the VCN than do bushy cells. In this section, we consider how the strength and kinetics of inhibition from the VCN and DCN varies with each of the target cell populations. Cells with access resistance greater than 30 MΩ were excluded from this analysis.

Xie and Manis (2013) reported previously that the decay time constant of IPSCs was significantly faster in stellate cells than bushy cells. To determine whether there are also differences between DCN and VCN inputs, we selected well-isolated events that appeared to have been evoked by photostimulation and compared their decay time constants across input region and postsynaptic cell type. Our results are consistent with those previously reported. The individual measurements were VCN to bushy=10$\pm$4.2 ms (n=10), DCN to bushy=19$\pm$4.7 ms (n=3), VCN to stellate=4.2$\pm$1.0 ms (n=11), DCN to stellate=4.0$\pm$2.2 ms (n=5). We found by ANOVA a significant effect of target cell type ($F_{1,53}$=55.1, p=9.4$\times10^{-10}$), but no significant effect of inhibitory source ($F_{2,53}$=1.81, p=0.17) or interaction between cell type and source ($F_{2,53}$=2.86, p=0.066). Post-tests (Tukey's HSD) showed significant differences for all comparisons between bushy and stellate cells, regardless of source. The trend toward faster inhibition from VCN onto bushy cells than from DCN is interesting, but requires further study.

The PSCs evoked by uncaging showed a wide variety of amplitudes and temporal patterns. IPSC amplitudes ranged from a detection limit of ~10 pA to hundreds of pA. Some stimuli were followed by a single, large IPSC, whereas others evoked long-lasting trains of IPSCs. The trains could exhibit a highly regular inter-event interval, suggesting that only a single stimulated neuron was activated, or could show more complex patterns suggesting that the events arose from multiple neurons.

We tested whether the amplitude of evoked IPSCs varies systematically between cell types or input regions. To test this, we measured the mean amplitude of events across stimulus sites within either the

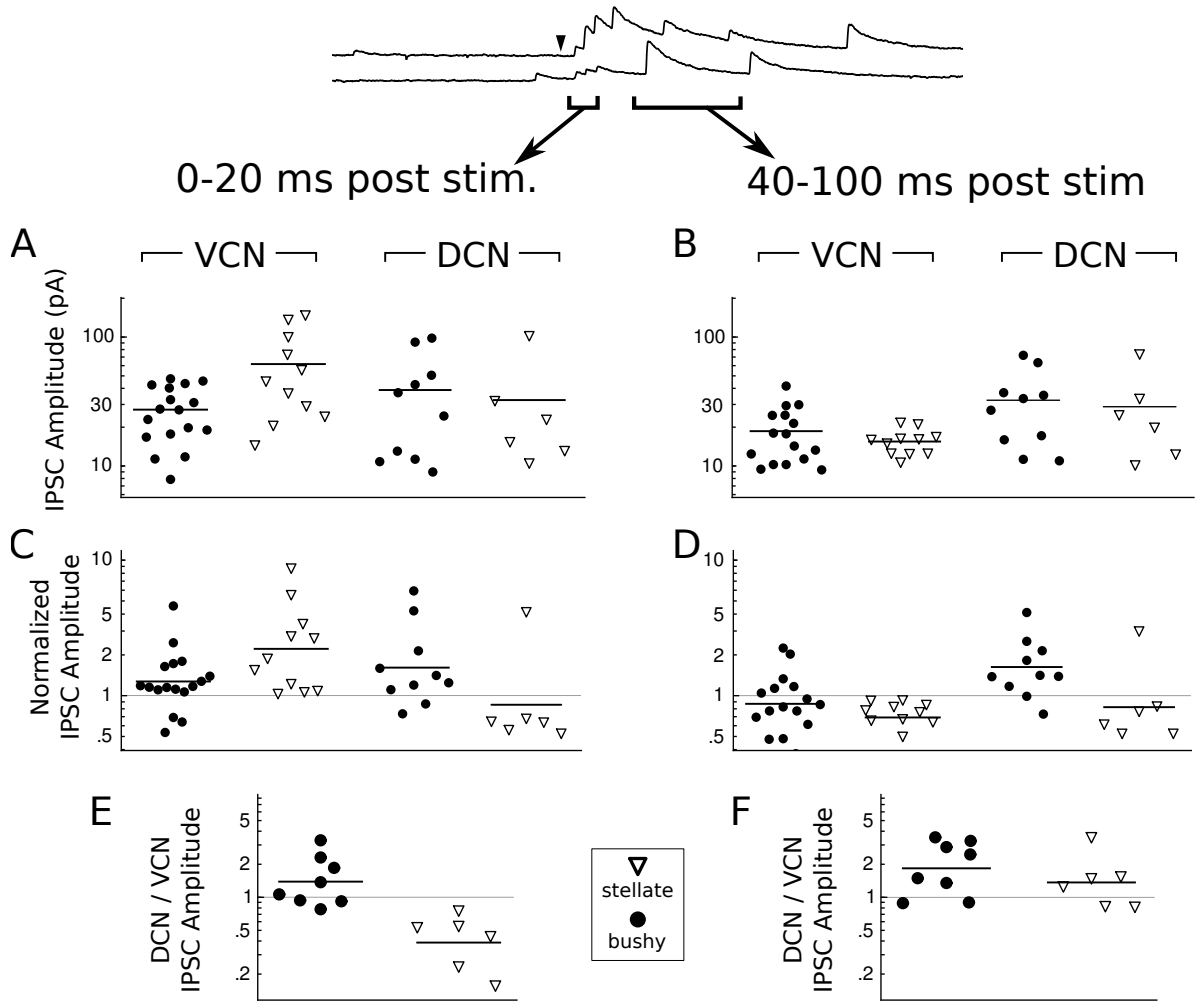

Figure 5.12: Evoked IPSC amplitude depends on both the input region and the target cell type. **A,B)** Evoked IPSC amplitudes for events 0–20 ms and 40–100 ms post-stimulus, respectively. **C,D)** IPSC amplitudes normalized by spontaneous IPSC amplitude per cell for the same time windows. **E,F)** Ratio of DCN / VCN IPSC amplitude for the same time windows. In all plots, each symbol indicates the mean of event measurements for the specified time range, region, and cell type. Bars indicate means in A and B, geometric means in C–F.

VCN or DCN that produced evoked responses in two time windows: from 3 to 20 ms and from 40 to 100 ms following stimulation (Figure 5.12). The first window frequently contains the largest events, whereas the second window contains primarily smaller, isolated events that appear to arise from presynaptic neurons that continue to fire long after the stimulus.

In both bushy and stellate cells, IPSCs evoked from within the VCN during the early (0-20 ms) window range from 1 to 5 times the amplitude of the spontaneous IPSCs in the same cells (Figure 5.12C; VCN). This result indicates that photostimulation over the VCN evokes events that are likely composed of multiple release events, although it is not possible to separate whether these arise from only one presynaptic cell with multiple synaptic terminals on the target cell, or from convergence from several activated cells. In bushy cells, IPSCs evoked from the DCN were similar to those evoked from the VCN. However, in stellate cells, DCN events were typically half the size of spontaneous events (Figure 5.12C; DCN). This could occur if the DCN synaptic inputs are located electrotonically distant to the cell body relative to the synapses producing the spontaneous events. It is not likely to result from rapid synaptic depression because IPSCs evoked by electrical stimulation of the DCN do not show strong depression at firing rates < 100 Hz (Xie and Manis, 2013). Events evoked from VCN in the late (40-100 ms) window had the same amplitude as spontaneous IPSCs in bushy cells, but again were smaller than spontaneous IPSCs in stellate cells (Figure 5.12D).

In cells that received both DCN and VCN inputs, paired comparisons were made to reduce variability. Comparing the early evoked amplitudes between the DCN and VCN in individual cells reveals that bushy cells trend toward stronger input from the DCN (Figure 5.12E; geometric mean ratio DCN:VCN = 1.4; 1-sample t-test $\ln[DCN/VCN] \neq 0$: $t_7=1.82$, $p=0.1$). Stellate cells had significantly stronger input from the VCN (geometric mean ratio DCN:VCN = 0.4; 1-sample t-test $\ln[DCN/VCN] \neq 0$: $t_5=3.92$, $p=.011$), which could be explained either by differences in convergence, or a segregation of inputs along the somato-dendritic axis due to dendritic attenuation of distant synaptic inputs. The difference between the two cell targets was significant (permutation $p<10^{-4}$), and demonstrates cell-type differences in convergence between DCN and VCN inhibitory inputs. Stellate cells strongly favor inhibition from within the VCN, which perhaps reflects their emphasis on spectral processing relative to bushy cells.

5.5 Negative Results

Over the course of analyzing the results from these experiments, we searched for correlations between several different types of measurements. The cases where we found interesting correlations are detailed above. In many cases we did not find correlations where they might have been expected. A sample of

these negative results are detailed below.

First, we found no relationship between the location or frequency of the postsynaptic cell and any of its input properties. This means, for example, that high-frequency cells seem to have the same patterns of input as low-frequency cells. Second, we found that a subset of VCN cells respond to direct photostimulation with a large, prolonged inward current lasting hundreds of ms (Section 5.2). We wondered whether this property was specific to a certain cell type or correlated with other cell properties (in particular, the presence of multiple populations of spontaneous EPSCs). We found no correlations in these properties. Third, no relationships were found between the location of presynaptic sites and strength, decay time constant, or firing patterns evoked from that site.

Chapter 6

Discussion

Inhibition from the central VCN

Previous reports have shown that collaterals of D-stellate axons branch profusely in the VCN (Arnott et al., 2004) and that the terminals of these axons contain flattened and pleomorphic vesicles similar to those found in synapses on both bushy and stellate cells (Cant, 1981; Smith and Rhode, 1989; Ostapoff and Morest, 1991; Doucet et al., 1999). Furthermore, electrical stimulation of the auditory nerve root in cochlear nucleus slices evokes delayed glycinergic inhibition in stellate cells, even in the absence of the DCN (Ferragamo et al., 1998b). These studies and others strongly suggest that D-stellate cells provide local inhibitory input within the VCN. Our results demonstrate the first direct measurements of the functional connectivity in this pathway.

Several single-unit recording studies have found stronger inhibitory sidebands in the frequency-response areas of chopper units (T-stellate) than both primarylike (bushy) and onset chopper (D-stellate) units (Martin and Dickson, 1983; Smith and Rhode, 1989; Rhode and Greenberg, 1994b). In part, this likely results from their differing dendritic architecture. Bushy cells have compact, highly-branched dendritic arbors with the majority of synapses concentrated on the soma, axon hillock, and proximal dendrites. In contrast, T-stellate cells have long, sparsely-branching dendrites with the majority of synapses concentrated on their dendrites. Consistent with the single unit studies, we found that stellate cells received inhibitory inputs from approximately twice as many VCN stimulation sites as bushy cells, and those sites spanned a wider frequency range. Likewise, the convergence of inhibitory inputs for each stimulation site was increased in stellate cells relative to bushy cells. We have also found that the strength and spatial extent of VCN inhibition is highly variable from cell to cell, particularly in stellate cells, which echoes several studies describing VCN inhibition *in vivo* (Evans and Nelson, 1973; Goldberg and Brownell, 1973; Brownell, 1975; Martin and Dickson, 1983; Paolini et al., 2005).

D-stellate cells have comparatively broad frequency receptive fields combined with temporally sharp

response properties (Smith and Rhode, 1989). Since they provide wideband inhibition, it is natural to expect that they reduce the sensitivity of postsynaptic cells to wideband sounds. Thus D-stellate cells may increase the *spectral contrast* of bushy and T-stellate cells, enabling them to selectively encode the timing and amplitude of narrow spectral peaks. This may be particularly important for T-stellate cells, which encode the envelope of sound within their excitatory receptive field (Shofner, 1999). It has been suggested that wideband inhibition improves the signal detection in background noise (Rhode and Greenberg, 1994b; Caspary et al., 1994; Ebert and Ostwald, 1995b). Taking this hypothesis one step further, D-stellate inhibition may allow T-stellate cells to more precisely encode the amplitude and envelope of spectral peaks even in the presence of rapidly fluctuating background noise.

The idea of spectral contrast should not be confused with the spectral *sharpening* proposed in several other studies, in which postsynaptic cells would become less responsive to off-center, narrowband frequencies (Rhode and Greenberg, 1994b; Kopp-Scheinpflug et al., 2002). Rather, it is more consistent with CMR (Pressnitzer et al., 2001) and with the idea that inhibition decreases sensitivity to broadband noise while increasing the dynamic range available for encoding sound of interest (Rhode and Greenberg, 1994b). The fast kinetics of D-stellate synapses onto T-stellate cells is particularly important for CMR, since this requires inhibition that can follow rapid envelope changes in the background noise (Pressnitzer et al., 2001; Xie and Manis, 2013). Bushy cells have comparatively slow input from D-stellate cells, and thus may only be sensitive to CMR for slowly-modulated background noise (Xie and Manis, 2013).

The difference between bushy and stellate cells in the range of frequency over which they integrate D-stellate input is particularly surprising, since it would seem that bushy cells could benefit from reduced sensitivity to background noise, just as stellate cells do. It was suggested in Chapter 1 that, in order to produce a *predictable* output spike train, a single bushy cell must integrate auditory nerve input from fibers having similar frequency and intensity response properties. In theory, this would allow sound localization nuclei to make single-spike comparisons between bilateral bushy cell inputs. Thus it may follow that bushy cells also require relative homogeneity in their inhibitory inputs as compared to T-stellate cells. In other words, even though an individual bushy cell might benefit from broader inhibition, integrating from an area that is too large could impact the predictability of the cell's output, and thus add noise to binaural computation of location.

Inhibition from the DCN

Another source of inhibitory input comes from cells in the deep layer of the DCN, presumed to be tuberculoventral neurons. These cells are believed to correspond to a subset of the "Type II" units in DCN, which have high thresholds and narrow frequency receptive fields that are matched in frequency to their

postsynaptic targets (Young and Voigt, 1982). They provide a temporally-delayed inhibitory feedback to the VCN that is thought to perform many functions including echo suppression, spike timing control, and dynamic range optimization (Wickesberg and Oertel, 1990; Caspary et al., 1994; Xie and Manis, 2013).

The pattern of connections that we measured from the DCN agrees closely with previous anatomical and functional studies showing a precise tonotopic projection from DCN to VCN (Feng and Vater, 1985; Wickesberg and Oertel, 1988, 1990). We found that both bushy and stellate cells receive tuberculoventral input from a narrow band oriented parallel to the isofrequency sheets in the DCN. Although the DCN input area was the same for both cell types, stellate cells have significantly weaker IPSCs than bushy cells from DCN.

Tuberculoventral cells are believed to receive excitatory input from both auditory nerve fibers and T-stellate cells (Feng and Vater, 1985; Wu and Oertel, 1986; Zhang and Oertel, 1993). They have narrow tuning curves, tonic firing patterns, and relatively high thresholds (Young and Voigt, 1982). By providing slower input to bushy cells through both their firing pattern and synaptic kinetics, they provide a *temporal contrast* that likely facilitates gain control by subtracting out the slower sound envelope, leaving more dynamic range for representing rapid changes in the sound level. This type of input is ideally suited to enhance the response to amplitude-modulation since it would decrease sensitivity to the unmodulated portion of the signal. Bushy cells were found to have stronger tuberculoventral input than T-stellate cells, which is consistent with previous studies showing that, in response to amplitude-modulated sound, bushy cells have better synchronization and increased modulation depth, particularly in the presence of background noise (Rhode and Greenberg, 1994a; Wang and Sachs, 1994). In contrast, T-stellate cells preserve their sensitivity to the slow sound envelope, so tuberculoventral input is expected to be less useful in this context.

It has also been hypothesized that tuberculoventral cells provide monaural echo suppression (Wickesberg and Oertel, 1990). This is particularly interesting for bushy cells since they are involved in sound localization, and any response to an echo might decrease localization accuracy. However, the high thresholds of tuberculoventral cells cast some doubt on this hypothesis.

Due to the small number of D-stellate cells in this study, we were unable to determine whether these cells receive input from tuberculoventral cells. This will be an important question to answer because it is not clear whether D-stellate cells would receive narrow-band inhibition as bushy and T-stellate cells do, or if they would receive inhibition from a broad range of frequencies. The functional implications of these possible connections are similarly unclear.

Inhibition from the dorsal border of AVCN

Together, D-stellate and tuberculoventral cells provide the majority of intranuclear inhibitory synaptic input to the bushy and stellate cells. However, a third source of inhibition was evoked from sites at the dorsal and medial borders of the AVCN. This inhibition appears to arise from an anatomically distinct population of cells. Although some of these input sites appeared to reside entirely within the AVCN, those found along the dorsal border may arise from within the AVCN or from the adjacent granule cell area. These possibilities are difficult to distinguish in this study because of the limited spatial resolution of the photostimulation maps and overlap of anatomical regions within the depth of the slice.

Two candidate sources are the marginal stellate cells (Doucet and Ryugo, 1997; Palmer et al., 2003; Doucet and Ryugo, 2006) and the commisural multipolar cells (Doucet and Ryugo, 2006) found in these regions, although it is not clear whether these are excitatory or inhibitory cells. The functional significance of these inputs is not clear, although they may provide a source of non-auditory input (Ghoshal and Kim, 1996a). Another possible candidate is the Golgi cell population located in the granule cell area between AVCN and DCN (Ferragamo et al., 1998a). However, because Golgi cell bodies and axonal domains are largely restricted to the granule cell area, it is unlikely that they could account for all of the border inputs seen in this study.

Excitatory input from the VCN

Previous anatomical studies have shown that the axons of T-stellate cells have prominent collaterals in the VCN that terminate within or near the isofrequency lamina occupied by their dendrites (Oertel et al., 1990, 2011), and contain small spherical vesicles, consistent with an excitatory transmitter (Smith and Rhode, 1989). Furthermore, non-primary excitatory synapses with small spherical vesicles are present on stellate and bushy cells (Cant, 1981; Smith and Rhode, 1987; Ostapoff and Morest, 1991). The other major population of excitatory cells in the cochlear nucleus, the granule cells, neither reside in nor project to the magnocellular regions of the VCN (Mugnaini et al., 1980), and so are not candidates for local excitatory circuits. It seems most likely that the few excitatory inputs found in the present study originate from T-stellate cells.

Seven bushy cells were found to have bimodal distributions of sEPSC decay kinetics, which to our knowledge has not been reported previously in the VCN. The fast mode is consistent with the decay kinetics previously seen for bushy cell EPSCs from auditory nerve synapses. These synapses are thought to contain AMPA receptors that lack the GluR2 subunit and are composed of the GluR3 and 4 flop splice variants, which endow them with exceptionally fast kinetics (Ryugo and Parks, 2003; Cao and Oertel, 2010;

Wang and Manis, 2005). Stellate cells have slower, GluR2-containing auditory nerve synapses (Cao and Oertel, 2010) as do bushy cells in a mouse model of hearing loss (Wang and Manis, 2005). Taken together, our observations suggest that bushy cells may have AMPA receptors with two different configurations of subunits, but that the GluR2-lacking receptors associated with the auditory nerve input are the dominant class. Three of the bushy cells with bimodal sEPSC distributions also had evoked excitatory inputs, and in each case, the decay time constant of evoked events was similar to the slower spontaneous EPSCs. This suggests that AMPA receptor composition at synapses on bushy cells depends on the presynaptic input source, and that T-stellate inputs to bushy cells are a source of slower excitatory input, possibly associated with GluR2-containing AMPA receptors. In a few cases, excitatory input sites appeared to span up to 250 µm orthogonal to the auditory nerve fibers, indicating that they may have come from cells whose center frequency was different from the postsynaptic cell, although the span suggests that this range corresponds to less than 0.5 octaves. Together, these suggest a surprising result that bushy cells, whose properties are so uniquely reliant on the sharp temporal and spectral response properties of their auditory nerve inputs, also receive excitation that is comparatively slow, imprecisely timed, and spectrally broad.

Only three stellate cells were found with bimodal sEPSC distributions. Given that auditory nerve EPSCs are considerably slower in stellate cells than bushy cells (about 3 ms at 25 °C), it is possible that this population of sEPSCs is associated with secondary sources that cannot be distinguished by kinetics alone. However, of the 24 stellate cells in this study, none had detectable evoked events with ~3 ms decay time constant.

In all cells with local excitatory input, we were able to evoke excitatory events from 2 to 5 different stimulation sites. In some cases, discontinuities in the excitatory input areas suggests that the input came from multiple cells. This is surprising given that local excitatory connections were so rare in the VCN, and raises the possibility that some cells are more engaged with local excitatory circuits than other cells. This interpretation is also supported by the finding that only a fraction of cells had bimodal EPSC distributions, and that these were more often found in cells with local evoked excitatory inputs.

Looking forward

Although this work has made significant progress in revealing the circuitry of the cochlear nucleus, several aspects of the circuit have yet to be explored. First, D-stellate cells are poorly represented in this data set because they make up a small fraction of cells in the cochlear nucleus. Future mapping studies in transgenic mice with fluorescently labeled D-stellate cells may address this. Second, while the PVCN is in many respects a contiguous nucleus with the AVCN, it is still necessary to measure connectivity to PVCN cells, particularly with attention paid to the disparity in excitatory input seen between this study and that

of Ferragamo et al. (1998b). Third, to model tuberculoventral inputs to the VCN, it will be necessary to determine whether these cells receive input from either of the VCN cell types that project to DCN. Both D- and T-stellate cells project to the DCN and may form recurrent connections with tuberculoventral cells. Fourth, input from the SOC is believed to comprise a significant portion of inhibition to VCN cells. Mapping these connections will be more difficult due to the long distance of these projections. An optogenetic approach that selectively labels projections from the SOC could be used to activate axon terminals, but this would not provide information about the spatial organization of these connections. Finally, many synapses that make up the VCN circuit have unknown short-term plasticity dynamics. From this study, it appears that the temporal control provided by glutamate uncaging is insufficient for determining synaptic dynamics. An optogenetic approach may be more productive, but it is not yet clear whether transgenic mice exist with the necessary cell-type specificity. Another approach would be to attempt paired recordings guided by newly-developed 2-photon stimulation of single cells. Such experiments would provide the most unambiguous results and at the same time allow imaging of both pre- and postsynaptic cells to determine synapse location. In having developed the tools and techniques needed to carry out this research, it is my hope that these problems may be addressed more quickly in the future.

Despite the remaining unaddressed questions about VCN connectivity, this study reveals an important component of the VCN circuit and is useful for model development. The difference between bushy and stellate cells in the range of frequency over which they integrate inhibitory input is particularly surprising. To begin to develop hypotheses about the functional relevance of this result, it may be useful to simply model the circuits and test them against a battery of physiological tests such as frequency response area, sensitivity to amplitude-modulated sound, and comodulation masking release. Then, simply swap the inhibitory connectivity between bushy and stellate cells to see whether and how this affects the output. This is a perfect example of the power and importance of modeling; designing an experiment to ask the same questions would be prohibitively difficult, but any positive results from the model may inform the design of new experiments.

It was suggested above that bushy cells may require their D-stellate input to be more spectrally restricted in order to preserve the predictability of their firing pattern. At the same time, the broader and stronger D-stellate inhibition on T-stellate cells may improve their ability to encode the precise amplitude of spectral features even in the presence of rapidly changing background noise. Both of these cases could be simply modeled by observing the ability of each cell type to encode timing or amplitude, while manipulating the spectral breadth of their inhibitory input. A simple model could confirm or refute these hypotheses, yet the equivalent *in vivo* experiment is currently beyond our capabilities.

Another possible modeling study comes from the idea, discussed in Chapter 1, that bushy cells may encode amplitude through spike latency, and that this latency is used centrally to compute interaural level differences. In this context, one function of inhibition may be to alter spike timing to improve the dynamic range available for measuring signal amplitude in the presence of background noise. This would be particularly important when the background noise is not identical in both ears; bushy cells must be able to encode the amplitude of a select component of the auditory signal so that binaural differences in background level to not affect the ability to measure sound location. Due to the difficulty of simultaneously recording the convergent inputs of bushy cells on either side of the brain, this is another example of a situation that calls for a relatively simple model based on the known inhibitory connectivity, yet may be difficult to demonstrate *in vivo*.

Finally, an important use for a cochlear nucleus model will be to determine what effects cochlear implants and brainstem implants have on the output properties of the cochlear nucleus. An important consequence of the spatially-imprecise electrical stimulation seen in cochlear implants is that the activity of large groups of auditory nerve fibers may become highly synchronized. The impact of excessive synchronization is not known, but could be evaluated in the context of an accurate cochlear nucleus model.

It is possible, for example, that stellate cells depend on integration of numerous unsynchronized inputs in order to produce tonic firing and thus a better estimate of envelope amplitude. Highly synchronized input, therefore, may cause T-stellate cells to fire more phasically. Likewise, given the temporal differences in the output between D-stellate and tuberculoventral cells, it is plausible that these may respond differently to over-synchronized input. Accurate models of these cell types could provide an estimate of the effects of cochlear implant stimulation, and suggest corrective stimulation strategies.

Because of the membrane dynamics of bushy cells, they depend on synchronization as a measure of sound intensity. Louder sounds produce more synchronized firing in auditory nerve fibers, which decreases the spike latency of the bushy cell (Rothman et al., 1993; Xu-Friedman and Regehr, 2005). In the context of cochlear implant stimulation, highly synchronized auditory nerve fibers would impart little information about sound amplitude to bushy cells, thus flattening their spike latency response and ultimately impacting the ability of the SOC to encode sound location. A simple approach to correcting this would be to artificially introduce amplitude-based latency in the cochlear implant stimulus. Since inhibition is hypothesized to play a role in removing background noise from the spike latency encoding, it would be important to model the effects of cochlear implant stimulation strategies in the context of the complete inhibitory circuit.

Closing

It is my hope that the tools and techniques developed in this dissertation will serve as a future template for measuring patterns of functional connectivity, while the experimental results will allow the development of more accurate models of the cochlear nucleus. With continued research into the cochlear nucleus circuit, such models may eventually provide a reliable source of input to models of more central auditory nuclei. By pushing steadily inward, the model of the auditory system may become progressively more complete. As we understand more of the components in this system, we are encouraged to ask increasingly high-level questions about its overall behavior, and a model of great complexity may become the most powerful tool for exploring the function of large neuronal networks.

Appendix A

Optical system design

To facilitate both laser scanning photostimulation and 2-photon imaging, an optical system was designed and implemented to convert a Zeiss Axioskop FS-2 microscope to support laser input. The design is based on standard laser scanning systems which use a two-lens telescope to solve two optical constraints simultaneously: First, a set of galvometric scanning mirrors are imaged onto the back of the microscope objective (Figure A.1C). This constraint is met by ensuring that the distance from the scan mirrors to the back aperture of the objective is equal to twice the sum of the scan and tube lens (Figure A.1D,E) focal lengths. This allows the beam to be steered with the scan mirrors while remaining stationary at the back of the objective. The mirrors then control the incident angle of the beam onto the objective, which translates to changes in the position of the beam's focal point on the sample. The second constraint is that the beam must be collimated when it enters the objective to ensure that the beam converges at the correct distance after exiting the objective. This constraint is met by ensuring that the distance between the scan and tube lenses is equal to the sum of their focal lengths. The selection of focal lengths is determined by the desired beam expansion. For 2-photon imaging, expansion ensures that the laser beam fills the entire back aperture of the objective, thus providing maximal imaging resolution. We selected 50 and 150 mm lenses for this purpose. For UV photostimulation, two 100 mm lenses were selected to reduce beam expansion. This results in a narrower column of illumination at the sample which increases both spatial resolution and effective depth for photostimulation. We also placed an adjustable telescope (two 100 mm lenses) on the table in the path of the UV laser to allow adjustment of the beam divergence. The distance between these lenses was set such that the size of the spot was 90 µm in diameter at the sample. All components were mounted in a 30 mm optical cage (Thorlabs).

Added to the standard laser scanning system is an LED illumination assembly (Figure A.1A) which provides both green and blue widefield illumination via a movable mirror (Figure A.1B). The LEDs are collimated, and thus must enter the optical pathway *after* the scan lens. This ensures that the LED illumination is properly focused by the tube lens, resulting in smooth widefield illumination at the

sample.

To monitor laser power, we used a UV beam sampler (BSF05-UV, Thorlabs) to divert a small portion of the beam onto a photodiode (HUV-1100BG). This photodiode package includes a low-noise amplifier that was used to output a photocurrent measurement to an analog input on the DAQ (Figure A.2). The photodiode was used in photoconductive mode (reverse-biased, 15 V) to improve response time and generate a linear output. The output of the photodiode was calibrated and monitored by ACQ4 (Chapter 4) and used to automatically adjust the photostimulation pulse duration to maintain constant pulse energy.

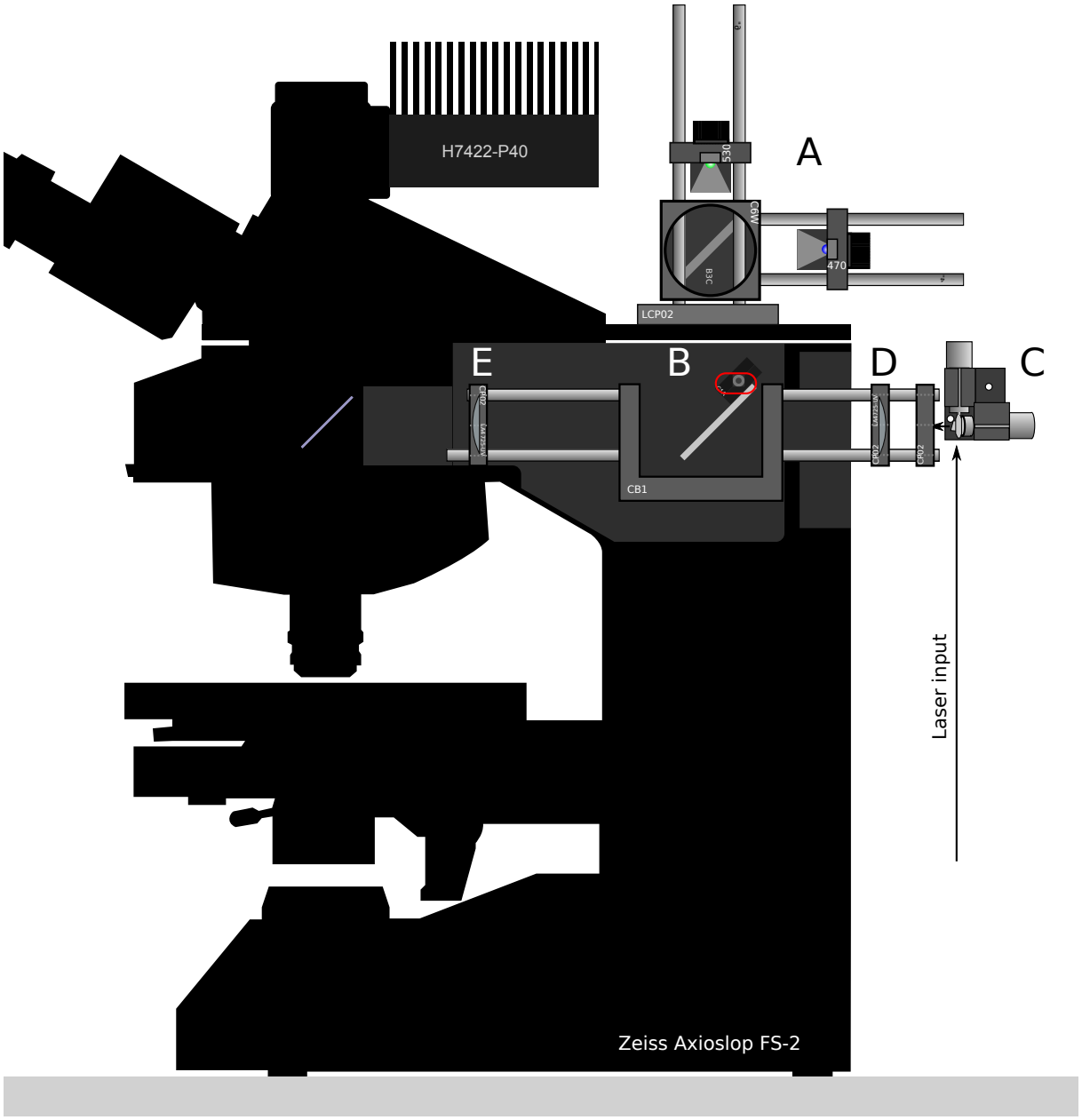

Figure A.1: Optical design of laser scanning system for Axioskop FS-2. The scanning optics occupy the cavity inside the microscope which normally houses the epifluorescence illumination train. **A)** LED illumination assembly. Two collimated, high-intensity LEDs are combined via dichroic mirror and directed into the scope through a 2.5 cm hole drilled into the top plate. **B)** A flippable mirror reflects light from the LEDs toward the filter carousel when positioned downward. Note that the tube lens (E) decollimates the LED beams to produce even illumination on the sample. In the upward position, the mirror allows laser illumination to pass from the scan mirrors to the filter carousel. **C)** Scanning mirrors reflect three nearly-colinear laser beams into the epifluorescence port on the microscope. All three beams converge on the center of the first scanning mirror. **D)** 100 mm focal length scan lens (or 50 mm to provide beam expansion). **E)** 100 mm focal length tube lens (or 150 mm to provide beam expansion). Individual part numbers (Thorlabs) are listed in the diagram.

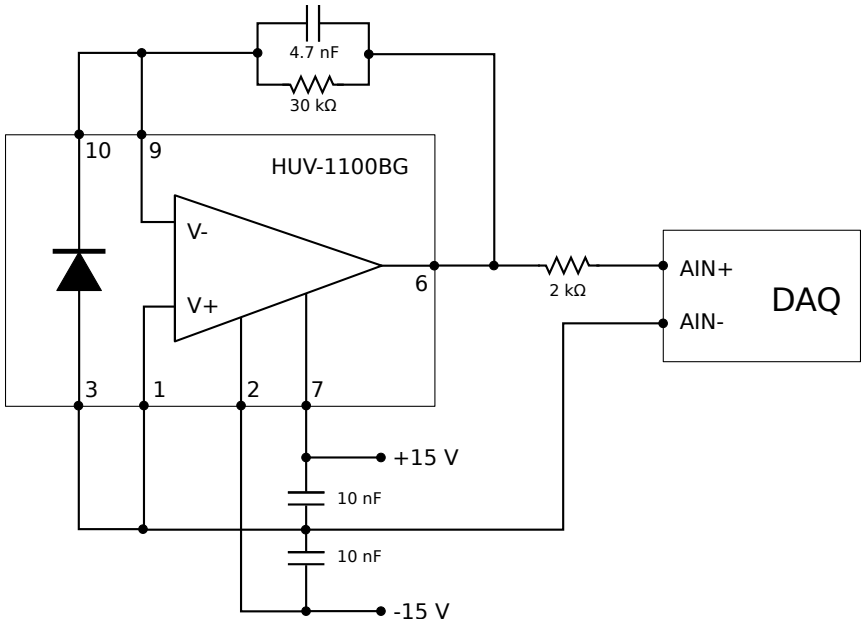

Figure A.2: Schematic of photodiode circuit used for laser power measurement. The circuit is based around the HUV-1100BG, which includes its own low-noise amplifier. The circuit design operates the diode in photoconductive mode, with a reverse bias of 15 V. The amplifier feedback is low-pass filtered with a cutoff frequency of 1.1 kHz.

Appendix B

MP285 interface

In the design of ACQ4 (Chapter 4), position-awareness is a recurring theme. All devices which have a defined spatial relationship to the subject (usually a brain slice) are calibrated such that ACQ4 understands that spatial relationship and can automatically register disparate types of data from multiple devices such that they occupy the same coordinate system. This greatly simplifies the task of data analysis, which would otherwise require tedious manual alignment. Alternatively, this effort might simply be avoided by fixing the microscope in a single location for the duration of each experiment. In situations where the slice is much larger than the visible range of the microscope, this may be an unacceptable approach. To provide this automatic registration, ACQ4 supports the use of the Sutter MP-285 controller for motorized stages and manipulators. This controller provides a serial interface to the computer which ACQ4 uses to periodically poll the position of the microscope stage.

We discovered a problem with this approach, which is that a design flaw in the MP-285 prevents simultaneous input from the serial port and the ROE used to direct the stage. To work around this problem, a microcontroller device was implemented which intercepts data from both the ROE and serial port, then forwards this data to the MP-285 while ensuring that collisions are handled gracefully. Specifically, serial commands are never sent to the MP-285 within 1 second of sending ROE input. To maintain good responsiveness while the ROE is in use, the microcontroller counts digital pulses from the ROE and uses this to estimate the motion of the stage. After ROE movement has ceased, the MP-285 is polled for its actual position to correct the estimate. This is not a perfect solution, but nevertheless solves the major issues. The technical details are summarized in Figure B.1, and the source code used to program the microcontroller is distributed with ACQ4.

An extra benefit to this approach is that we can provide new features not available on the MP-285, such as position limits that prevent equipment damage caused by excessive stage movement, as well as making the ROE buttons reprogrammable.

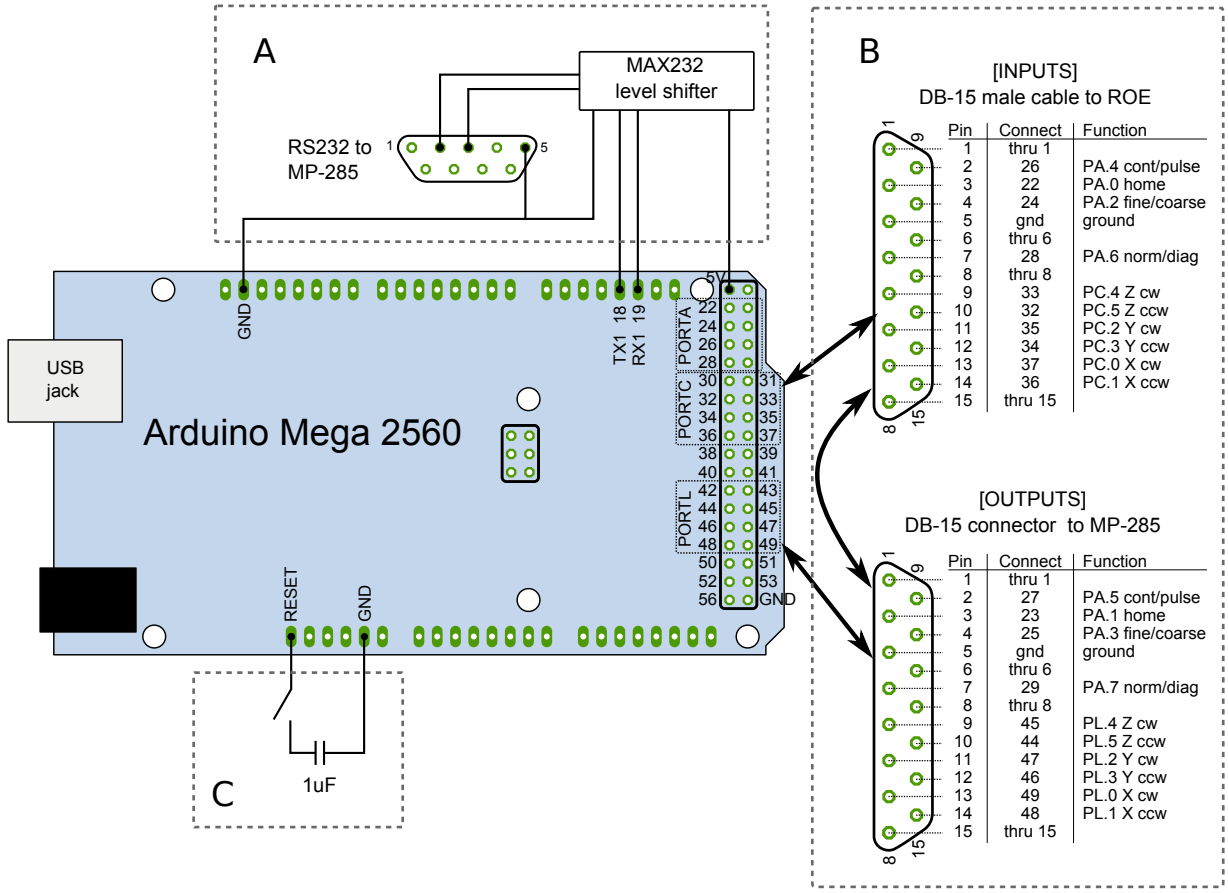

Figure B.1: Schematic of MP-285 interface. **A)** RS232 connection between the microcontroller and the MP-285 serial interface. It is necessary to convert between RS232 -12V (low) / 12V (high) and TTL 5V (low) / 0V (high). In the original design this is achieved this with a 50% voltage divider and a 7404 inverter. Another approach would be to use an RS232 level shifter, as shown. **B)** Two DB-15 connectors are used to interrupt data from the ROE to the MP-285. Pins 1, 6, 8, and 15 connect directly from one connector to the other. Pins 2, 3, 4, and 7 carry signals for the 4 buttons on the ROE. Inputs (from ROE buttons) connect to the even bits on port A, while outputs connect to the odd bits. Pins 9-14 carry the actual rotary encoder signals. Inputs connect to port C and outputs to port L. **C)** Ordinarily, initiating a serial connection to the Mega causes it to reset. When connected, this capacitor disables the auto-reset, allowing the processor to continue running uninterrupted. The switch must be opened in order to reprogram the board, since that process requires the auto-reset functionality.

Appendix C

Laser depth measurements

When considering the spatial organization of photostimulation maps, it is important to take into account that the laser beam diverges and scatters after it reaches the sample. Accordingly, the strength of photostimulation decreases with depth, and the diameter of the beam increases. Ideally one would like to know the probability that a cell will respond to photostimulation as a function of the cell's depth within the slice. In practice this is a difficult relationship to measure. To provide an indirect estimate of this relationship, we devised an experiment to determine the spatial profile of the laser beam as it travels through the tissue by photobleaching slices perfused with fluorescent dye, then imaging the cross-section of the bleached area. The purpose was to get a rough idea of how quickly laser intensity falls off at greater depths, and whether beam divergence significantly affects mapping resolution.

We cut 500 µm thick coronal cortical slices from one mouse. The slices were incubated for 2 hours in oxygenated ACSF (Chapter 2) with lucifer yellow. Slices were then fixed in 4% formaldehyde to prevent dye diffusion and placed in the recording chamber. The laser optics were focused to produce the smallest possible spot, then scanned in straight lines across the sample. The slices were then embedded in agar and cut again perpendicular to the direction of the photobleached stripes. Under fluorescence illumination, the cross-sectional profile of the photobleached area was imaged and analyzed to determine the scattering and divergence of the beam (Figure C.1).

The region of each image showing the bleaching profile was cropped, rotated, and normalized against values measured from the adjacent area (Figure C.1A,B). We then fit a gaussian curve to the intensity values from each row of the image to measure the width of the profile as it changes with depth (Figure C.1C,D). Finally, the width to depth function was averaged across several images and fit to a parabolic curve (Figure C.2B). This relationship was used to generate a model illumination volume by assuming that, at each depth level, the total illumination is constant (a better model would assume constant illumination across the curved wavefront surfaces, but the flat-surface approximation should suffice for the purposes of this experiment). To estimate the loss of intensity as a function of depth, the model volume

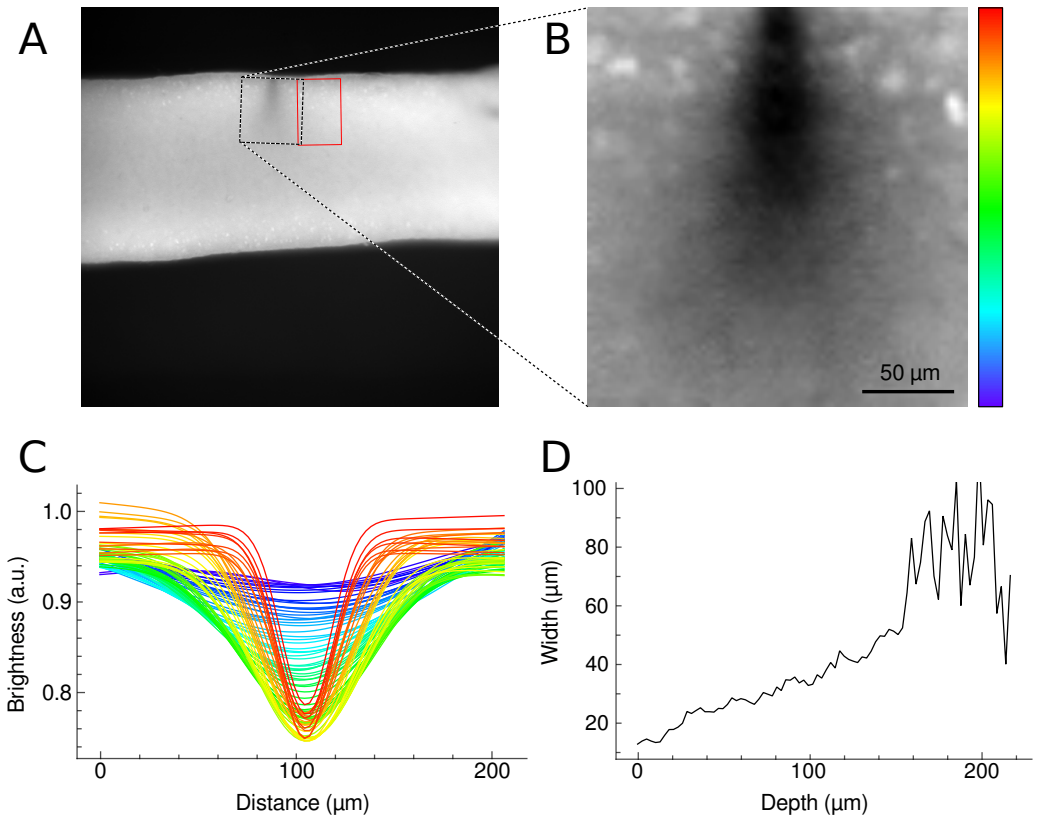

Figure C.1: Example data from a photobleaching experiment. **A)** Fluorescence image of fixed brain slice showing profile of photobleached region (black rectangle). The red rectangle indicates the unbleached region used as a baseline subtraction. **B)** Expanded view of the photobleached region with baseline removed. **C)** Gaussian fits for each row of pixels in (B). The color of each plot corresponds to the depth indicated by the color bar in (B). **D)** The width of the bleached area increases with depth. Measurements deeper than ~150 µm become unreliable because the bleaching is no longer detectable.

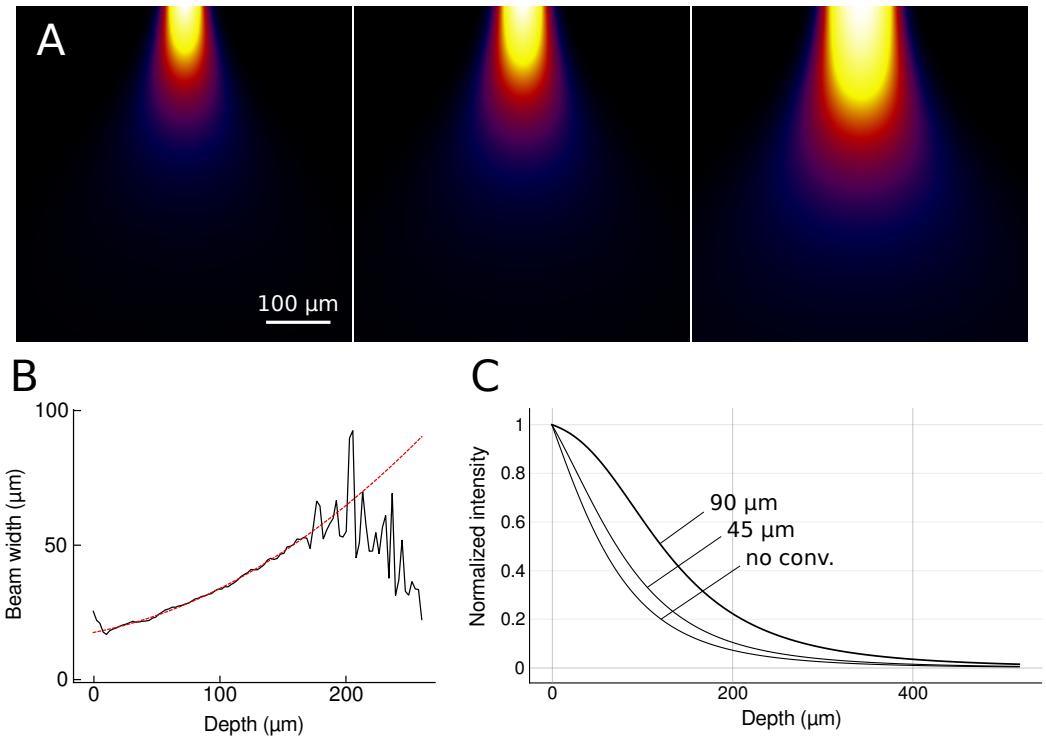

Figure C.2: Simulated laser intensity profiles based on relationship between depth and beam width. **A)** Images of three simulated beam profiles. The first is based on the raw data collected. The second and third are convolved with 45 and 90 µm circular beam profiles, respectively. **B)** Average width vs depth relationship across all images taken. Plotted in red is a parabolic fit used to extrapolate to greater depths. **C)** Simulated intensity vs depth profiles for the 3 convolution criteria listed in (A).

was convolved with circular beam profiles of 45 and 90 µm diameter (Figure C.2A). As expected, wider beam profiles result in significantly greater depth penetration (Figure C.2C). For the beam width used in this study for photostimulation mapping (90 µm), we expect that intensity drops to 50% at a depth of ~100 µm, and 20% at ~200 µm.

REFERENCES

Adams, J. C. and Mugnaini, E. (1984). Dorsal nucleus of the lateral lemniscus: a nucleus of GABAergic projection neurons. *Brain research bulletin*, 13(4):585–90.

Adams, J. C. and Warr, W. B. (1976). Origins of axons in the cat's acoustic striae determined by injection of horseradish peroxidase into severed tracts. *The Journal of comparative neurology*, 170(1):107–21.

Arnott, R. H., Wallace, M. N., Shackleton, T. M., and Palmer, A. R. (2004). Onset neurones in the anteroventral cochlear nucleus project to the dorsal cochlear nucleus. *Journal of the Association for Research in Otolaryngology : JARO*, 5(2):153–70.

Backoff, P. M., Palombi, P. S., and Caspary, D. M. (1997). Glycinergic and GABAergic inputs affect short-term suppression in the cochlear nucleus. *Hearing research*, 110(1-2):155–63.

Backoff, P. M., Shadduck Palombi, P., and Caspary, D. M. (1999). Gamma-aminobutyric acidergic and glycinergic inputs shape coding of amplitude modulation in the chinchilla cochlear nucleus. *Hearing research*, 134(1-2):77–88.

Banks, M. I. and Sachs, M. B. (1991). Regularity analysis in a compartmental model of chopper units in the anteroventral cochlear nucleus. *J Neurophysiol*, 65:606–629.

Barbour, D. and Callaway, E. (2008). Excitatory local connections of superficial neurons in rat auditory cortex. *Journal of Neuroscience*, 28(44):11174 –11185.

Bendels, M. H. K., Beed, P., Schmitz, D., Johenning, F. W., and Leibold, C. (2010). Detection of input sites in scanning photostimulation data based on spatial correlations. *Journal of neuroscience methods*, 192(2):286–95.

Blackburn, C. C. and Sachs, M. B. (1989). Classification of unit types in the anteroventral cochlear nucleus: PST histograms and regularity analysis. *J Neurophysiol*, 62:1303–1329.

Boettcher, F. a., Salvi, R. J., and Saunders, S. S. (1990). Recovery from short-term adaptation in single neurons in the cochlear nucleus. *Hearing research*, 48(1-2):125–44.

Bourk, T. R. (1976). *Electrical Responses of Neural Units in the Anteroventral Cochlear Nucleus of the Cat*. PhD thesis, Massachusetts Institute of Technology.

Bourk, T. R., Mielcarz, J. P., and Norris, B. E. (1981). Tonotopic organization of the anteroventral cochlear nucleus of the cat. *Hear Res*, 4:215–241.

Boyden, E. S., Zhang, F., Bamberg, E., Nagel, G., and Deisseroth, K. (2005). Millisecond-timescale, genetically targeted optical control of neural activity. *Nature neuroscience*, 8(9):1263–8.

Brawer, J. R., Morest, D. K., and Kane, E. C. (1974). The neuronal architecture of the cochlear nucleus of the cat. *The Journal of comparative neurology*, 155(3):251–300.

Brown, M. C., Liberman, M. C., Benson, T. E., and Ryugo, D. K. (1988). Brainstem branches from olivocochlear axons in cats and rodents. *J Comp Neurol*, 278:591–603.

Brownell, W. E. (1975). Organization of the cat trapezoid body and the discharge characteristics of its fibers. *Brain research*, 94(3):413–33.

Bures, Z. and Marsalek, P. (2013). On the precision of neural computation with interaural level differences in the lateral superior olive. *Brain research*.

Cajal, R. y. (1909). *Histologie du système nerveux de l'homme & des vertébrés*.

Cant, N. (1981). The fine structure of two types of stellate cells in the anterior division of the anteroventral cochlear nucleus of the cat. *Neuroscience*, 6(12):2643–55.

Cant, N. and Benson, C. G. (2003). Parallel auditory pathways: projection patterns of the different neuronal populations in the dorsal and ventral cochlear nuclei. *Brain Res Bull*, 60:457–474.

Cant, N. and Gaston, K. C. (1982). Pathways connecting the right and left cochlear nuclei. *The Journal of comparative neurology*, 212(3):313–26.

Cant, N. and Morest, D. K. (1979a). Organization of the neurons in the anterior division of the anteroventral cochlear nucleus of the cat. Light-microscopic observations. *Neuroscience*, 4(12):1925–45.

Cant, N. and Morest, D. K. (1979b). The bushy cells in the anteroventral cochlear nucleus of the cat. A study with the electron microscope. *Neuroscience*, 4(12):1925–45.

Cao, X.-J. and Oertel, D. (2010). Auditory nerve fibers excite targets through synapses that vary in convergence, strength, and short-term plasticity. *Journal of neurophysiology*, 104(5):2308–20.

Caspary, D. M., Backoff, P. M., Finlayson, P. G., and Palombi, P. S. (1994). Inhibitory inputs modulate discharge rate within frequency receptive fields of anteroventral cochlear nucleus neurons. *J Neurophysiol*, 72:2124–2133.

Chase, S. M. and Young, E. D. (2007). First-spike latency information in single neurons increases when referenced to population onset. *Proceedings of the National Academy of Sciences of the United States of America*, 104(12):5175–80.

Colonnier, M. (1968). Synaptic patterns on different cell types in the different laminae of the cat visual cortex. An electron microscope study. *Brain research*, 9(2):268–87.

Dehmel, S., Cui, Y. L., and Shore, S. E. (2008). Cross-modal interactions of auditory and somatic inputs in the brainstem and midbrain and their imbalance in tinnitus and deafness. *American journal of audiology*, 17(2):S193–209.

Doucet, J. R., Ross, A. T., Gillespie, M. B., and Ryugo, D. K. (1999). Glycine immunoreactivity of multipolar neurons in the ventral cochlear nucleus which project to the dorsal cochlear nucleus. *J Comp Neurol*, 408:515–531.

Doucet, J. R. and Ryugo, D. K. (1997). Projections from the ventral cochlear nucleus to the dorsal cochlear nucleus in rats. *J Comp Neurol*, 385:245–264.

Doucet, J. R. and Ryugo, D. K. (2006). Structural and functional classes of multipolar cells in the ventral cochlear nucleus. *Anat Rec A Discov Mol Cell Evol Biol*, 288:331–344.

Ebert, U. and Ostwald, J. (1995a). GABA alters the discharge pattern of chopper neurons in the rat ventral cochlear nucleus. *Hear Res*, 91:160–166.

Ebert, U. and Ostwald, J. (1995b). GABA can improve acoustic contrast in the rat ventral cochlear nucleus. *Exp Brain Res*, 104:310–322.

Evans, E. F. and Nelson, P. G. (1973). The responses of single neurones in the cochlear nucleus of the cat as a function of their location and the anaesthetic state. *Exp Brain Res*, 17(4):402–427.

Fekete, D. M., Rouiller, E. M., Liberman, M. C., and Ryugo, D. K. (1984). The central projections of intracellularly labeled auditory nerve fibers in cats. *The Journal of Comparative Neurology*, 229(3):26– 29.

Feng, A. S. and Vater, M. (1985). Functional organization of the cochlear nucleus of rufous horseshoe bats (Rhinolophus rouxi): frequencies and internal connections are arranged in slabs. *The Journal of comparative neurology*, 235(4):529–53.

Ferragamo, M. J., Golding, N. L., Gardner, S. M., and Oertel, D. (1998a). Golgi cells in the superficial granule cell domain overlying the ventral cochlear nucleus: morphology and electrophysiology in slices. *J Comp Neurol*, 400:519–528.

Ferragamo, M. J., Golding, N. L., and Oertel, D. (1998b). Synaptic inputs to stellate cells in the ventral cochlear nucleus. *Journal of neurophysiology*, 79(1):51–63.

Fino, E., Araya, R., Peterka, D. S., Salierno, M., Etchenique, R., and Yuste, R. (2009). RuBi-Glutamate: Two-Photon and Visible-Light Photoactivation of Neurons and Dendritic spines. *Frontiers in neural circuits*, 3(May):2.

Friedland, D. R., Pongstaporn, T., Doucet, J. R., and Ryugo, D. K. (2003). Ultrastructural examination of the somatic innervation of ventrotubercular cells in the rat. *J Comp Neurol*, 459:77–89.

Frisina, R. D., Smith, R. L., and Chamberlain, S. C. (1990a). Encoding of amplitude modulation in the gerbil cochlear nucleus: I. A hierarchy of enhancement. *Hear Res*, 44:99–122.

Frisina, R. D., Smith, R. L., and Chamberlain, S. C. (1990b). Encoding of amplitude modulation in the gerbil cochlear nucleus: II. Possible neural mechanisms. *Hear Res*, 44:123–141.

Fujino, K. and Oertel, D. (2001). Cholinergic modulation of stellate cells in the mammalian ventral cochlear nucleus. *J Neurosci*, 21:7372–7383.

Gai, Y. and Carney, L. H. (2008a). Influence of inhibitory inputs on rate and timing of responses in the anteroventral cochlear nucleus. *Journal of neurophysiology*, 99(3):1077–95.

Gai, Y. and Carney, L. H. (2008b). Statistical analyses of temporal information in auditory brainstem responses to tones in noise: correlation index and spike-distance metric. *Journal of the Association for Research in Otolaryngology : JARO*, 9(3):373–87.

Ghoshal, S. and Kim, D. O. (1996a). Marginal shell of the anteroventral cochlear nucleus: acoustically weakly-driven and not-driven units in the unanesthetized decerebrate cat. *Acta Otolaryngol*, 116:280–283.

Ghoshal, S. and Kim, D. O. (1996b). Marginal shell of the anteroventral cochlear nucleus: intensity coding in single units of the unanesthetized, decerebrate cat. *Neurosci Lett*, 205:71–74.

Ghoshal, S. and Kim, D. O. (1997). Marginal shell of the anteroventral cochlear nucleus: single-unit response properties in the unanesthetized decerebrate cat. *J Neurophysiol*, 77:2083–2097.

Godfrey, D. a., Kiang, N. Y., and Norris, B. E. (1975). Single unit activity in the posteroventral cochlear nucleus of the cat. *The Journal of comparative neurology*, 162(2):247–68.

Goldberg, J. (1975). Physiological Studies of Auditory Nuclei of the Pons. In Keidel, WolfD. and Neff, W., editor, *Auditory System, Handbook of Sensory Physiology*, pages 109–144. Springer Berlin Heidelberg.

Goldberg, J. and Brown, P. (1969). Response of binaural neurons of dog superior olivary complex to dichotic tonal stimuli: some physiological mechanisms of sound localization. *Journal of neurophysiology*, 32(4):613.

Goldberg, J. and Brownell, W. (1973). Discharge characteristics of neurons in anteroventral and dorsal cochlear nuclei of cat. *Brain research*, 64:35—-54.

Gómez-Nieto, R. and Rubio, M. E. (2009). A bushy cell network in the rat ventral cochlear nucleus. *The Journal of comparative neurology*, 516(4):241–63.

Gómez-Nieto, R. and Rubio, M. E. (2011). Ultrastructure, synaptic organization, and molecular components of bushy cell networks in the anteroventral cochlear nucleus of the rhesus monkey. *Neuroscience*, 179:188–207.

Hall, J. W., Haggard, M. P., and Fernandes, M. A. (1984). Detection in noise by spectro-temporal pattern analysis. *The Journal of the Acoustical Society of America*, 76(1):50–6.

Han, X. and Boyden, E. S. (2007). Multiple-color optical activation, silencing, and desynchronization of neural activity, with single-spike temporal resolution. *PloS one*, 2(3):e299.

Histed, M. H., Bonin, V., and Reid, R. C. (2009). Direct activation of sparse, distributed populations of cortical neurons by electrical microstimulation. *Neuron*, 63(4):508–22.

Hunter, C., Doi, K., and Wenthold, R. J. (1992). Neurotransmission in the auditory system. *Otolaryngologic clinics of North America*, 25(5):1027–52.

Irvine, D. R., Park, V. N., and McCormick, L. (2001). Mechanisms underlying the sensitivity of neurons in the lateral superior olive to interaural intensity differences. *Journal of neurophysiology*, 86(6):2647–66.

Irvine, D. R. F. (1986). *The Auditory Brainstem*, volume 7 of *Progress in Sensory Physiology*. Springer Berlin Heidelberg, Berlin, Heidelberg.

Jin, X., Prince, D. A., and Huguenard, J. R. (2006). Enhanced excitatory synaptic connectivity in layer v pyramidal neurons of chronically injured epileptogenic neocortex in rats. *The Journal of neuroscience : the official journal of the Society for Neuroscience*, 26(18):4891–900.

Johnson, G. A., Badea, A., Brandenburg, J., Cofer, G., Fubara, B., Liu, S., and Nissanov, J. (2010). Waxholm space: an image-based reference for coordinating mouse brain research. *NeuroImage*, 53(2):365–72.

Joris, P. X., Carney, L. H., Smith, P. H., and Yin, T. C. (1994). Enhancement of neural synchronization in the anteroventral cochlear nucleus. I. Responses to tones at the characteristic frequency. *J Neurophysiol*, 71:1022–1036.

Joris, P. X., Smith, P., Carney, L. H., and Yin, T. (1991). Projections of physiologically characterized globular bushy cell axons from the cochlear nucleus of the cat. *The Journal of Comparative Neurology*, 304(3).

Josephson, E. M. and Morest, D. k. (1998). A quantitative profile of the synapses on the stellate cell body and axon in the cochlear nucleus of the chinchilla. *Journal of neurocytology*, 27(11):841–64.

Katz, L. C. and Dalva, M. B. (1994). Scanning laser photostimulation: a new approach for analyzing brain circuits. *Journal of neuroscience methods*, 54(2):205–18.

Kiang, N. Y., Pfeiffer, R. R., Warr, W. B., and Backus, A. (1965). Stimulus coding in the cochlear nucleus. *Ann Otol Rhinol Laryngol*, 74:463–485.

Kopp-Scheinpflug, C., Dehmel, S., Dorrscheidt, G. J., and Rubsamen, R. (2002). Interaction of excitation and inhibition in anteroventral cochlear nucleus neurons that receive large endbulb synaptic endings. *J Neurosci*, 22:11004–11018.

Kuo, S. P., Lu, H.-W., and Trussell, L. O. (2012). Intrinsic and synaptic properties of vertical cells of the mouse dorsal cochlear nucleus. *Journal of neurophysiology*, 0044050.

Lauer, A. M., Connelly, C. J., Graham, H., and Ryugo, D. K. (2013). Morphological Characterization of Bushy Cells and Their Inputs in the Laboratory Mouse (Mus musculus) Anteroventral Cochlear Nucleus. *PloS one*, 8(8):e73308.

Liberman, M. (1982). Single-neuron labeling in the cat auditory nerve. *Science*, 216(4551):1239–1241.

Liberman, M. (1991). Central projections of auditory-nerve fibers of differing spontaneous rate. I. Anteroventral cochlear nucleus. *The Journal of Comparative Neurology*, 313(2):240–258.

Lloyd, S. (2001). Measures of Complexity a non–exhaustive list. *IEEE Control Systems Magazine*, 21(4).

Louage, D. H. G., van der Heijden, M., and Joris, P. X. (2005). Enhanced temporal response properties of anteroventral cochlear nucleus neurons to broadband noise. *The Journal of neuroscience : the official journal of the Society for Neuroscience*, 25(6):1560–70.

Manis, P. B. and Marx, S. O. (1991). Outward currents in isolated ventral cochlear nucleus neurons. *J Neurosci*, 11:2865–2880.

Martin, M. R. and Dickson, J. W. (1983). Lateral inhibition in the anteroventral cochlear nucleus of the cat: a microiontophoretic study. *Hearing research*, 9(1):35–41.

McGinley, M. J. and Oertel, D. (2006). Rate thresholds determine the precision of temporal integration in principal cells of the ventral cochlear nucleus. *Hear Res*, 216-217:52–63.

Moller, A. R. (1974a). Responses of units in the cochlear nucleus to sinusoidally amplitude-modulated tones. *Experimental neurology*, 45(1):105–17.

Moller, A. R. (1974b). Responses of units in the cochlear nucleus to sinusoidally amplitude-modulated tones. *Experimental neurology*, 45(1):105–17.

Moller, A. R. (1975). Latency of unit responses in cochlear nucleus determined in two different ways. *Journal of neurophysiology*, 38(4):812–21.

Mugnaini, E., Warr, W. B., and Osen, K. K. (1980). Distribution and light microscopic features of granule cells in the cochlear nuclei of cat, rat, and mouse. *The Journal of comparative neurology*, 191(4):581–606.

Mulders, W. H., Seluakumaran, K., and Robertson, D. (2008). Effects of centrifugal pathways on responses of cochlear nucleus neurons to signals in noise. *Eur J Neurosci*, 27:702–714.

Muniak, M. a., Rivas, A., Montey, K. L., May, B. J., Francis, H. W., and Ryugo, D. K. (2013). 3D model of frequency representation in the cochlear nucleus of the CBA/J mouse. *The Journal of comparative neurology*, 521(7):1510–32.

Muniak, M. A. and Ryugo, D. K. (2013). Tonotopic organization of vertical cells in the dorsal cochlear nucleus of the CBA/J mouse. *The Journal of comparative neurology*.

Munirathinam, S., Ostapoff, E. M., Gross, J., Kempe, G. S., Dutton, J. A., and Morest, D. K. (2004). Organization of inhibitory feed-forward synapses from the dorsal to the ventral cochlear nucleus in the cat: a quantitative analysis of endings by vesicle morphology. *Hear Res*, 198:99–115.

Oertel, D. (1983). Synaptic responses and electrical properties of cells in brain slices of the mouse anteroventral cochlear nucleus. *Journal of Neuroscience*, 3(10):2043–2053.

Oertel, D., Bal, R., Gardner, S. M., Smith, P. H., and Joris, P. X. (2000). Detection of synchrony in the activity of auditory nerve fibers by octopus cells of the mammalian cochlear nucleus. *Proc Natl Acad Sci U S A*, 97:11773–11779.

Oertel, D., Fay, R. R., and Popper, A. N. (2002). *Integrative Functions in the Mammalian Auditory Pathway*. Springer.

Oertel, D., Wright, S., Cao, X.-J., Ferragamo, M., and Bal, R. (2011). The multiple functions of T stellate/multipolar/chopper cells in the ventral cochlear nucleus. *Hearing research*, 276(1-2):61–9.

Oertel, D. and Wu, S. (1984). Intracellular injection with horseradish peroxidase of physiologically characterized stellate and bushy cells in slices of mouse anteroventral cochlear nucleus. *Journal of Neuroscience*, 4(6):1577–1588.

Oertel, D. and Wu, S. H. (1989). Morphology and physiology of cells in slice preparations of the dorsal cochlear nucleus of mice. *The Journal of comparative neurology*, 283(2):228–47.

Oertel, D., Wu, S. H., Garb, M. W., and Dizack, C. (1990). Morphology and physiology of cells in slice preparations of the posteroventral cochlear nucleus of mice. *The Journal of comparative neurology*, 295(1):136–54.

Osen, K. K. (1969). Cytoarchitecture of the cochlear nuclei in the cat. *The Journal of Comparative Neurology*, 136(4).

Ostapoff, E. M. and Morest, D. K. (1991). Synaptic organization of globular bushy cells in the ventral cochlear nucleus of the cat: a quantitative study. *The Journal of Comparative Neurology*, 314(3):598–613.

Ostapoff, E. M., Morest, D. K., and Parham, K. (1999). Spatial organization of the reciprocal connections between the cat dorsal and anteroventral cochlear nuclei. *Hearing research*, 130(1-2):75–93.

Palmer, A. R., Jiang, D., and Marshall, D. H. (1996). Responses of ventral cochlear nucleus onset and chopper units as a function of signal bandwidth. *J Neurophysiol*, 75:780–794.

Palmer, A. R., Wallace, M. N., Arnott, R. H., and Shackleton, T. M. (2003). Morphology of physiologically characterised ventral cochlear nucleus stellate cells. *Exp Brain Res*, 153:418–426.

Palombi, P. S. and Caspary, D. M. (1992). GABAA receptor antagonist bicuculline alters response properties of posteroventral cochlear nucleus neurons. *Journal of neurophysiology*, 67(3):738–46.

Paolini, A. G., Clarey, J. C., Needham, K., and Clark, G. M. (2004). Fast inhibition alters first spike timing in auditory brainstem neurons. *Journal of neurophysiology*, 92(4):2615–21.

Paolini, A. G., Clarey, J. C., Needham, K., and Clark, G. M. (2005). Balanced inhibition and excitation underlies spike firing regularity in ventral cochlear nucleus chopper neurons. *Eur J Neurosci*, 21:1236–1248.

Peters, A., Palay, S., and Webster, H. (1991). *Fine Structure of the Nervous System: Neurons and Their Supporting Cells*. Oxford University Press, USA.

Pfeiffer, R. R. (1966). Classification of response patterns of spike discharges for units in the cochlear nucleus: tone-burst stimulation. *Experimental brain research. Experimentelle Hirnforschung. Expérimentation cérébrale*, 1(3):220–35.

Pressnitzer, D., Meddis, R., Delahaye, R., and Winter, I. M. (2001). Physiological correlates of comodulation masking release in the mammalian ventral cochlear nucleus. *J Neurosci*, 21:6377–6386.

Raman, I. M. and Trussell, L. O. (1992). The kinetics of the response to glutamate and kainate in neurons of the avian cochlear nucleus. *Neuron*, 9(1):173–86.

Ranck, J. B. (1975). Which elements are excited in electrical stimulation of mammalian central nervous system: a review. *Brain research*, 98(3):417–40.

Rhode, W. S. and Greenberg, S. (1994a). Encoding of amplitude modulation in the cochlear nucleus of the cat. *Journal of neurophysiology*, 71(5):1797.

Rhode, W. S. and Greenberg, S. (1994b). Lateral suppression and inhibition in the cochlear nucleus of the cat. *Journal of neurophysiology*, 71(2):493–514.

Rhode, W. S., Oertel, D., and Smith, P. H. (1983). Physiological response properties of cells labeled intracellularly with horseradish peroxidase in cat ventral cochlear nucleus. *The Journal of comparative neurology*, 213(4):448–63.

Rhode, W. S. and Smith, P. H. (1985). Characteristics of tone-pip response patterns in relationship to spontaneous rate in cat auditory nerve fibers. *Hearing research*, 18(2):159–68.

Rhode, W. S. and Smith, P. H. (1986). Encoding timing and intensity in the ventral cochlear nucleus of the cat. *Journal of neurophysiology*, 56(2):261–86.

Richardson, M. J. E. and Silberberg, G. (2008). Measurement and analysis of postsynaptic potentials using a novel voltage-deconvolution method. *Journal of neurophysiology*, 99(2):1020–31.

Rose, J. E., Brugge, J. F., Anderson, D. J., and Hind, J. E. (1967). Phase-locked response to low-frequency tones in single auditory nerve fibers of the squirrel monkey. *Journal of neurophysiology*, 30(4):769–93.

Rothman, J. S. and Manis, P. B. (2003a). Differential expression of three distinct potassium currents in the ventral cochlear nucleus. *J Neurophysiol*, 89:3070–3082.

Rothman, J. S. and Manis, P. B. (2003b). The roles potassium currents play in regulating the electrical activity of ventral cochlear nucleus neurons. *J Neurophysiol*, 89:3097–3113.

Rothman, J. S., Young, E. D., and Manis, P. B. (1993). Convergence of auditory nerve fibers onto bushy cells in the ventral cochlear nucleus: implications of a computational model. *J Neurophysiol*, 70:2562–2583.

Rouiller, E. M. and Ryugo, D. K. (1984). Intracellular marking of physiologically characterized cells in the ventral cochlear nucleus of the cat. *J Comp Neurol*, 225:167–186.

Ryugo, D. K., Babalian, A. L., and Rouiller, E. M. (2003). Discharge properties of identified cochlear nucleus neurons and auditory nerve fibers in response to repetitive electrical stimulation of the auditory nerve. *Experimental brain research. Experimentelle Hirnforschung. Expérimentation cérébrale*, 153(4):452–60.

Ryugo, D. K. and Parks, T. N. (2003). Primary innervation of the avian and mammalian cochlear nucleus. *Brain research bulletin*, 60(5-6):435–56.

Sachs, M. B. and Abbas, P. J. (1974). Rate versus level functions for auditory-nerve fibers in cats: tone-burst stimuli. *The Journal of the Acoustical Society of America*, 56(6):1835–47.

Saint Marie, R. L., Benson, C. G., Ostapoff, E. M., and Morest, D. K. (1991). Glycine immunoreactive projections from the dorsal to the anteroventral cochlear nucleus. *Hear Res*, 51:11–28.

Schofield, B. R. and Cant, N. (1996). Projections from the ventral cochlear nucleus to the inferior colliculus and the contralateral cochlear nucleus in guinea pigs. *Hear Res*, 102:1–14.

Sento, S. and Ryugo, D. K. (1989). Endbulbs of held and spherical bushy cells in cats: morphological correlates with physiological properties. *The Journal of comparative neurology*, 280(4):553–62.

Shepherd, G. M. G., Pologruto, T. A., and Svoboda, K. (2003). Circuit analysis of experience-dependent plasticity in the developing rat barrel cortex. *Neuron*, 38(2):277–89.

Shofner, W. P. (1999). Responses of cochlear nucleus units in the chinchilla to iterated rippled noises: analysis of neural autocorrelograms. *Journal of neurophysiology*, 81(6):2662–74.

Shofner, W. P. and Young, E. D. (1985). Excitatory/inhibitory response types in the cochlear nucleus: relationships to discharge patterns and responses to electrical stimulation of the auditory nerve. *Journal of neurophysiology*, 54(4):917–39.

Shore, S. E. (1995). Recovery of forward-masked responses in ventral cochlear nucleus neurons. *Hear Res*, 82:31–43.

Shore, S. E. (1998). Influence of centrifugal pathways on forward masking of ventral cochlear nucleus neurons. *J Acoust Soc Am*, 104:378–389.

Shore, S. E., Helfert, R. H., Bledsoe, S. C., Altschuler, R. a., and Godfrey, D. a. (1991). Descending projections to the dorsal and ventral divisions of the cochlear nucleus in guinea pig. *Hearing research*, 52(1):255–68.

Shore, S. E., Vass, Z., Wys, N. L., and Altschuler, R. A. (2000). Trigeminal ganglion innervates the auditory brainstem. *J Comp Neurol*, 419:271–285.

Smith, P. H., Joris, P. X., and Yin, T. C. (1993). Projections of physiologically characterized spherical bushy cell axons from the cochlear nucleus of the cat: evidence for delay lines to the medial superior olive. *The Journal of comparative neurology*, 331(2):245–60.

Smith, P. H. and Rhode, W. S. (1987). Characterization of HRP-labeled globular bushy cells in the cat anteroventral cochlear nucleus. *J Comp Neurol*, 266:360–375.

Smith, P. H. and Rhode, W. S. (1989). Structural and functional properties distinguish two types of multipolar cells in the ventral cochlear nucleus. *The Journal of comparative neurology*, 282(4):595–616.

Spangler, K. M., Cant, N., Henkel, C. K., Farley, G. R., and Warr, W. B. (1987). Descending projections from the superior olivary complex to the cochlear nucleus of the cat. *The Journal of comparative neurology*, 259(3):452–65.

Spirou, G. A., Brownell, W., and Zidanic, M. (1990). Recordings from cat trapezoid body and HRP labeling of globular bushy cell axons. *Journal of Neurophysiology*, 63(5):1169–1190.

Spirou, G. A., Manis, P. B., and Rager, J. (2005). Convergence of auditory-nerve fiber projections onto globular bushy cells. *Neuroscience*, 136:843– 863.

Starr, A. and Britt, R. (1970). Intracellular recordings from cat cochlear nucleus during tone stimulation. *Journal of neurophysiology*, 33(1):137–47.

Sutherland, D. P., Glendenning, K. K., and Masterton, R. B. (1998). Role of acoustic striae in hearing: discrimination of sound-source elevation. *Hearing research*, 120(1-2):86–108.

Tanaka, Y., Tanaka, Y., Furuta, T., Yanagawa, Y., and Kaneko, T. (2008). The effects of cutting solutions on the viability of GABAergic interneurons in cerebral cortical slices of adult mice. *Journal of neuroscience methods*, 171(1):118–25.

Tolbert, L. P., Morest, D. K., and Yurgelun-Todd, D. A. (1982). The neuronal architecture of the anteroventral cochlear nucleus of the cat in the region of the cochlear nerve root: horseradish peroxidase labelling of identified cell types. *Neuroscience*, 7(12):3031–3052.

Typlt, M., Englitz, B., Sonntag, M., Dehmel, S., Kopp-Scheinpflug, C., and Ruebsamen, R. (2012). Multidimensional characterization and differentiation of neurons in the anteroventral cochlear nucleus. *PloS one*, 7(1):e29965.

Wang, X. and Sachs, M. B. (1994). Neural encoding of single-formant stimuli in the cat. II. Responses of anteroventral cochlear nucleus units. *J Neurophysiol*, 71:59–78.

Wang, Y. and Manis, P. B. (2005). Synaptic transmission at the cochlear nucleus endbulb synapse during age-related hearing loss in mice. *Journal of neurophysiology*, 94(3):1814–24.

Weaver, W. (1948). Science and complexity. *American scientist*, 36(4):536–44.

Webster, D. B. and Fay, R. R. (1992). *The Mammalian Auditory Pathway: Neuroanatomy*. Springer.

Webster, D. B. and Trune, D. R. (1982). Cochlear nuclear complex of mice. *Am J Anat*, 163:103–130.

Wenthold, R. J. (1987). Evidence for a glycinergic pathway connecting the two cochlear nuclei: an immunocytochemical and retrograde transport study. *Brain research*, 415(1):183–7.

White, J. A., Young, E. D., and Manis, P. B. (1994). The electrotonic structure of regular-spiking neurons in the ventral cochlear nucleus may determine their response properties. *Journal of neurophysiology*, 71(5):1774–86.

Wickesberg, R. E. and Oertel, D. (1988). Tonotopic projection from the dorsal to the anteroventral cochlear nucleus of mice. *J Comp Neurol*, 268:389–399.

Wickesberg, R. E. and Oertel, D. (1990). Delayed, frequency-specific inhibition in the cochlear nuclei of mice: a mechanism for monaural echo suppression. *J Neurosci*, 10:1762–1768.

Wickesberg, R. E., Whitlon, D., and Oertel, D. (1991). Tuberculoventral neurons project to the multipolar cell area but not to the octopus cell area of the posteroventral cochlear nucleus. *The Journal of comparative neurology*, 313(3):457–68.

Winter, I. M., Robertson, D., and Yates, G. K. (1990). Diversity of characteristic frequency rate-intensity functions in guinea pig auditory nerve fibres. 45:191–202.

Wu, S. H. and Oertel, D. (1986). Inhibitory circuitry in the ventral cochlear nucleus is probably mediated by glycine. *J Neurosci*, 6:2691–2706.

Xie, R. and Manis, P. B. (2013). Target-specific IPSC kinetics promote temporal processing in auditory parallel pathways. *The Journal of neuroscience : the official journal of the Society for Neuroscience*, 33(4):1598–614.

Xu-Friedman, M. A. and Regehr, W. G. (2005). Dynamic-clamp analysis of the effects of convergence on spike timing. II. Few synaptic inputs. *Journal of neurophysiology*, 94(4):2526–34.

Young, E. D. and Brownell, W. (1976). Responses to tones and noise of single cells in dorsal cochlear nucleus of unanesthetized cats. *Journal of Neurophysiology*, 39(2):282–300.

Young, E. D., Robert, J. M., and Shofner, W. P. (1988). Regularity and latency of units in ventral cochlear nucleus: implications for unit classification and generation of response properties. *J Neurophysiol*, 60(1):1–29.

Young, E. D. and Voigt, H. F. (1982). Response properties of type II and type III units in dorsal cochlear nucleus. *Hearing research*, 6(2):153–69.

Zhang, S. and Oertel, D. (1993). Tuberculoventral cells of the dorsal cochlear nucleus of mice: intracellular recordings in slices. *Journal of neurophysiology*, 69(5):1409–21.

Zilany, M. S. a., Bruce, I. C., Nelson, P. C., and Carney, L. H. (2009). A phenomenological model of the synapse between the inner hair cell and auditory nerve: long-term adaptation with power-law dynamics. *The Journal of the Acoustical Society of America*, 126(5):2390–412.